INTERNAL PROCESSES OF SAND AND OTHER POROUS MEDIA

A Dissertation

Presented to the Faculty of the Graduate School

of Cornell University

in Partial Fulfillment of the Requirements for the Degree of

Doctor of Philosophy

by

Jin Xu

April 2015

INTERNAL PROCESSES OF SAND AND OTHER POROUS MEDIA

Jin Xu, Ph.D.

Cornell University 2015

This dissertation discusses internal processes of porous media from multiple perspectives.

In chapter 2, “Statistical Mechanics of Unsaturated Porous Media,” we derive a statistical mechanical model of fluid retention characteristics in porous media in terms of known surface energies and void geometry within the permeable solid based on the Ising model from magnetism. In the limit of vanishing inertial and viscous forces, the theory predicts the fuid retention curve that relates saturation of the porous matrix to applied capillary pressure. We show how the fluid retention curve can be calculated from the statistical distribution of two dimensionless parameters measuring, respectively, the areas of link cross-section and wetted cavity surface with respect to cavity volume. The theory attributes hysteresis of the retention curve to collective first-order phase transitions in the network of cavities. Furthermore, we illustrate predictions with a porous domain consisting of a random packing of spheres, and reproduce the behavior of Haines jumps, which we associate with phase transitions.

Chapters 3 and 4 features experimental studies of a particular type of particulate porous media – sand and explores the internal processes of sand dunes and their surface ripples. Chapter 3, “Temperature and Humidity within a Mobile Barchan Sand Dune,” (co-authored with A. Valance, A. Ould el-Moctar, A. G. Hay and R. Richer), attempts at answering a practical question of potential importance to dune stabilization, whether temperature and moisture deep

within relatively fast moving hyperarid mobile dunes present a suitable habitat for microbes. We contrast deep thermal records obtained from implanted probes with measurements of diurnal variations of the temperature profile just below the surface, and show that temperature within fast moving dunes is predictable, as long as dune advection is properly considered. Observations and analyses also suggest that small quantities of rain falling on the leeward face escape evaporation and endure within the dune until resurfacing upwind. At depths below 10 cm, we show that moisture, rather than temperature, determines the viability of microbes.

Toward elucidating how a wavy porous sand bed perturbs a turbulent flow above its surface, in Chapter 4, "Pore Pressure in a Wind-swept Rippled Bed," (co-authored with R. A. Musa, S. Takarrouht, and M. E. Berberich), we record and model pressure within a permeable material resembling the region just below desert ripples. We discovered that, unlike flows on impermeable waves, the porous rippled bed diffuses the depression upstream, reduces surface pressure gradients, and gives rise to a slip velocity, thus affecting the turbulent boundary layer. Pressure gradients within the porous material also generate body forces rising with wind speed squared and ripple aspect ratio, partially counteracting gravity around crests, thereby facilitating the onset of erosion.

Although these three essays differ in method and focus, they are all address the internal processes of porous media.

BIOGRAPHICAL SKETCH

Jin Xu is currently in his 5th year of study in the Sibley School of Mechanical and Aerospace Engineering at Cornell University. In May 2015, he is expected to graduate with a Ph.D. in Mechanical Engineering with a focus on unsaturated porous media.

Born and raised in the People's Republic of China, Jin received his Bachelor's Degree in Applied Physics from Nanjing University in 2006 before coming to the United States to continue his graduate studies. He received a Master's Degree in Physics from the University of Kansas in 2010 before joining Cornell. Jin received his Master's Degree in Mechanical Engineering from Cornell in 2013.

Jin spent the summer of 2011 at the Pacific Northwest National Laboratory as a Research Intern when he designed an intelligent and automated process of generating the Hamiltonian describing alloy formation energy. He later applied this knowledge in Statistical Mechanics and in Thermodynamics to the study of fluid retention characteristics of unsaturated porous media as the principle subject of his PhD dissertation.

Jin has served as a Research Assistant in the Department of Physics at the University of Kansas and in the Department of Mechanical Engineering at Cornell University. He also served as a Teaching Assistant in both universities and thoroughly enjoyed his time spent interacting with the instructors and the students there.

Outside of academics, Jin enjoys watching documentaries on history and military, endless Wikipedia "chain-viewing", playing flight simulators, and occasionally a few games of badminton to blow off steam.

This document is dedicated to all fellow Ph.D. students.

ACKNOWLEDGEMENTS

First and foremost, I would like to thank my supervisor Prof. Michel Louge for the inspirational guidance and the tremendous amount of help throughout my graduate studies at Cornell, and for introducing me to the fascinating and fruit-bearing research subject of unsaturated porous media. His liberal and supportive management style encouraged the freedom of creativity. His courteous and friendly character has always made even the most tedious aspects of scientific research a lot more enjoyable than would otherwise have been.

I would like to thank members of my thesis committee, Profs. Olivier Desjardins and Abraham Stroock, for the enlighten discussions and their encouragement and support during my graduate studies at Cornell.

I would like to recognize the fundamental importance that Qatar National Research Fund and the Department of Mechanical Engineering had in making possible my graduate studies.

I would also like to give thanks to Jiang Wan, Bin Wen, Peng Chen, Alais Hewes, Daniel Balantine for giving me their invaluable insight, assistance and support throughout the entire time that I have been fortunate enough to know and work with each of them.

Among the many people I am indebted to, I am especially grateful to Xiangjun Qiu for his generous help, his inspirational attitude toward scientific research, and his insightful comments, feedback and discussions throughout my graduate career.

And to my parents Chaohua Xu and Chang Chai, and my wife Ran Cao goes my last, most important and grateful thank you of all!

TABLE OF CONTENTS

LIST OF TABLES

LIST OF FIGURES

CHAPTER 1

CONTEXTUAL INTRODUCTION

This thesis is inspired by the hope that desertification can be mitigated by fixing sand dunes with microbes, thereby beginning a process of vegetation growth.

Recent NASA satellite imagery [2] reveals that dry areas cover over one third of the world. While much of it is already deserts, the rest is continuously degraded by sand. Desertification is a kind of land degradation, in which a relatively dry land region becomes increasingly arid and eventually loses its entire soil content to sand. It is a serious threat affecting over 110 countries and about 70% of the world's agricultural dry lands. This is especially true in Africa, as well as in China where the author was raised.

Sand forms not only from natural processes such as mountains and boulders breaking up, but also from excessive degradation of land as a consequence of climate change and human activities. Some of these newly "freed" grains accumulate on a massive scale and become sand dunes. In this way, static stone mountains become mobile sands, thereby posing significant threat to human activities. Desertification threatens food production and promotes water scarcity, famine, forced migration, and even political instability.

Halting a dune means stopping sand grains from avalanching beyond its brink. The most efficient way to achieve this is to deploy sand catchers such as trees or cacti on the leeward face. In 2005, 11 African countries banded together to create the Great Green Wall in the Sahara. A fantastic project, the initial plan called for a shelter belt of trees to be planted right across the African continent, from Mauritania in the West, all the way to Djibouti in the East [1].

However, the effectiveness of deploying plants as sand catchers is unclear. Aside from the obvious difficulty that dune surfaces rarely provide micro climates suitable for plant growth, one additional problem with planting trees is that poor people, who are often located nearby a desertification front, often chop them down for firewood or other household usage.

Our motivation, on the other hand, is to work against desertification by stabilizing sand dunes with microbes such as *Bacillus pasteurii*, a micro-organism that is readily available in wetlands and marshes and is known to promote Microbe-Induced Calcite Precipitation (MiCP). With an ability to metabolize urea, MiCP microbes can cement a pile of loose sand into sandstones. During such process, *Bacillus pasteurii* fills up voids between grains, initiates a chemical process that precipitates calcite, which serves as a natural cement that binds grains together [51].

Before designing a feasible strategy for microbial dune stabilization, we must first gauge whether sufficient water is available for microbial growth, and whether microbes can be protected from arid conditions on the dune surface. To that end, we must understand internal dune physical processes, such as the diurnal and seasonal variations of humidity and temperature, as well as internal transport of these variables.

In this context, we present three essays laying foundations toward understanding whether conditions within a desert sand bed are suitable for microbial growth. These essays include 1) a model capturing the fluid retention behavior of porous media such as sand, 2) field measurements of the internal temperature and humidity variation within a mobile sand dune, and 3) experimental measurements of pore pressure within a wind-swept rippled porous bed.

This dissertation is structured as follows. We present the first essay in chapter 2 where we take a statistical mechanical approach toward the fluid retention characteristics in porous media. In the limit of vanishing inertial and viscous forces, the theory predicts the fluid retention curve that relates saturation of the porous matrix to applied capillary pressure. To avoid complicated calculations, we deliberately adopt the simplest statistical mechanics, in which a unit cell is made up of a single cavity interacting with its neighbors through narrow openings called “links”, while possessing only two energy states that are either full or empty of fluid. We show how the resulting retention curve can be calculated from the statistical distribution of two dimensionless parameters, α and λ, measuring, respectively the areas of link cross-section and wetted cavity surface with respect to cavity volume. The theory attributes hysteresis of the retention curve to collective first-order phase transitions in the network of cavities. We illustrate predictions with a porous domain consisting of a random packing of spheres, and we reproduce the behavior of Haines jumps, which we associate with phase transitions. We show that hysteresis strength grows with λ and weakens as the distribution of α and λ broadens. An estimate of the correlation length among neighboring cavities implies that reproducibility of the uid retention curve worsens at intermediate saturation as capillary pressure is applied across distant boundaries. This suggests that equations capturing the spatio-temporal evolution of saturation in porous media should be integrated with a retention curve measured across a mesoscopic domain of relatively small size.

Chapter 3 contains our second essay which explores the temperature and humidity within a mobile barchan sand dune. We report measurements of temperature and humidity from probes initially sunk below the leeward avalanche face of a mobile barchan dune in the Qatar desert, emerging windward after 15 months of deep burial. Despite large diurnal variations on the surface, temperature within this dune of 5.6 m height is predictable, as long as dune advection is properly considered. It evolves on smaller amplitude and longer timescale than the surface, lagging average seasonal atmospheric conditions by about 2 months. We contrast these deep thermal records with measurements of diurnal variations of the temperature profile just below the surface, which we calculate with a thermal model predicting the relative roles of wind-driven convective heat transfer and net radiation flux on the dune. Observations and analyses also suggest why random precipitation on the leeward face produces a more unpredictable moisture patchwork on the windward slope. By rapidly reaching sheltered depths, small quantities of rain falling on that face escape evaporation and endure within the dune until resurfacing upwind. At depths below 10 cm, we show that moisture, rather than temperature, determines the viability of microbes and we provide initial microscopic and respiration-based evidence of their presence below the windward slope.

The third essay presented in chapter 4 is concerned with how a wavy porous sand bed perturbs a turbulent flow above its surface. We record pressure within a permeable material resembling the region just be- low desert ripples, contrasting these delicate measurements with earlier studies on similar impermeable surfaces. We run separate tests in a wind tunnel on two sinusoidal porous ripples with aspect ratio of half crest-to-trough amplitude to wavelength of 3% and 6%. For the smaller ratio, pore pressure is a function of streamwise distance with a single delayed harmonic decaying exponentially with depth and proportional to wind speed squared. The resulting pressure on the porous surface is nearly identical to that on a similar impermeable wave. Pore pressure variations at the larger aspect ratio are greater and more complicated. Consistent with the regime map of Kuzan et al. [127], the flow separates, creating a depression at crests. Unlike flows on impermeable waves, the porous rippledbed diffuses the depression upstream, reduces surface pressure gradients, and gives rise to a slip velocity, thus affecting the turbulent boundary layer. Pressure gradients within the porous material also generate body forces rising with wind speed squared and ripple aspect ratio, partially counteracting gravity around crests, thereby facilitating the onset of erosion, particularly on ripples of high aspect ratio armored with large surface grains. By establishing how pore pressure gradients scale with ripple aspect ratio and wind speed, our measurements quantify the internal seepage flow that draws dust and humidity beneath the porous surface.

This work presented in this dissertation is sponsored by the Qatar National Research Foundation. It is a collaboration with the Weill-Cornell Medical College in Qatar, the Biotechnology Centre of the Qatar Ministry of Environment, Maersk Oil in Qatar, the Ecole Polytechnique Federale de Lausanne, Tencate Geosynthetics, the Universite de Rennes, the Universite de Nantes, the Laboratoire 3SR of the Universite de Grenoble, DAMTP at the University of Cambridge, the LGPM laboratory of the Ecole Centrale de Paris, and the Faculte des Sciences de Nouakchott.

CHAPTER 2

STATISTICAL MECHANICS OF UNSATURATED POROUS MEDIA

2.1 Introduction

Unsaturated porous media are ubiquitous in geophysical and industrial processes. They include, for example, soils partially filled with water, fuel cell, or oil reservoirs holding several gas and liquid phases. They also underlie techniques like mercury porosimetry [213]. The principal challenge is to predict how fluid penetrates into, – or emerges from –, a porous solid matrix upon applying a macroscopic gradient in negative tensile pressure p_ℓ on the liquid relative to the surrounding ambient pressure p_g. In general, porous solids delimit a complex geometrical network consisting of a large number of small individual cavities interconnected through several narrow openings. When a porous sample traps one kind of liquid at a volume fraction θ, a simple measure of its partial filling state is the saturation $S \equiv \theta/(1-\nu)$, where ν is the solid volume fraction of the dry sample.

Because the capillary energy of a cavity depends upon the degree of saturation of its neighbors, the establishment of a local equilibrium derives from many-body interactions similar to those handled by statistical mechanics [41], such as lattice gas [131], neural network [106], and spin glasses [54, 25]. In this context, we propose a mean field theory of fluid retention in unsaturated porous media.

In this regime, the porous network exhibits a non-linear hysteretic behavior, whereby an applied macroscopic capillary pressure $\psi \equiv p_g - p_\ell$ delivers a higher saturation when ψ rises to expel the liquid, than when ψ is gradually released to return fluid to the sample. The relation $S = f(\psi)$ then includes two limiting "fluid retention curves" that describe, respectively, the wetting of an initially dry porous solid $S = f_w(\psi)$ and the draining of a completely saturated sample $S = f_d(\psi)$.

Analyses capturing this phenomenon typically invoke one of two approaches. The objective of the first is to describe the porous medium on a scale large enough for practical applications. To that end, this traditional approach uses partial differential equations (PDE) that incorporate retention as a constitutive law. The second approach exploits recent progress in direct numerical simulations and three-dimensional X-ray imaging to observe geometry and behavior of a smaller sample.

To establish the constitutive retention behavior of the medium, the first approach assumes a simplified view of the porous medium, such as a bundle of capillary tubes [67] or it invokes an analogous physical process, like magnetism [149, 154, 152, 153] or neural networks [184]. Parameters of the model are then fitted to experimental retention data. For example, Mualem [149] drew attention to the "ink-bottle" effect, whereby the total liquid content of a single bulging capillary at a given ψ is greater if capillarity thwarts expulsion of the liquid, than it is when the liquid is drawn into the bulge. This observation recognized the role played by connected cavities in setting the local saturation, and mainly attributed hysteresis to a distribution in capillary size. Crucially, Mualem [149] regarded unsaturated porous media as a collection of independent pores.

The chief limitation of the traditional approach is its reliance on macroscopic experiments to describe the overall constitutive behavior of unsaturated porous media. For example, Van Genuchten [214] put forth a convenient expression that is commonly adopted to characterize the water retention of soils. The model uses five parameters to fit experimental data. These include the liquid volume fraction θ_s at saturation, its residual value θ_r after the liquid ceases to percolate between the two boundaries across which ψ is applied, a characteristic capillary pressure ψ_a, and two exponents that are adjusted to reproduce the shape of the fluid retention curve.

If this simple model does not satisfactorily conform to data, other mathematical forms of the retention curve are chosen to minimize the number of additional empirical parameters needed to describe the entire range of S from saturation to complete dryness [163]. In the terminology of wet granulation [112], this range begins with the "funicular" regime near saturation, where percolation allows ψ to be felt through most of the liquid. It then transitions to the "pendular" regime, where liquid congregates near grain contacts [99]. Finally, liquid films condense or evaporate from surfaces within the porous solid [192]. Hysteresis is typically handled by adopting different values of fitting parameters for wetting and draining. A simpler description postulates that the two retention curves are related by the differential Eq. $\mathrm{d}f_w/\mathrm{d}\psi = (f_w - f_d)/\psi$ [161].

Traditionally, once established experimentally across a macroscopic sample, retention curves are then used to predict the effective permeability K of the porous medium in terms of its saturated value K_0, for example through the integral models of Burdine [35], Brooks and Corey [32] or Mualem [150, 151]. Retention curve and permeability are then incorporated into PDEs like that of [178]

$$(1-\nu)\frac{\partial S}{\partial t} = -\nabla \cdot \left[\frac{K}{\mu}\left(\rho \mathbf{g} + \frac{\partial \psi}{\partial S}\nabla S\right)\right], \tag{2.1}$$

which combines Darcy's law and mass conservation to predict the evolution of S over space and time for a liquid of density ρ and dynamic viscosity μ in a gravitational field g. Other formulations can also include other effects such as "non-Darcy" inertial behavior [3].

Unfortunately, experiments show that, if a large sample is subject to a pressure drop imposed across distant boundaries, the resulting hysteresis is more complicated than based upon the two unique "main" retention curves $S = f_d(\psi)$ and $S = f_w(\psi)$. For example, if the applied suction is reversed before fluid drains completely from the sample, the resulting overall saturation follows a path in the S vs ψ diagram that invades the region between f_d and f_w [210, 166, 211]. Although the function $f(\psi)$ appears continuous upon reversal, its derivative is not, and a new path $S = f(\psi)$ is opened each time the rate of change of ψ switches sign. In general, this "return-point memory" effect [190] indicates that the current state of a large sample depends upon details of its past history.

To address this difficulty, other treatments subsume hysteresis by introducing constitutive expressions that include state variables other than ψ and S, such as microscopic interface curvature [91], or by involving dynamic relaxation [16]. Averaging procedures based on moments of the Boltzmann equation [199] or methods consistent with thermodynamics [90] are then employed to build macroscopic governing equations for the evolution of these variables in space and time from physics at the microscopic scale [92, 17, 93]. However, to solve practical problems, the averaging still requires a measurable closure, such as a retention curve, to capture the constitutive behavior of the system.

The second, more recent approach begins with a detailed geometric description of the porous medium. Like direct numerical simulations, this method aims at reproducing the retention behavior by integrating PDEs on the pore scale that incorporate capillary, inertial and viscous forces [180, 95, 209, 217, 76]. Other treatments operate on an intermediate scale to handle uneven fluid distribution, for example in the pendular regime [88].

Recent experimental techniques, such as X-ray micro-tomography, have the potential to inform these numerical simulations by revealing the internal liquid distribution among cavities within porous solid matrices in great detail [220, 6, 117, 23, 187]. Here, a challenge is to relate the complex microscopic geometry of triple contact lines where gas, solid and liquid meet, to the macroscopic behavior of the porous medium [159]. Because the location and structure of these contact lines are affected by surface roughness and impurities that are difficult to discern or control, data interpretation and reproducibility are challenging.

As with other complex multiphase flows, the choice among the two approaches is mandated by overall system size. Because direct numerical simulations or three-dimensional experiments are rarely large enough to handle realistic applications, a formulation based on PDEs like Eq. (3.8) remains of practical interest. However, the complicated hysteresis observed on macroscopic samples has called into question the meaningfulness of the retention curve and the judiciousness of describing the filling state of an unsaturated porous media by saturation alone [91, 18]. If the traditional retention curve $S = f(\psi)$ is meaningful, is it so at any scale? Could it be derived from geometry and surface energies, rather than measured on a macroscopic sample?

In this context, we propose a statistical mechanics of unsaturated porous media at equilibrium. By limiting its scope to the mesoscopic scale, the theory predicts no invasion of the main retention curves. To present our analysis as clearly as possible, we deliberately adopt the simplest mean-field theory and illustrate it with generic examples. In this treatment, we simplify the complicated geometry of liquid distribution within the porous matrix, and adopt an "Ising model" that characterizes the state of a single cavity as being either full or empty. Adjacent cavities interact through the narrow openings that connect them, either by establishing gas-liquid interfaces when their filling state differs, or by not doing so when fluids are identical on both sides. We borrow from statistical mechanics terminology and call these openings "links" [41]. In the strict sense, a consequence of our assumptions is that results are only valid near saturation, unless the non-wetting fluid is also a liquid. However, the theory captures the behavior of the main fluid retention curves for a porous domain of known geometry and surface energies without parametric fitting.

We begin this article with a derivation of the theory. We then show how hysteresis of the main draining and wetting retention curves can be interpreted as a first-order phase transition in the ensemble of cavities, which we identify as the origin of Haines jumps [97]. To illustrate how the geometrical statistics of cavities and links affect the hysteresis, we consider porous media made of dense packings of spheres generated in numerical simulations. Finally, as with other physical phenomena where mean-field theory is invoked, such as magnetism [69], this equilibrium theory captures the behavior of "mesoscopic" domains that contain enough cavities to uphold statistical mechanics, yet are small enough to ignore gradients of capillary pressure. We suggest how it could be extended to inhomogeneous macroscopic samples through domain theory [123, 62, 61, 59, 60, 57], but warn that apparent retention curves in an inhomogeneous porous medium depend on the initial distribution of fluid.

2.2 Mean-field theory

We consider a void space of mean volume fraction $(1-\nu)$ delimited by internal surfaces of a porous solid, filled with two immiscible wetting and non-wetting fluids. For convenience, we refer to these respective fluids as a liquid and a gas, although the non-wetting fluid may be a liquid as well. Although this theory could also apply to a hydrophobic situation such as mercury porosimetry [94], thereby reversing the sign of capillary pressure, we illustrate it with hydrophilic porous solids relevant to soils.

The void space consists of many "cavities" of individual volume v_c and solid surface area a_c interconnected to n adjacent cavities of index i by narrow "links" of cross-sectional area $a_{\ell,i}$ (Fig. 2.1). For tractability, we adopt the Ising model [41] and assume that cavities contain only gas or liquid, with known surface energies $\gamma_{s\ell}$, $\gamma_{\ell g}$ and γ_{gs} between solid-liquid, liquid-gas, and gas-solid interfaces, respectively. Consistent with this simplest framework, we assign a binary filling state variable σ to each cavity, whereby $\sigma = +1$ denotes a cavity full of gas, while $\sigma = -1$ denotes one with liquid only.

We begin by evaluating the energy $\Delta E(-\sigma \rightarrow +\sigma)$ that must be supplied to a cavity to change its state from $-\sigma$ to $+\sigma$. Without loss of generality, we calculate the amount $\Delta E(-1 \rightarrow +1)$ that is needed to empty out a cavity initially full of liquid. This energy input can be decomposed into three parts. The first two are

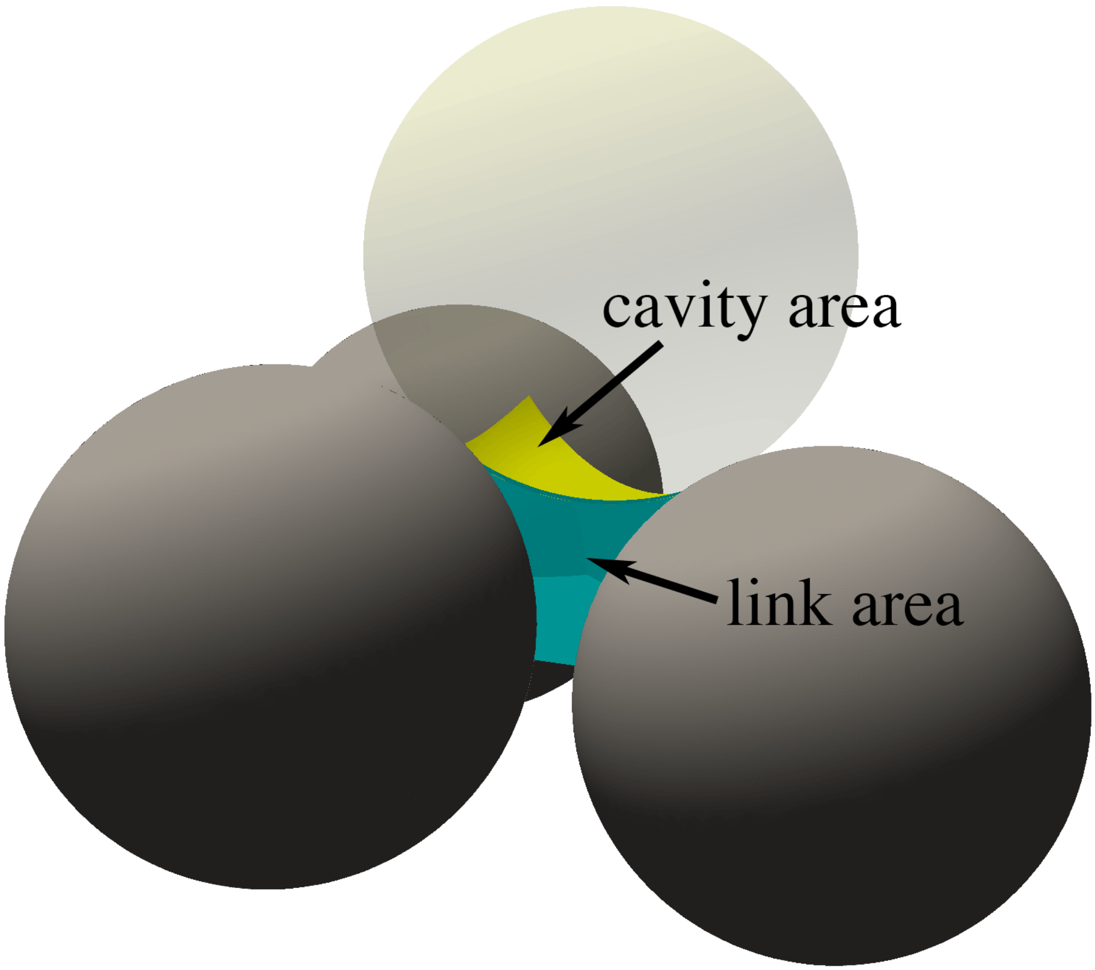

Figure 2.1: Single cavity wedged between an irregular tetrahedron of four spheres. The contribution of the top sphere to the cavity area is highlighted in yellow. The contribution of three spheres in the foreground to the link cross-section is shown in blue. Cartesian coordinates of the four spheres relative to their diameter and measured from their barycenter are $(x, y, z) = (0.05, -0.50, 0.26)$; $(-0.50, 0.05, -0.36)$; $(-0.14, 0.46, 0.51)$; $(0.58, -0.01, -0.42)$. For this cavity, $\lambda_0 \simeq 5.23$ and $\alpha_0 \simeq 3.20$.

independent of the state of neighboring cavities. They include the volume work

$$W = -\int_{v_c}^{0} (p_\ell - p_g) dv = -\psi v_c \tag{2.2}$$

that integrates elementary contributions needed to counteract the net pressure $(p_\ell - p_g) = -\psi$ resisting gas penetration into a liquid volume shrinking from v_c to zero. Then, the energy required to remove the liquid from the internal solid surface of area a_c is

$$\Gamma_c = (\gamma_{gs} - \gamma_{s\ell}) a_c = \gamma_{\ell g} a_c \cos\theta_c, \tag{2.3}$$

where θ_{c} is the static contact angle at the triple line where solid, liquid and gas meet.

The third contribution depends on the filling of all n connected cavities of index i. If the adjacent cavity i has no liquid ($\sigma_i = +1$), then emptying the cavity of interest involves the "exothermic" destruction of a gas-liquid interface. If instead cavity i is full ($\sigma_i = -1$), then the process entails the "endothermic" creation of a new such interface. Overall, the energy required is a sum over all adjacent cavities,

$$\Gamma_\ell = -\sum_{i=1}^{n} \sigma_i \gamma_{\ell g} a_{\ell,i}, \tag{2.4}$$

A similar argument shows that, for the opposite transformation ($\sigma = +1 \to \sigma = -1$), all signs are flipped in Eqs. (2.2)-(2.4). Therefore, in general, $\Delta E(-\sigma \to +\sigma) = (W + \Gamma_c + \Gamma_\ell)\sigma$. With the convenient (and inconsequential) choice of a ground state at $\sigma = 0$ halfway between a completely filled or a completely empty porous domain, the energy of a single cavity is then $E(\sigma) = (1/2)\Delta E(-\sigma \to +\sigma)$, or

$$E(\sigma) = \frac{1}{2}\left[-\psi v_{\mathrm{c}} + \gamma_{\ell \mathrm{g}} \cos\theta_{\mathrm{c}} a_{\mathrm{c}} - \sum_i \gamma_{\ell \mathrm{g}} a_{\ell,i} \sigma_i\right] \sigma. \tag{2.5}$$

In the mean-field theory [41], σ_i is approximated by the domain-average filling state $\bar{\sigma}$, recognizing that the relative fluctuation in σ among adjacent cavities is small if their number is large. Unlike problems of granular mechanics, what matters here is pore space contained *outside* the solid matrix. Therefore, in this article, $\overline{\varphi}$ denotes the volume-average of any state quantity φ over the domain of total *cavity* volume $V = \sum v_c$,

$$\bar{\varphi} \equiv \int \varphi f(\varphi) \mathrm{d}\varphi, \tag{2.6}$$

where $f(\varphi)$ is the normalized volume distribution of φ such that $\mathrm{d}v = V\, f(\varphi)\, \mathrm{d}\varphi$ is the elementary cavity volume distributed within the domain that has $\varphi \in [\varphi, \varphi + \mathrm{d}\varphi]$. With the self-consistent mean-field assumption $\sigma_i \simeq \bar{\sigma}$, Eq. (2.5) becomes

$$E(\sigma) = \frac{1}{2}\left[-\psi v_{\mathrm{c}} + \gamma_{\ell \mathrm{g}} \cos\theta_{\mathrm{c}} a_{\mathrm{c}} - \gamma_{\ell \mathrm{g}} a_{\ell} \bar{\sigma}\right] \sigma, \tag{2.7}$$

where $a_\ell \equiv \sum a_{\ell,i}$ is the total cross-sectional area of all links connected to the cavity of interest. In a disordered porous material, v_c, a_c and a_ℓ are random variables. For a crystal of like particles, they instead possess discrete values.

In the framework of statistical mechanics, we consider an ensemble of identical copies of a porous mesoscopic sample at equilibrium containing a large number of cavities. Each copy has a distinct distribution of filling states. Copies with similar total energy in Eq. (2.7) form a microstate with Bose-Einstein statistics (i.e. there is no limitation on the number of cavities holding a given filling state). Then, according to the Maxwell-Boltzmann distribution [41], the probability to find a cavity at the filling state σ, subject to the constraints of a given ensemble-average energy and total number of copies in the ensemble is

$$\Pr(\sigma) = \frac{1}{Z} e^{-\beta E(\sigma)}, \tag{2.8}$$

where β is a Lagrange multiplier and Z is the partition function

$$Z = e^{-\beta E(+1)} + e^{-\beta E(-1)}. \tag{2.9}$$

The expected filling state in the cavity of interest is then

$$\begin{aligned} \langle \sigma \rangle &= \sum_{\sigma=\pm 1} \sigma \, \mathrm{Pr}(\sigma) \qquad (2.10) \\ &= \tanh \left\{ \frac{\beta}{2} \left[\gamma_{\ell \mathrm{g}} a_\ell \bar{\sigma} + \psi v_{\mathrm{c}} - \gamma_{\ell \mathrm{g}} a_{\mathrm{c}} \cos \theta_{\mathrm{c}} \right] \right\}, \end{aligned}$$

where $\langle \varphi \rangle$ denotes the ensemble-average of any state quantity φ over all copies of the sample.

This expression prescribes how the problem should made dimensionless. First, we define the characteristic length

$$\bar{\ell}_0 \equiv (\bar{v}_{\mathrm{c}_0})^{1/3} \tag{2.11}$$

based on the domain-average dry cavity size $\bar{v}_{\mathrm{c}_0}$, which only depends on geometry of the host solid constituting the porous matrix. Then, the dimensionless capillary pressure can be written

$$\psi' \equiv \psi \bar{\ell}_0 / \gamma_{\ell g}. \tag{2.12}$$

Similarly, dimensionless link cross-section and cavity surface areas are

$$\lambda \equiv a_\ell \bar{\ell}_0 / v_c \tag{2.13}$$

and

$$\alpha \equiv a_c \bar{\ell}_0 / v_c, \tag{2.14}$$

such that Eq. (2.10) becomes

$$\langle \sigma \rangle = \tanh \left[(\beta'/2) \left(\lambda \bar{\sigma} + \psi' - \alpha \cos \theta_{\mathrm{c}} \right) \right], \tag{2.15}$$

where $\beta' \equiv \beta\gamma_{\ell g} v_c/\bar{\ell}_0$.

In Appendix A.1, we show that $\beta' \gg 1$, which allows us to simplify the hyperbolic tangent in Eq. (2.10), which effectively becomes the Heaviside function $\mathbb{H}(\psi - \psi_c)$ jumping from -1 to $+1$ at a dimensionless transition pressure is

$$\psi_c' = \alpha\cos\theta_c - \lambda\bar{\sigma}. \tag{2.16}$$

Then, in a domain where cavities and links are not uniform, the domain-average expected filling state is

$$\overline{\langle\sigma\rangle} = \int_{\lambda=0}^{\infty}\int_{\alpha=0}^{\infty} \langle\sigma\rangle F \,\mathrm{d}\lambda\mathrm{d}\alpha = \iint \mathbb{H}(\psi - \psi_c)\, F \,\mathrm{d}\lambda\mathrm{d}\alpha, \tag{2.17}$$

where $F(\lambda, \alpha)$ is the normalized joint distribution function by volume of λ and α in Eqs. (2.13)-(2.14), such that

$$\mathrm{d}v = V\, F \,\mathrm{d}\lambda\mathrm{d}\alpha \tag{2.18}$$

is the elementary cavity volume distributed within the domain of total cavity volume V that has $\lambda \in [\lambda, \lambda + \mathrm{d}\lambda]$ and $\alpha \in [\alpha, \alpha + \mathrm{d}\alpha]$.

For an ergodic system at equilibrium,

$$\bar{\sigma} = \overline{\langle\sigma\rangle}, \tag{2.19}$$

so that Eq. (2.17) can be written

$$\bar{\sigma} = \mathbb{I}(\bar{\sigma}, \psi'; \theta_c), \tag{2.20}$$

where $\mathbb{I}$ is the integral function

$$\mathbb{I}(\bar{\sigma}, \psi'; \theta_c) \equiv \iint\limits_{\Omega_+} F \,\mathrm{d}\lambda\mathrm{d}\alpha - \iint\limits_{\Omega_-} F \,\mathrm{d}\lambda\mathrm{d}\alpha, \tag{2.21}$$

and Ω_+ and Ω_- are complementary non-intersecting regions filling the parameter space (λ, α) and satisfying

$$\Omega_\pm \Leftrightarrow \lambda\bar{\sigma} + \psi' - \alpha\cos\theta_c \gtrless 0. \tag{2.22}$$

Meanwhile, because $\sigma = \mp 1$ for cavities filled with liquid and gas, respectively, the domain-average $\bar{\sigma}$ is related to the liquid volume fraction through

$$\theta = (1 - \nu)(1 - \bar{\sigma})/2, \tag{2.23}$$

or, equivalently, $S = (1-\bar{\sigma})/2$. Therefore, a stable solution of Eq. (2.20) at a given ψ' yields a point on the retention curve of θ vs ψ'. Finally, the conjecture $\beta' \gg 1$ invoked earlier would explain why retention curves are typically insensitive to absolute temperature.

2.3 Phase transition and hysteresis

We now identify the hysteretic behavior of an unsaturated porous domain as resulting from first-order phase transitions in the ensemble. Such transitions occur, for example, as an initially saturated sample abruptly drains most of its liquid or, conversely, when an initially dry sample suddenly jumps toward saturation.

To illustrate these transitions, it is instructive to examine the simplest case of an ordered porous domain with single-valued v_s, a_c and a_ℓ. For instance, we consider a hypothetical foam consisting of identical hollow spherical cavities with circular links carved in a solid on a regular cubic lattice. (A more realistic, albeit more complicated hexagonal close-packed crystal is analyzed in the supporting information). For the foam, F is a delta-function located at (λ, α) (square symbol in either sides of Fig. 2.2). The middle graph in Fig. 2.2 shows the resulting retention curves. Because F is a normalized delta-function in this example, the two integrals on the right of Eq. (2.20) are unity if ψ belongs to the

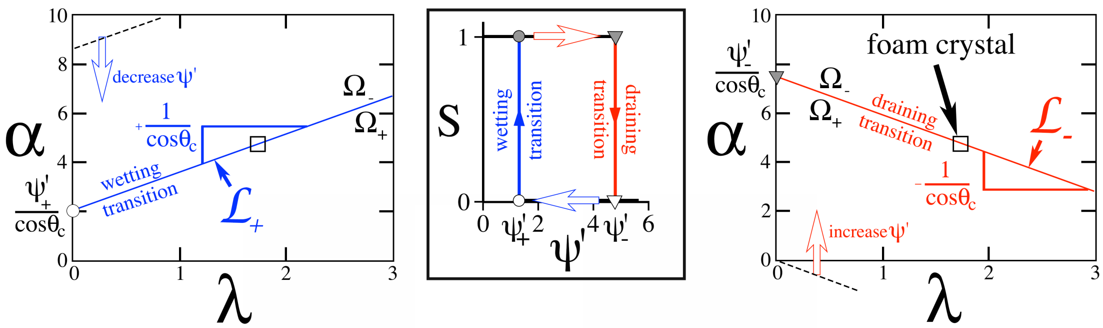

Figure 2.2: Middle graph: Retention curves of saturation S vs dimensionless capillary pressure ψ' for a hypothetical foam of identical spherical cavities on a square lattice with solid volume fraction $\nu = 0.3$, having single-valued $\lambda_0 = 1.530\cdots$ and $\alpha_0 = 4.735\cdots$. As Appendix A.5 suggests, $\lambda \simeq 1.73$ and $\alpha \simeq 4.74$ for the contact angle $\theta_c = 50°$ in this example. Arrows show directions of changes in ψ'. Right: draining transition in the graph of α vs λ. For this foam, F is a delta-function centered on the square symbol. The black dashed line marks the border in Eq. (2.22) between domains Ω_+ below the line and Ω_- above, with $\psi' = 0$. The red line $\mathcal{L}_-$ is the corresponding border for the draining phase transition, which occurs when ψ', rising in the direction of the red arrow, reaches ψ'_-. Left: as ψ' decreases in the direction of the blue arrow, it eventually reaches the wetting transition at $\psi'_+ \simeq 1.31$.

domain of integration, and zero otherwise. Therefore, their combination can only take one of three values $(-1, 0, +1)$.

Consider first an initially saturated sample with $\bar{\sigma} = -1$ and $\psi' = 0$ (black dashed line in the right "draining" graph of Fig. 2.2), for which the entire (λ, α) space is occupied by Ω_- (Eq. 2.22). At small capillary pressure, the delta-function at (λ, α) remains within Ω_- until ψ' reaches

$$\psi'_- \equiv \alpha \cos\theta_c + \lambda. \tag{2.24}$$

Then, because $\mathbb{I} = -1$, $\forall \psi' < \psi'_-$, Eq. (2.20) is satisfied and, consequently, $\bar{\sigma} = -1$ remains its solution throughout the range $\psi' < \psi'_-$. As section 2.4 will show, this solution (filled triangle in Fig. 2.2) is stable. However, for $\psi' > \psi'_-$, $\bar{\sigma} = -1$ ceases to be a solution, forcing the system to jump to the other stable solution $\bar{\sigma} = +1$ marked by an open triangle in Fig. 2.2. In short, the porous domain remains saturated until ψ' reaches ψ'_-.

A similar argument implies that an initially dry sample with $\bar{\sigma} = +1$ and $\psi' \to \infty$ stays dry as ψ' is progressively decreased within the range $\psi'_+ < \psi' < +\infty$ (Fig. 2.2, left graph), where

$$\psi'_+ \equiv \alpha \cos\theta_c - \lambda. \tag{2.25}$$

Because $\psi'_+ < \psi'_-$, an initially saturated sample with $\bar{\sigma} = -1$ transitions abruptly to the other solution $\bar{\sigma} = +1$ of Eq. (2.20) as ψ' increases beyond ψ'_-. Conversely, an initially dry sample jumps to saturation as ψ' falls below ψ'_+. In short, the porous domain with single-valued λ and α undergoes a hysteresis loop marked by two abrupt phase transitions such that

$$\begin{aligned} S &= f_d(\psi') = \mathbb{H}(\psi'_- - \psi') \\ S &= f_w(\psi') = \mathbb{H}(\psi'_+ - \psi'), \end{aligned} \tag{2.26}$$

for draining and wetting, respectively. Because these transitions arise as an external field (viz. the capillary pressure ψ') passes through a critical point at which the total system energy per unit cavity volume $\mathcal{H} \equiv (1/V)\sum E(\sigma_i)$ is discontinuous, they are classified as "first-order" phase transitions [190].

In this crystalline geometry, the "air-entry potential", i.e. the capillary pressure at which a saturated sample begins to drain, is $\psi_- = \gamma_{\ell g}(\alpha\cos\theta_c + \lambda)/\bar{\ell}_0$. Then, the separation $\Delta\psi' \equiv (\psi'_- - \psi'_+)$ between the two transition pressures is a measure of hysteresis strength,

$$\Delta\psi' = 2\lambda. \tag{2.27}$$

By the definition of λ in Eq. (2.13), the hysteretic separation for single-valued a_ℓ, a_c and v_c is therefore governed by the link area relative to the $(2/3)$ power of the cavity volume.

2.4 Collective behavior in a disordered medium

Traditional treatments regard unsaturated porous media as a collection of independent pores, each acting as a separate domain, and each having an individual critical capillary pressure for wetting and another for draining. In that view, a pore contributes to decreasing the average retention of the whole draining medium by emptying once its own critical pressure is reached; conservely, upon wetting the medium, each pore fills up after ψ decreases below another, lower threshold [149].

Our approach is radically different. The self-consistent integral formulation of Eqs. (2.20)-(2.22) implies that the entire unsaturated porous domain contributes collectively to its equilibrium solution, rather than as a superposition of individual transitions. In our mean-field analysis, cavities are interconnected to the bulk filling index $\bar{\sigma}$ through the links they each possess. Therefore, the hysteresis of our retention curve is determined by the entire distribution function F, rather than by averaging retention curves of individual cavities.

To show how such collective behavior arises in the statistical mechanics, we now consider a porous domain with a broad distribution $F(\lambda, \alpha)$, illustrated with random, polydisperse, dense packings of spheres obtained in numerical simulations [176] (Fig. 2.3). Appendix A.2 outlines how F is calculated from a knowledge of the positions of sphere centers and their diameter.

Unlike the crystal example in section 2.3, the integral function $\mathbb{I}$ no longer takes on discrete values, but adopts instead a sigmoidal shape. Figure 2.4 illustrates the search for solutions to Eq. (2.20) by superposing $\mathbb{I}$ vs $\bar{\sigma}$ and the diagonal representing the ergodic condition $\overline{\langle \sigma \rangle} = \bar{\sigma}$. In general, there can be

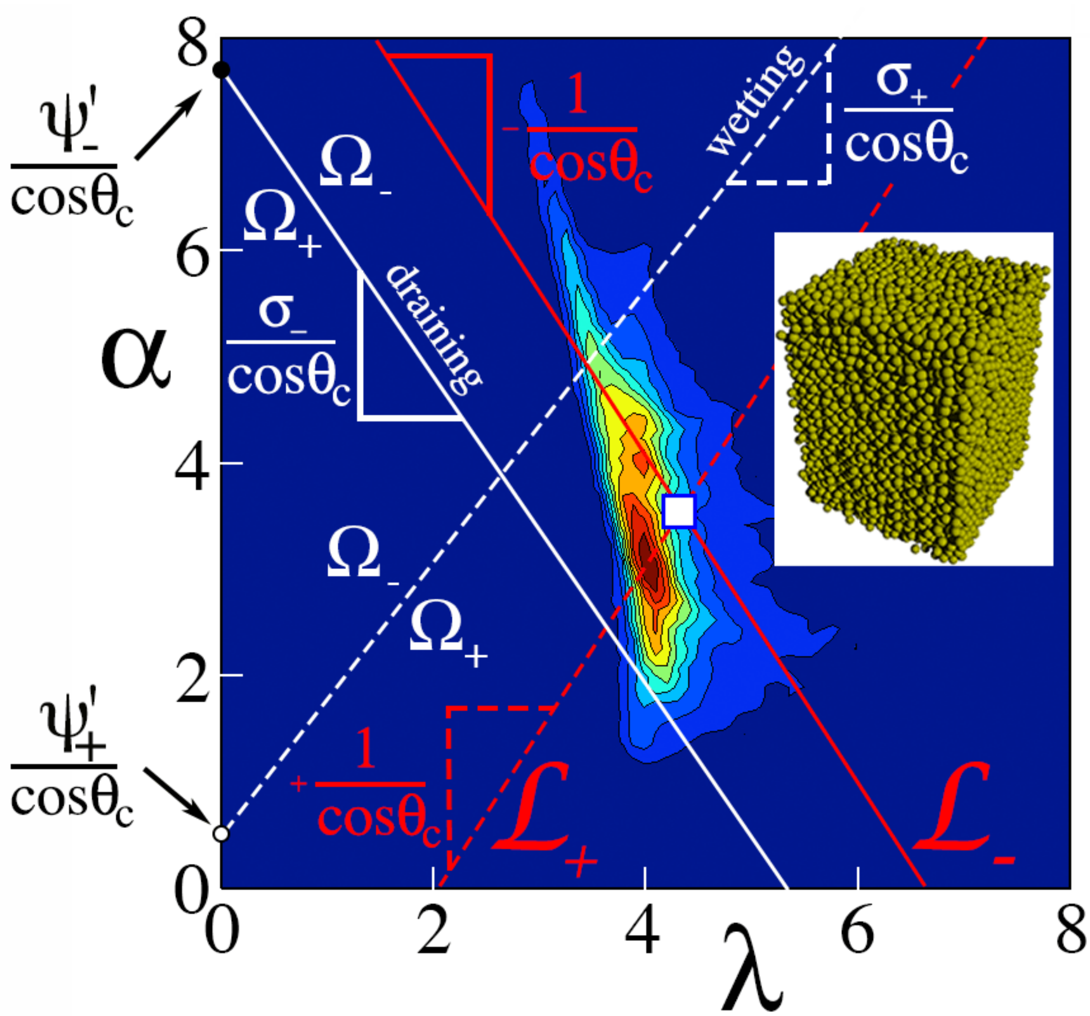

Figure 2.3: Contour plot of the distribution $F(\lambda, \alpha)$ for the random packing shown in the inset with 20,000 spheres forming 123,914 cavities at $\nu = 0.604$ (detail in Fig. 2.1). The Delaunay triangulation mentioned in Appendix A.2 yields $\bar{\ell}_0/d \simeq 0.389$, $\bar{\lambda}_0 \simeq 3.81$ and $\bar{\alpha}_0 \simeq 3.55$. For a contact angle $\theta_c = 50°$, $\bar{\lambda} \simeq 4.32$. The open square marks the "center of mass" of F defined in Eqs. (A.3) and (A.4). The white solid line of slope $\sigma_-/\cos\theta_c$ and intercept $\psi'_-/\cos\theta_c$ is the boundary between the regions Ω_+ and Ω_- in Eq. (2.22) when the mesoscopic domain undergoes its draining phase transition at the capillary pressure $\psi'_- \simeq 4.98$ and filling state $\sigma_- \simeq -0.925$ ($S \simeq 0.96$). The white dashed line is the wetting phase transition with $\psi'_+ \simeq 0.35$ and filling state $\sigma_+ \simeq +0.820$ ($S \simeq 0.09$). The red solid and dashed lines (respectively called $\mathcal{L}_-$ and $\mathcal{L}_+$ in Fig. 2.2) mark the corresponding transitions for a hypothetical porous medium with single-valued cavity and link sizes having the same $\bar{\lambda}$ and $\bar{\alpha}$.

(Numerical simulation courtesy of Patrick Richard)

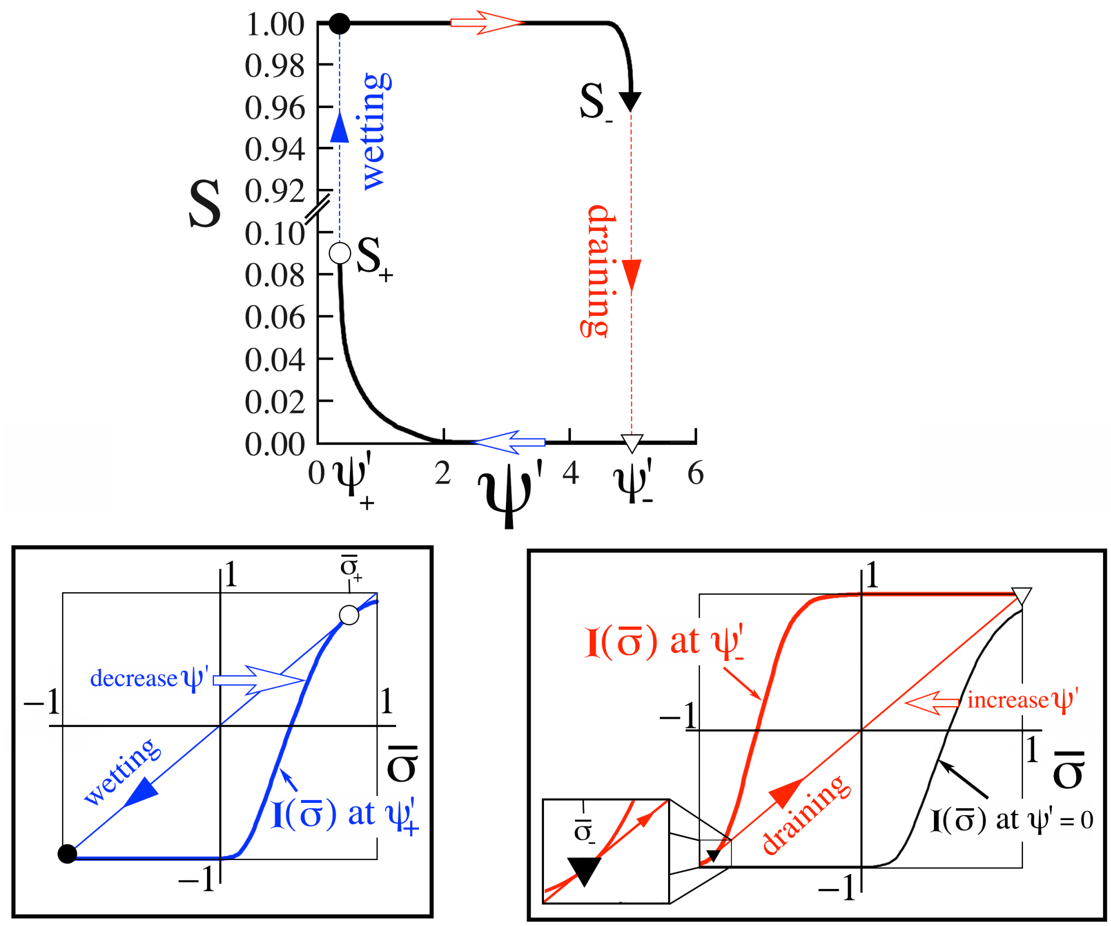

Figure 2.4: Top: wetting and draining retention curves of saturation $S = \theta/(1-\nu)$ vs dimensionless capillary pressure $\psi' = (p_g - p_\ell)/\gamma_{\ell g}\bar{\ell}_0$ for the distribution $F(\lambda, \alpha)$ in Fig. 2.3 and $\theta_c = 50°$. Bottom right: integral $\mathbb{I}$ and domain-averaged expected filling state $\overline{\langle\sigma\rangle}$ vs $\bar{\sigma}$ as ψ' is increased from zero ($\mathbb{I}$, black line) to its value $\psi'_- \simeq 4.98$ at the draining phase transition, beyond which the filling state must jump from $\bar{\sigma}_- \simeq -0.925$ (or $S_- \simeq 0.963$, filled triangle) to $\bar{\sigma} \simeq +1$ (open triangle), as $\mathbb{I}$ (red sigmoidal line) no longer intersects the diagonal to satisfy Eq. (2.20). Bottom left: the corresponding graphs of $\mathbb{I}$ and $\overline{\langle\sigma\rangle}$ vs $\bar{\sigma}$ as ψ' is decreased from $+\infty$ to $\psi'_+ \simeq 1.31$ at the wetting transition (open to filled circles) with $\bar{\sigma}_+ \simeq 0.820$ (or $S_+ \simeq 0.090$).

one, two or three solutions at intersections of the sigmoidal and diagonal lines in Fig. 2.4.

To establish whether anyone is stable, we must first determine causality among state variables. On the one hand, the mean filling state $\bar{\sigma}$ determines the regions $\Omega_\pm$ of integration of $\mathbb{I}$ or, in short, $\bar{\sigma} \Rightarrow \mathbb{I}$. Conversely, ergodicity implies that knowledge of the expected filling state $\overline{\langle\sigma\rangle} = \mathbb{I}$ leads to knowledge of $\bar{\sigma}$, i.e. $\overline{\langle\sigma\rangle} \Rightarrow \bar{\sigma}$. By determining whether the domain returns to a solution upon small excursions away from it, these causal relations indicate that, out of three solutions, the middle one is unstable, while the others at low and high filling are both stable. (Instability of the middle solution explains why we ignored $\bar{\sigma} = 0$ for the example in section 2.3).

Consider an initially saturated domain ($\bar{\sigma} = -1$) without capillary pressure ($\psi' = 0$) (bottom right Fig. 2.4). Here, $\lambda\bar{\sigma} + \psi' - \alpha\cos\theta_c < 0, \forall(\lambda, \alpha)$, so that Ω_- represents the entire (λ, α) space shown in Fig. 2.3, and $\mathbb{I} = -1$. This saturated state is a single solution of Eq. (2.20) represented by the lower left corner in the bottom right graph of Fig. 2.4. As capillary pressure is increased, the $\mathbb{I}$-curve shifts leftward, until one, then two new intersections arise beside the lower left solution near $\bar{\sigma} \sim -1$. Yet, because this solution is stable, any other solution is ignored and the domain remains near saturation. However, as ψ' increases, the sigmoidal curve eventually moves too far leftward to intersect the diagonal near saturation. At the pressure ψ'_- (filled triangle), the whole domain undergoes a first-order phase transition whereby $\bar{\sigma}$ changes sign and jumps to the dryer solution on the upper right (open triangle). The top graph in Fig. 2.4 traces the resulting path in the diagram of saturation $\bar{S}$ vs dimensionless capillary pressure ψ'.

Now consider the draining process, which begins with a stable $\bar{\sigma} \to +1$ as $\psi' \to \infty$ (left graph in Fig. 2.4). As capillary pressure is progressively released, dry states remain stable until the sigmoidal curve at $\psi' = \psi'_+$ intersects the diagonal at only one point (open circle). At lower capillary pressures, the domain must then jump to its other solution closer to saturation (filled circle).

As with the crystal in section 2.3, the theory suggests that the transition pressure upon wetting is greater than that upon draining, $\psi'_- > \psi'_+$, so hysteresis arises once again. However, as Appendix A.3 shows, the difference $\Delta\psi' \equiv \psi'_- - \psi'_+$ is always smaller with a broadly-distributed F than with single-valued λ and α. Therefore, in general,

$$\Delta\psi' \equiv \psi'_- - \psi'_+ < 2\bar{\lambda}. \tag{2.28}$$

Meanwhile, the form of Eq. (2.22), which marks the border between the domains Ω_- and Ω_+ in the (λ, α) parameter space, implies that the air entry potential ψ'_- shifts toward higher values as $\bar{\alpha}$ increases, consistent with the crystal example in Eqs. (2.24)-(2.25).

Figure 2.5 confirms these trends with retention curves calculated from artificial distributions $F(\lambda, \alpha)$ having a simple analytical form. In short, increasing $\bar{\lambda}$ strengthens the hysteresis, i.e. it widens the gap between wetting and draining curves without shifting their mid-position along the pressure axis (bottom Fig. 2.5, compare curves for larger $\bar{\lambda}$ with the base case). In contrast, increasing $\bar{\alpha}$ translates the mid-position toward higher ψ' without affecting hysteresis strength (top Fig. 2.5, as $\bar{\alpha}$ is raised). Lastly, spreading the function $F(\lambda, \alpha)$ along either axis reduces hysteresis strength (see curves for "wider" F), to the point that hysteresis can disappear altogether (Fig. 2.5, with "wider" F_α).

Even in the example of Figs. 2.3-2.4 with monodisperse spheres, the retention curves exhibit a more gradual draining and wetting transitions than in section 2.3, as the function $F(\alpha, \lambda)$ is no longer a delta-function. More generally, a wider particle-size-distribution (PSD) should induce greater spread in F, and therefore less hysteresis and a more gradual transition roll-off. Then, for exam-

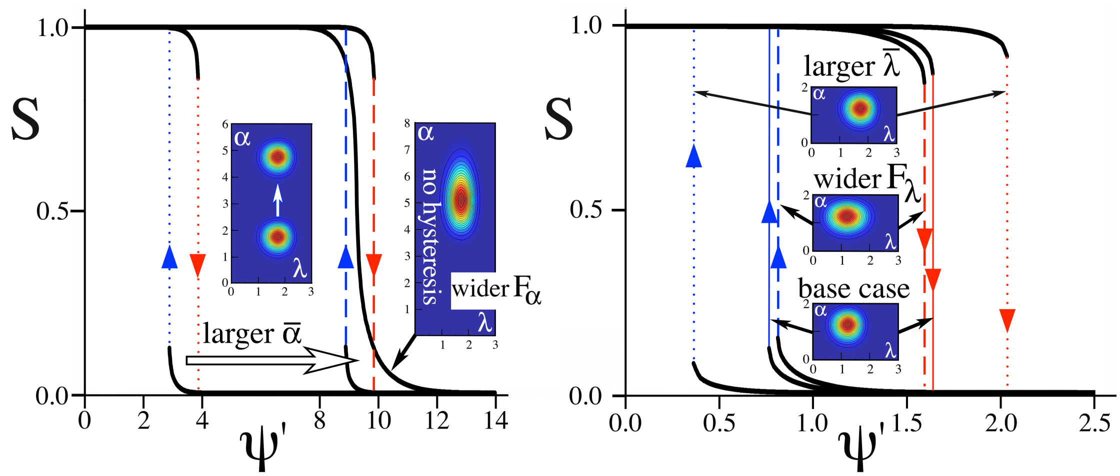

Figure 2.5: Dependence of retention curves $S = S(\psi')$ on $F(\lambda, \alpha)$, illustrated with artificial gamma-distributions of the form $F = F_\lambda \times F_\alpha$, where $F_\lambda = (\lambda - d_\lambda)^{a_\lambda c_\lambda - 1} \exp\{-[(\lambda - d_\lambda)/b_\lambda]^{c_\lambda}\}$ for $\lambda > d_\lambda$ and zero otherwise, and $F_\alpha = (\alpha - d_\alpha)^{a_\alpha c_\alpha - 1} \exp\{-[(\alpha - d_\alpha)/b_\alpha]^{c_\alpha}\}$ for $\alpha > d_\alpha$ and zero otherwise. Insets show the corresponding contours of $F(\lambda, \alpha)$ where blue is $F = 0$ and red is maximum F. Vertical blue and red arrows and lines mark, respectively, wetting and draining phase transitions. Top graphs: white arrows show how hysteretic retention curves are affected by an increase in the mean value of α from $\bar{\alpha} \simeq 1.7$ to 4.7 (respective phase transitions represented by dotted and dashed lines), while keeping $\bar{\lambda} \simeq 1.7$ and the standard deviations of F_α and F_λ at 0.32. The retention curve without hysteresis (uninterrupted solid line without phase transition) is obtained from F in the "no hysteresis" inset having $\bar{\alpha} \simeq 4.7$, a wider standard deviation 0.72 for F_α, and the same F_λ as above. Bottom graphs, from lowest to highest insets: "base case" for $F_\alpha = F_\lambda$ with a standard deviation of 0.32 and $\bar{\lambda} \simeq 1.2$ (solid blue and red transition lines); case of a "wider F_λ", in which the standard deviation of F_λ is increased to 0.42 (dashed transition lines); case of a "larger $\bar{\lambda}$" where $\bar{\lambda}$ alone is increased to 1.7 from the base case (dotted lines).

ple, this theory suggests that a sand with relatively narrow PSD should have significant hysteresis. However, if the same sand also included fine particles, the strength of its hysteresis should be diminished.

Because the theory is built upon actual areas and volumes through λ and α, it tacitly accounts for interface deformations caused by a contact angle $\theta_c \neq \pi/2$, in addition to the explicit $\cos\theta_c$ appearing in Eq. (2.22). However, it is difficult to determine the distribution $F(\lambda, \alpha)$ with complicated gas-liquid interfaces. Instead, it is more straightforward to find its counterpart $F_0(\lambda_0, \alpha_0)$ on a dry sample, which is equivalent to $\theta_c = \pi/2$, for example by employing the Delaunay triangulation mentioned in Appendix A.2. Then, one can estimate how a contact angle $\neq \pi/2$ affects interface area and cavity volume. As Appendix A.5 shows, unless λ_0 is relatively large, values of $\theta_c < \pi/2$ mainly affect λ by raising it uniformly, as estimated in Eq. (A.12), thereby exacerbating hysteresis strength.

2.5 Mesoscopic domain size

An important feature of this equilibrium theory is that it applies to a mesoscopic domain with a limited number of successive nearest neighbors. To estimate the size of this domain, we calculate in Appendix A.4 the probability $\mathrm{Pr}_c(m)$ that the m-th nearest neighbor has the same filling state as the original cavity of index $m = 0$. Then, a measure of the mesoscopic domain size is the value of m where $\mathrm{Pr}_c(m)$ approaches zero. If tortuosity of the porous medium is known [216, 164], then m can be converted to a correlation length. We find

$$\mathrm{Pr}_c = (1 - S)^{m+1} + S^{m+1}. \tag{2.29}$$

As expected, Pr_c decays with m ever more slowly as the system approaches either the dry state or its saturated counterpart. A prediction of Eq. (2.29) is that the mesoscopic domain is at its smallest when $S = 1/2$, which arises as the porous medium transitions from saturation and dryness.

A more objective measure of the correlation index m_c at which Pr_c has decayed substantially is the integral scale

$$m_c = \int_{m=0}^{\infty} \mathrm{Pr}_c \mathrm{d}m = -\left[\frac{S}{\ln S} + \frac{1 - S}{\ln(1 - S)}\right]. \tag{2.30}$$

For the dense spherical packing with retention behavior in Figs. 2.3–2.4, this scale is $m_{c_-} \simeq 25$ and $m_{c_+} \simeq 10$ at the draining and wetting transitions S_- and S_+, respectively. It is consistent with observations [10]. Here, wetting occurs over a smaller mesoscopic region than draining. Because both m_{c_-} and m_{c_+} just fit within the simulation domain having approximately $24 \times 24 \times 31$ spheres in x-, y- and z-directions, the inset in Fig. 2.3 illustrates how small a mesoscopic domain of identical spheres can typically be.

2.6 Haines jumps

Because our equilibrium theory ignores time and gradients in state variables, it addresses the limit of negligible inertial and viscous forces. However, its results can shed light on fluid behavior during phase transitions.

For inertial forces to be significant, the Weber number We $\equiv \rho u^2 \bar{\ell}_0 / \gamma_{\ell g}$ typically exceeds unity [230], where u is a characteristic interstitial flow speed. For example, inertial forces only become significant if water seepage during the wetting or draining transitions produces a speed $u \gtrsim 1\,\mathrm{m/s}$ in a sand bed with $\bar{\ell}_0 \sim 50\,\mu\mathrm{m}$. However, neglecting viscous forces typically requires lower capillary number Ca $\equiv \mu u / \gamma_{\ell g} < 10^{-5}$ [215], and therefore much lower speeds.

In this context, we expect viscosity to play a role during rapid fluid rearrangements called "Haines jumps" [80]. Berg et al. [23] and Moebius and Or [147] observed such events in 3D and 2D experiments, respectively, and Ferrari et al. [68] reproduced them in numerical simulations. Conversely, we do not expect viscosity to matter during the slower, reversible [226] redistribution of fluid that Berg et al. [23] also noted for a substantial fraction of the displaced volume, and which we interpret as the reversible approach to a phase transition. In this section, we suggest that Haines jumps are related to the first-order phase transitions described in earlier sections. To this end, we exploit our theory to interpret recent measurements of fluid speed by [10].

In those experiments, Haines jumps arose as water was drained from an artificial porous medium by injecting immiscible non-wetting decane at controlled flow rates. Unlike the air/water system in which the gas cannot hold tensile stresses, negative pressures percolated through both liquids at any S, and therefore we expect the theory to hold even at low water saturation. Because the porous solid medium was etched into glass on an hexagonal pattern with uniform cavities and links, the retention curves possessed the Heaviside shape in Fig. 2.2. From its known geometry and contact angle (caption of Fig. 2.6), we calculate $\lambda \simeq 0.627$ using Eq. (A.12). Such relatively small λ should produce modest hysteresis.

To predict the behavior in Haines jumps, we first calculate the total energy $\mathcal{H}$ in a unit volume of the mesoscopic domain by summing Eq. (2.7) over all cavities. For this monodisperse crystal, it is, in dimensionless form,

$$\mathcal{H}' = (\bar{\sigma}/2)(-\psi' + \alpha \cos\theta_c - \bar{\sigma}\lambda). \tag{2.31}$$

Then, the draining first-order phase transition produces a dimensionless "latent energy" per unit volume $\mathbb{L}'_- = \mathcal{H}'(\psi'_-, \bar{\sigma} = +1) - \mathcal{H}'(\psi'_-, \bar{\sigma} = -1) = -\psi'_- + \alpha \cos\theta_c$. Similarly, the wetting transition has $\mathbb{L}'_+ = +\psi'_+ - \alpha \cos\theta_c$. Substituting transition pressures in Eqs. (2.24)-(2.25), both transitions have the same dimensionless volumetric latent energy

$$\mathbb{L}' = -\lambda, \tag{2.32}$$

Therefore, they are both "exothermic" and should occur spontaneously.

Such latent energy is absorbed by viscous interactions of the two fluids within the porous solid. To model this dissipation mechanism as simply as possible, we consider an open rectilinear mesoscopic domain of uniform saturation with coordinate $-m_c\ell_0 < x < m_c\ell_0$. In a transition, volume conservation $\partial S/\partial t = -S\partial u/\partial x$ relates the gradient in water velocity u to temporal variations in S, and it binds decane and water velocities through $u_d = -uS/(1-S)$. Taking $u = 0$ midway through the domain, the ODE integrates to $u = -x\partial \ln S/\partial t$ or, equivalently, $u = 2\bar{u}x/(m_c\ell_0)$, where

$$\bar{u} = -\left(m_c\ell_0/2\right)\partial \ln S/\partial t \tag{2.33}$$

is the domain-average speed.

Meanwhile, viscous forces exerted by water and decane in a unit cavity volume are $\mu u(1-\nu)S/K$ and $\mu_d u_d(1-\nu)(1-S)/K_d$, where K and K_d are Carman-Kozeny permeabilities corrected for the respective incomplete saturations S and $(1-S)$ of water and decane, and μ and μ_d are their respective viscosities. In the integral model of Burdine [35], a Heaviside-shaped retention curve yields $K/K_0 = S^{n_b}$ and $K_d/K_0 = (1-S)^{n_b}$, where $K_0/(1-\nu) \simeq (d^2/180)[(1-\nu)/\nu]^2$, and $n_b \simeq 3$. From the periodic unit cell volume of V_{cell}, we calculated the Carman-Kozeny equivalent "particle diameter" $d = (6\nu V_{\text{cell}}/\pi)^{1/3}$.

Because the overall energy in Eq. (2.31) is proportional to $\bar{\sigma}$ to first order, the average rate of latent energy produced is approximately $-(\partial S/\partial t)|\mathbb{L}'|\gamma_{\ell g}/\ell_0$ during a draining phase transition in which S remains uniform in the mesoscopic domain. It balances the combined energy dissipation rate $\mu u^2(1-\nu)S/K + \mu_d u_d^2(1-\nu)(1-S)/K_d$ from viscous forces on both fluids averaged over the whole mesoscopic domain. Because $u \propto x$, the domain-average of u^2 is $(4/3)\bar{u}^2$.

In short, the energy balance is

$$-\left(\frac{|\mathbb{L}'|\gamma_{\ell g}}{\ell_0}\right)\frac{\partial S}{\partial t} = 180\left(\frac{\nu}{1-\nu}\right)^2 \frac{4}{3}\left(\frac{S\bar{u}}{d}\right)^2 \times \left[\frac{\mu}{S^{n_b+1}} + \frac{\mu_d}{(1-S)^{n_b+1}}\right]. \tag{2.34}$$

Substituting the continuity Eq. (2.33) and introducing the reference speed $u_0 \equiv |\mathbb{L}'|\gamma_{\ell g}/(180\mu)[(1-\nu)/\nu]^2(d/\ell_0)^2$ and time $\tau_0 \equiv \ell_0/u_0$, Eqs. (2.33)-(2.34) are, in dimensionless form where $t' \equiv t/\tau_0$ and $u' \equiv \bar{u}/u_0$,

$$\partial \ln S/\partial t' = -2u'/m_c \tag{2.35}$$

and

$$u' = \frac{3}{2Sm_c}\left[\frac{(1-S)^{n_b+1} S^{n_b+1}}{(1-S)^{n_b+1} + \mu' S^{n_b+1}}\right], \tag{2.36}$$

where $\mu' \equiv \mu_d/\mu$ is the ratio of viscosities of the non-wetting and wetting fluids. Equation (2.36) predicts that the mean dimensionless velocity peaks at a value u'_{max} that depends on this ratio through $\ln u'_{\text{max}} \simeq -0.03620 \ln \mu'^2 - 0.4206 \ln \mu' - 2.745$ in the range $10^{-3} < \mu' < 10^3$, at a saturation given by $\ln S_{\text{max}} \simeq -0.00472 \ln \mu'^2 - 0.0849 \ln \mu' - 0.7340$. In the experiments of Armstrong and Berg [10], the maximum Weber number is $\sim 1.2\ 10^{-3}$, which is too low for inertial forces to matter. However, if Armstrong and Berg [10] had used air ($\mu' \simeq 0.02$) rather than decane ($\mu' \simeq 0.96$) as non-wetting fluid, the peak speed would have been about 2.7 times faster, yet not large enough for inertia to become important.

To solve this problem, we first eliminate u' from Eqs. (2.35) using (2.36) and obtain an ODE for S in terms of t'. We then impose S_{max} as an initial condition and solve the ODE both forward and backward from the time of peak mean speed. As Fig. 2.6 shows, results compare well with experiments without resorting to parametric fitting. In particular, they reproduce the different behaviors that Armstrong and Berg [10] reported before and after the peak, namely a rapid rise in speed, followed by more gradual deceleration. This drawn-out approach to a new drained equilibrium, which is revealed by model and experiment, gives the impression that the system reaches a residual saturation ~ 0.1 on short time scales.

From the peak speed u', we estimate the magnitude of the largest expected drop $\delta\psi_{\text{max}}$ in capillary pressure by integrating its gradient across the mesoscopic domain, $\delta\psi_{\text{max}} \sim m_c \ell_0 \mu \bar{u}(1-\nu)/K$. Using Eq. (2.36), this is, in dimensionless form, $\delta p' \sim (3/2)(1-S_{\text{max}})^{n_b+1}/[(1-S_{\text{max}})^{n_b+1} + \mu' S_{\text{max}}^{n_b+1}]$. Then, we expect capillary pressures to vary in the range $\psi_- \pm \delta\psi$ during a Haines jump. From $\gamma_{\ell g}$ of the water-decane interface [115], we find $\psi_- \pm \delta\psi \simeq 15100 \pm 1700\,\text{Pa}$, which is consistent with the pressure jump of $15790 \pm 2820\,\text{Pa}$ that Armstrong and Berg [10] calculated from observed interface radii.

2.7 Discussion

Recent experiments on a single plane layer of sintered glass beads [147] or in more complicated three-dimensional Berea sandstone [23] indicate that sudden rearrangements in liquid distribution, which we interpret as a collective first-order phase transitions, only involve a few near-neighbors, thereby confirming that the mesoscopic size should be relatively small, as Eq. (2.30) implies.

Therefore, it is questionable to integrate PDEs like Richards' Eq. (3.8) using saturation curves measured with a pressure ψ that is imposed across the distant boundaries of a macroscopic sample. One should invoke instead a function $S = f(\psi)$ that is established on a mesoscopic scale to evaluate $\partial\psi/\partial S$. A related suggestion is that, to capture a draining or a wetting front, the domain of PDE

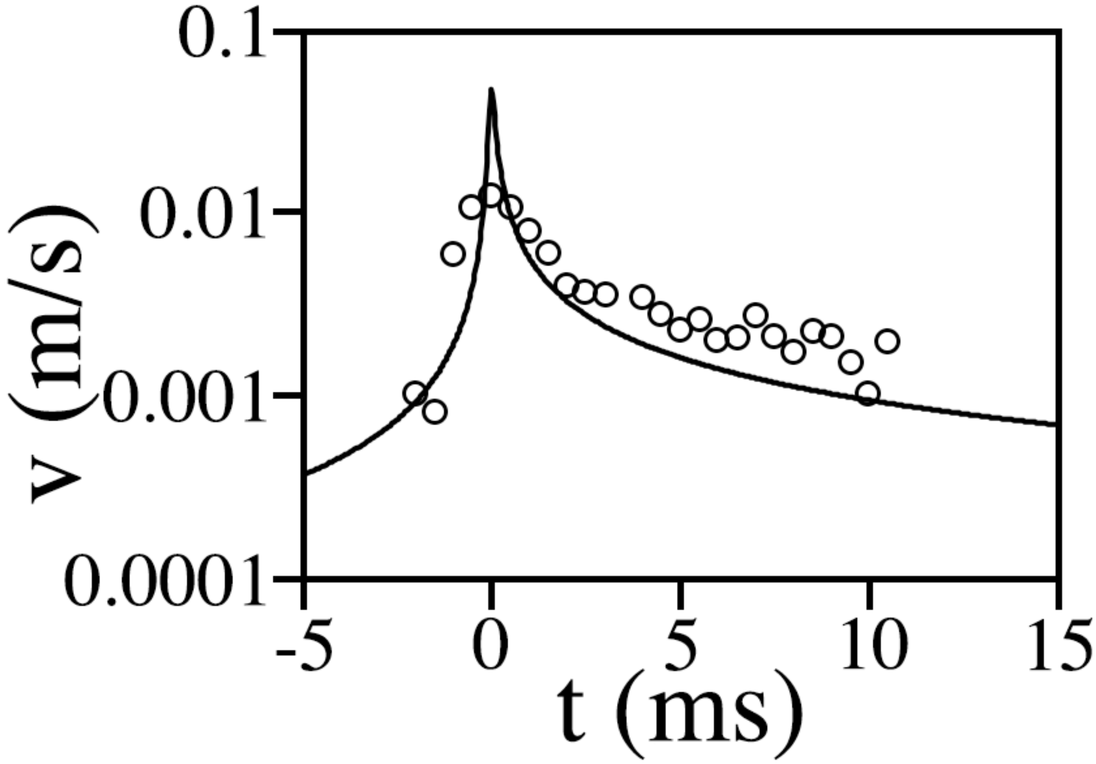

Figure 2.6: Time-history of water speed recorded by Armstrong and Berg [10] at a forced non-wetting decane fluid flow rate of $2\,\mathrm{nl/min}$ (symbols) and predicted by Eqs. (2.35)-(2.36) (line). The geometry of this experiment yields $\nu \simeq 0.349$, $\alpha_0 \simeq 12.17$, $\lambda_0 \simeq 0.567$ and $\ell_0 \simeq 26.2\,\mu\mathrm{m}$. With a periodic unit cell volume of $V_{\mathrm{cell}} \simeq 27713\,\mu\mathrm{m}^3$, its equivalent particle diameter is $d \simeq 26.4\,\mu\mathrm{m}$. Viscosities were $\mu \simeq 8.9\;10^{-4}\,\mathrm{kg/m.s}$ (water) and $\mu_d \simeq 8.4\;10^{-4}\,\mathrm{kg/m.s}$ (decane) [53] with $\gamma_{\ell g} \simeq 0.051\,\mathrm{J/m^2}$ [115]. From images in the article, we infer $\theta_c \simeq 54^\circ$ and find $|\mathbb{L}'| = \lambda \simeq 0.627$, yielding $u_0 \simeq 0.705\,\mathrm{m/s}$ and $\tau_0 \simeq 37\,\mu\mathrm{s}$. The predicted peak mean speed is $\bar{u}_{\mathrm{max}} \simeq 4.7\,\mathrm{cm/s}$.

integration should be thin. In this case, it may be judicious to treat such a front with a jump condition similar to that used in the macroscopic analysis of shock waves.

Our analysis also confirms that hysteresis is a natural behavior of a mesoscopic domain that exhibits phase transitions [168, 190], as it is in other instances where statistical mechanics is useful, such as magnetism [24], liquid sorption on microscopic surfaces [186, 121, 130, 81] or the behavior of shape-memory alloys [65]. In this view, it is not possible to eliminate hysteresis by introducing another state variable.

Our equilibrium statistical mechanics therefore predicts retention curves that are reversible until a phase transition occurs. Consequently, at the mesoscopic level, the region bound by the two curves in (ψ', S) state space cannot be invaded upon a reversal of capillary pressure. Nonetheless, practical applications invariably stage porous media that are larger than the typical correlation length mentioned earlier. For such macroscopic system, a simple example developed in Appendix A.6 shows how a porous medium with inhomogeneous saturation can produce such an invasion in (ψ', S) state space.

Because in general there is not a unique combination of saturations S_i that produces an overall saturation $\bar{S} = \sum S_i \chi_i$ in a medium composed of distinct mesoscopic domains with volume fraction χ_i, any measurement $(\psi', \bar{S})$ on a macroscopic sample that falls within the two main retention curves cannot describe the state of the system unambiguously. In other words, the existence of points within these main curves in (ψ', S) state space is a symptom of inherent inhomogeneities in a macroscopic sample, and subsequent sensitivity to past conditions. To restore unicity of the solution in a numerical scheme and reproducibility of the retention curve in experiments, one should therefore stay at the mesoscopic scale.

A related feature that our theory does not address is the percolation of negative capillary pressure through the mesoscopic domain, unless both wetting and non-wetting fluids are liquid. In the pendular regime where narrow liquid bridges congregate across links surrounded by gas on both sides, saturation can fall below the percolation threshold, thus producing the residual volume fraction θ_r observed in experiments [11]. Below this threshold, pendular bridges do not disappear until evaporation takes place.

For our description to hold, any liquid must therefore be continuously connected to domain boundaries where ψ is applied, so the latter may contribute uniformly to cavity energy through Eq. (2.2). Nonetheless, with input from percolation theory [128, 129, 42, 221, 64, 82], one might refine the statistical mechanics by cancelling the volume work in liquid-filled cavities that are entirely surrounded by a gas. A more accurate mean-field theory could also be constructed with unit cells containing more than one cavity, as suggested in Appendix A.2.

In general, because cavity energy in Eqs. (2.2)-(2.5) ignores pendular bridges forming around links at low saturation, we do not expect our mean-field theory to capture the transition from dry to wet as quantitatively as its converse from wet to dry, unless the predicted saturation S_+ at ψ'_+ is high enough to uphold the form of Eq. 2.5. Nonetheless, morphological observations on spherical packings at the pore scale [185] indicate that liquid arranges in cavity-filling clusters at a saturation as low as 0.15, followed by a percolation threshold for long-range connectivity of capillary pressure around $S \simeq 0.2$.

Finally, our analysis has restricted attention to immutable geometries in which mechanical forces do not contribute to the system's energy. However, pressure forces exerted on the porous medium could produce microscopic rearrangements, for example in unsaturated soils [83, 188]. In this case, the statistical mechanics could be refined to incorporate mechanical energy. Irreversible changes to the geometry could then lead to a mechanism for invasion of the main retention curves that is absent in our mesoscopic treatment.

2.8 Conclusions

We presented an equilibrium statistical mechanics of porous media near saturation. To avoid complicated derivations, we used a mean-field theory based on the simplest assumption that the porous structure is made up of cavities connected to their neighbors through narrow links, and that cavities are either full of a wetting fluid or empty. We derived the energy of an individual cavity in terms of its filling state and the corresponding average in the surrounding porous sample. The form of the cavity energy E suggested how capillary pressure ψ could be made dimensionless as $\psi' = \psi\bar{\ell}_0/\gamma_{\ell g}$ with mean cavity size $\bar{\ell}_0$ and liquid-gas surface energy $\gamma_{\ell g}$. The large magnitude of β' suggested why the retention curve plotting S vs ψ' is insensitive to temperature.

With simple examples, we showed that a mesoscopic sample with initially high homogeneous saturation S is eventually subject to an abrupt collective first-order phase transition as the applied capillary pressure ψ rises. We suggested that this phenomenon is related to Haines jumps. We then attributed hysteresis of the retention curve to the other phase transition that the sample experiences as capillary pressure is subsequently reduced.

We identified the origin and strength of the hysteresis in terms of statistical moments of the porous geometry, namely the dimensionless ratio α of wetted cavity area and cavity volume, and the dimensionless ratio λ of link interfacial area and cavity volume. Having showed how these two parameters could be evaluated in spherical packings, we found that the retention curve is shifted to higher capillary pressures as $\bar{\alpha}$ grows, and that its hysteresis loop gets wider as $\bar{\lambda}$ rises, or as the hydrophilic contact angle decreases. However, we showed that the hysteresis becomes less pronounced if the distribution of λ and α widens. We argued that, like other mesoscopic systems undergoing phase transitions, hysteresis is inevitable, but can be small with sufficiently broad distributions of λ and/or α.

Turning to the limits of the theory, we estimated how large the mesoscopic domain could be until gradients may no longer be ignored. Having noted that a porous domain with statistically homogeneous geometry and saturation could not reach a state (ψ', S) located in the region between the main wetting and draining retention curves, we interpreted an invasion of this region as a symptom of macroscopic inhomogeneities. With a simple counter-example, we confirmed that such a state is neither unique nor reproducible, but that it inherently depends on past history of the macroscopic sample. Accordingly, we suggested that any retention curve measured by imposing capillary pressure on a distant boundary should be treated with caution, and that an integration of PDEs like Richards' Eq. (3.8) should involve a derivative $\partial\psi/\partial S$ that is obtained from a mesoscopic saturation curve.

Finally, while recognizing that viscous forces are unlikely to remain negligible during rapid phase transitions, which we identified as the origin of Haines jumps, we suggested that the capillary number should be small enough during the more gradual liquid rearrangements leading to the transition, therefore upholding the notion of a hysteretic equilibrium retention curve.

CHAPTER 3

TEMPERATURE AND HUMIDITY WITHIN A MOBILE BARCHAN SAND DUNE

3.1 Introduction

Moderate temperatures and sufficient humidity are essential geophysical prerequisites for microscopic life in hyper-arid habitats. For example, moisture controls the physiological activity of nitrogen and carbon fixation in biological soil crusts (BSC), which contain a mixture of cyanobacteria, lichens, mosses, fungi and algae. BSCs are common on hard desert floors and play an important role in the ecosystem dynamics of drylands [28]. Conversely, once formed, BSCs affect hydrology, including infiltration and runoff, albeit in ways that remain poorly understood [21].

Surface moisture also affects aeolian processes, which govern the shape, speed and direction of mobile dunes [228, 229]. For instance, in spite of arid conditions, droplets condense at dawn when the surface temperature descends below the dew point [120], forming ephemeral liquid bridges among grains once water penetrates the sand bed [75]. Small amounts of liquid as low as 0.05% by mass can then increase grain cohesion [143, 206, 146], impeding aeolian erosion [173], but temporarily stiffening the sand surface, thus enhancing transport [105, 181].

Another example where moisture, life and geophysics are intertwined is in the rhizosphere of desert plants. Where such plants grow, arbuscular mycorrhizae fungi enhance the acquisition of water and nutrients by the roots of the plant host, thus ensuring its survival and faciliting soil fixation [201, 174, 208].

Recently, Gommeaux et al. [84] and Heulin et al. [102, 103] showed that BSCs and plant rhizospheres are not alone in harboring desert microbes. They found that stationary, non-vegetated desert sand dunes in South-East Morocco contained approximately a thousand culturable microbes for every gram of sand. These surprising observations prompted questions about the internal temperature and moisture that would allow these microorganisms to exist. If such favorable internal habitats could last long enough, the observations of Gommeaux et al. [84] also raised the intriguing possibility that relatively rapid mobile desert dunes could also contain live microbes, even though the collective motion of their sands does not normally permit the establishment of BSCs or plants [66], and relentless aeolian surface renewal works against the preservation of their moisture.

In fact, as this chapter will show, microorganisms are found below the surface of crescent-shaped barchan dunes, even though the latter can turn over their entire sand mass much more rapidly than the dune studied by Gommeaux et al. [84]. This presence was unexpected, since microbial viability is ultimately tied to sufficient sand moisture and moderate heat, whereas harsh atmospheric conditions, solar radiation, aeolian erosion of the windward slope, redeposition of dry sands on the leeward avalanche face, and rare precipitation all conspire against favorable humidity and temperature. Until this work it was unclear how microbes could find suitable habitat in relatively fast-moving hyper-arid dunes.

While much attention has been paid to the aeolian transport that forms desert dunes [134], fewer studies have focused upon their interior, and none have recorded the moisture and temperature habitat deep below the surface. To our knowledge, there is no prior attempt to model or simulate the internal heat and mass transfer within a mobile object of such size. In addition, because the travelling velocity of a mobile dune is typically on the same order as the thermal diffusion speed through sand, it was hitherto unclear how this motion affects the internal temperature of the dune.

Nonetheless, understanding the deep habitat of mobile dunes is crucial to ensure the success of stabilization strategies. The relentless encroachment of mobile dunes on infrastructure has prompted efforts to fix them through land use restrictions [133], artificial fixing by wind barriers or checkerboards [66], and restoration of disturbed BSCs [30]. Natural dune stabilization also involves other factors, including the release and oxidation of iron from primary minerals, known as rubification [22], and the development of physical soils crusts by deposition of wind-borne salts, silts and clays [66]. In marine dunes, Forster [70] found that microbes play an important stabilizing role, even before BSCs form. In such landforms, more frequently battered by rain than their desert counterparts, she observed how bacteria aggregate sand by secreting extracellular polysaccharides (EPS) [107, 108]. The resulting sand cohesion thus reduces wind erosion and increases moisture and nutrient content [71].

In general, stabilization of a mobile sand dune requires an ecological synergy between geophysics, meteorology, plant biology, zoology, and microbiology. Although the complex feedback underlying this synergy remains misunderstood, it depends crucially upon heat and moisture. If desert sand dunes travel too fast for plants to take root, or if moisture becomes depleted by extended drought, the stabilization process breaks down [52, 224]. It might recover with favorable moisture and temperature, through competing mechanisms involving heat transfer, penetration of scarce rainwater and ambient water vapor, aeolian transport in the turbulent boundary layer, granular cohesion and friction, and granular flow on leeward faces.

In short, heat and moisture are important geophysical attributes of mobile sand dunes. Focusing attention on these parameters, we show that barchans conceal regions of moderate temperature and sufficient humidity to permit the survival of microbes. Despite their mobility, barchan dunes preserve moisture acquired during infrequent rains. As they progress downwind, humidity adsorbed on sand grains immobilized under the leeward slope resurface at their toe, thus compensating for moisture lost to windward aeolian erosion.

To expose such internal heat and moisture processes, we sunk probes with data storing and broadcasting capabilities through the avalanche slope of a barchan in Qatar. These instruments remained buried where they were trapped while the dune passed overhead, until they finally emerged windward several months later. To gauge how deeply dune sands could protect microbes from extreme environmental conditions, we also contrasted these observations with vertical temperature and humidity profiles acquired just below the surface. These profiles revealed that wide diurnal variations in solar radiation and atmospheric conditions only affect temperature and moisture to a relatively shallow depth, thus allowing the dune to shelter milder conditions in its midst on longer time scales. They also suggested that surface humidity at dawn can temporarily affect aeolian transport and sand cohesion.

We begin with a geophysical description of mobile barchan dunes. We then present and interpret measurements of temperature and humidity just below the surface. We contrast these measurements with those of deeply buried probes, and show that moisture adsorbed on sand grains can persist within the mobile dune for a long time. Finally, we present respiration data and microscopic observations as evidence of biological activity.

3.2 Mobile barchan dunes

Mobile dunes pose insidious threats to human infrastructure. Their relatively slow but relentless wind-driven advance rarely brings them to the attention of civil or industrial planners. Attempts to stop them by planting *Prosopis* trees or erecting simple barriers are often unsuccessful [200]. In general, wind-driven granular transport determines the morphology and shape of hyper-arid deserts [14, 144, 228, 229]. On the edge of a sand sea, barchan dunes like the one we studied (Fig. 3.1) form where an inexhaustible sand supply meets a flat plain subject to a prevailing wind direction [134]. Their crescent-shape makes it possible to model the surrounding flow [189] and to understand their behavior [172, 183, 8, 101, 4].

The gently-rising windward face of a barchan is interrupted by a brink behind which air recirculates downward and inward. In its wake, suspended sand loses momentum and accumulates onto the steep leeward slope. Intermittent avalanches maintain this slope at its angle of repose by rapidly transferring excess grains downward. Sand involved in avalanches is trapped unless wind changes direction. Barchan dunes are thus mobile (Fig. 3.2), with speed roughly in inverse proportion to their size [43]. The lee face of the barchan dune is terminated by horns revealing the formation of “wing vortices” on either side and

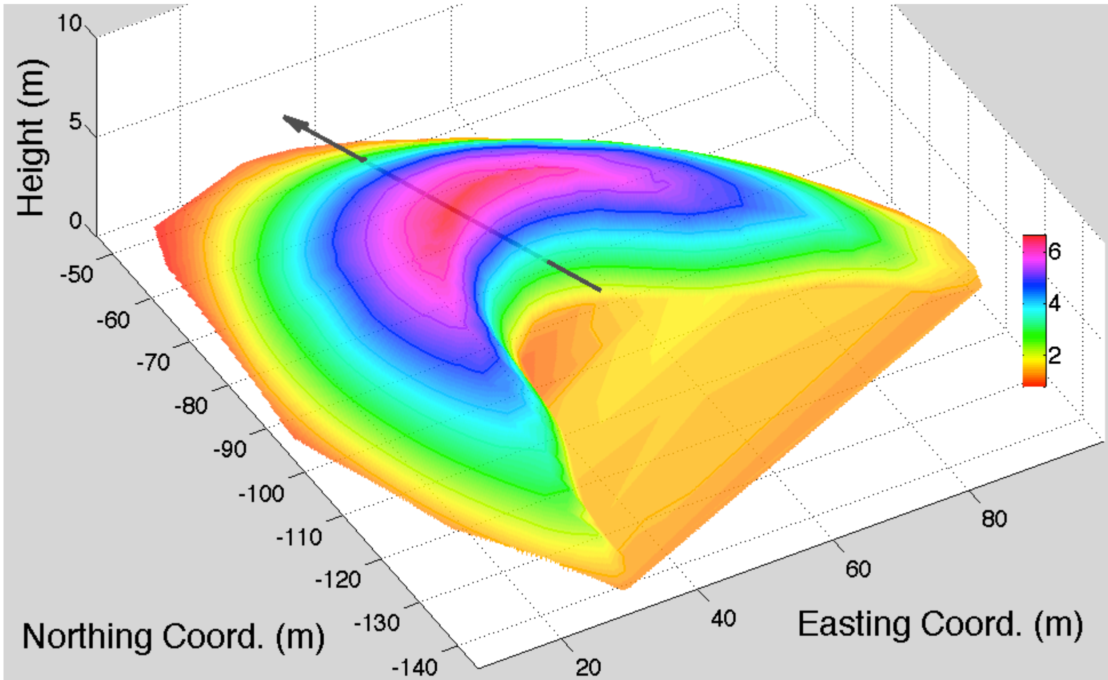

Figure 3.1: Shape of the Qatar dune under study on July 16, 2012. Easting, northing and altitude refer to the datum on hard ground at $25°00'35.82''$N, $51°20'24.54''$E near the weather station. The arrow is the estimated path relative to the dune of probe 1, which disappeared below the surface on May 1, 2011. The leeward avalanche face is inclined at $31\,°$ and the dune moves on an average bearing of $159\,°$. Altitude is represented by the color scale shown and is exaggerated by a factor of $\simeq 3$.

giving the dune its crescent shape. Sand escaping to the next barchan originates from these horns [100].

The barchan under study is outlined in Fig. 3.1. It is part of a mobile dune field West of Mesaieed (Qatar) with speeds shown in Fig. 3.2 and an average bearing of $160\,°$. In Appendix B.5, we report positions of selected nearby dunes, as well as properties of their sands. Sand material density is $\rho_m \simeq 2630\,\mathrm{kg/m^3}$. Particle size distribution (PSD) varies within the dune. On the windward slope, its moments are $\bar{d} \simeq 351\,\mu\mathrm{m}$, $d_{20} \equiv (\overline{d^2})^{1/2} \simeq 365\,\mu\mathrm{m}$, and $d_{30} \equiv (\overline{d^3})^{1/3} \simeq 377\,\mu\mathrm{m}$, where the overbar denotes averaging over the PSD. Particles collected at the base of the leeward face are typically larger ($\bar{d} \simeq 346\,\mu\mathrm{m}$) than at the top

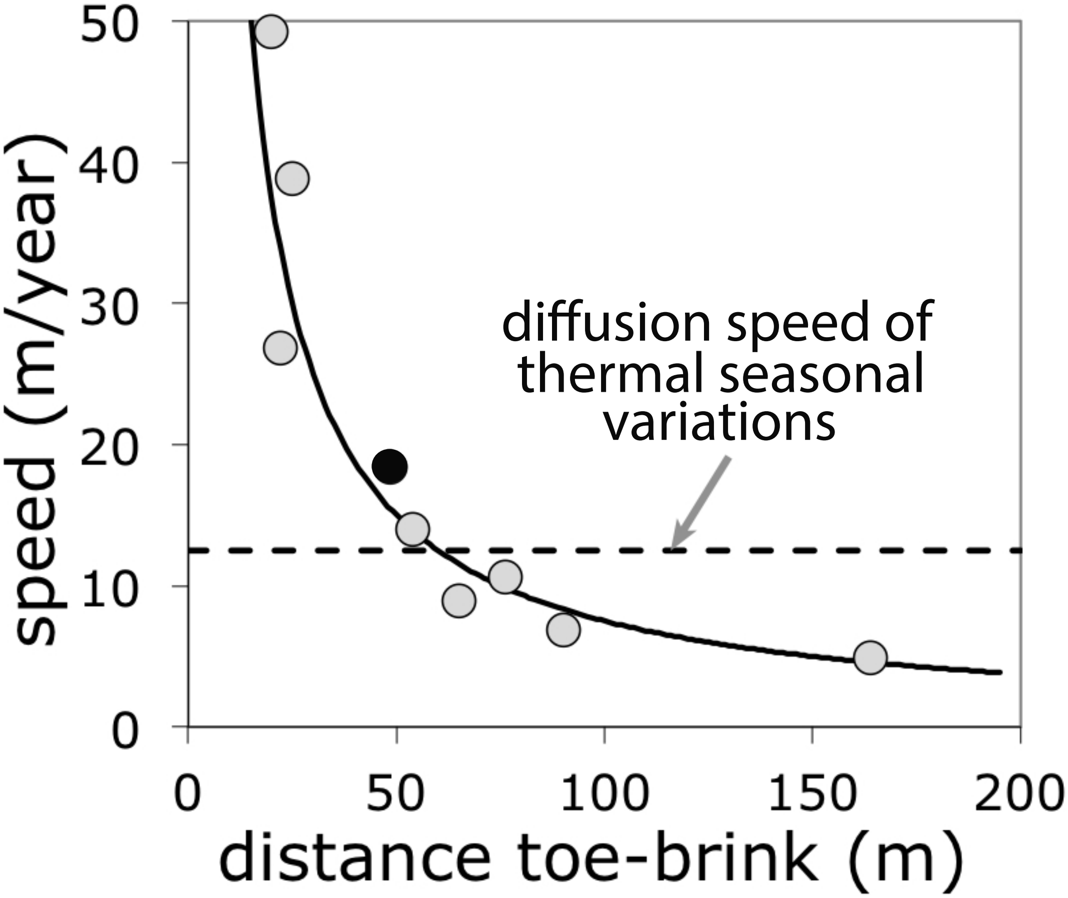

Figure 3.2: Dune speed U (m/yr) versus distance D (m) from windward toe to brink on the vertical plane of dune symmetry, derived from online historical images of GoogleEarth from October 2002 to September 2009 for the Qatar dune field studied (dune positions in Table B.2 of Appendix B.5). The line is the best fit $UD \simeq 750\,\mathrm{m}^2/\mathrm{yr}$. The horizontal dashed line marks the diffusion speed $u_d = 2\sqrt{\alpha_s \pi / Y}$ of thermal seasonal variations on a time scale Y of a year. The filled circle represents the barchan under study.

($\bar{d} \simeq 319\,\mu\mathrm{m}$), reflecting particle segregation in naturally intermittent granular avalanches [89]. Such dense slides give rise to an inclined stratification featuring layers of larger particles ($\bar{d} \simeq 352\,\mu\mathrm{m}$, $d_{20} \simeq 365\,\mu\mathrm{m}$, and $d_{30} \simeq 376\,\mu\mathrm{m}$) interlaced with layers of smaller ones ($\bar{d} \simeq 312\,\mu\mathrm{m}$, $d_{20} \simeq 331\,\mu\mathrm{m}$, and $d_{30} \simeq 347\,\mu\mathrm{m}$). The pattern is buried as the dune moves forward, progressively reappearing on the upwind slope below the brink's elevation as rounded outlines of the old face.

Until the observations of Gommeaux et al. [84], it was unclear whether microbes could survive extreme conditions of a hyper-arid, non-vegetated desert dune, as they do within biological soil crusts [21] or the rhizosphere of desert plants [174]. Intuition suggested that relatively fast-moving mobile dunes would be less likely to shelter internal microbial activity. Informing this question required peering deep into the dune.

Unfortunately, studies of the interior of sand dunes are rare. To investigate internal dune stratigraphy, McKee et al. [144] performed deep excavations and Bristow et al. [31] used ground-penetrating-radar. Recently, Vriend et al. [219] used this technique to visualize cross-strata in large dunes, and Vriend et al. [218] investigated the acoustics of booming sands with seismic refraction. To elucidate the behavior of the "dry layer" near the surface of a desert dune, Kobayashi et al. [124, 125] measured temperature and humidity in the first $13\,\mathrm{cm}$ below the dune surface. During campaigns in the Negev desert, Katata et al. [118] recorded incident radiation, derived latent heat flux from microlysimeter measurements below the dune surface, sand water content by gravimetric sampling, and turbulent transport flux of sensible heat with a sonic anemometer. de Félice [50] recorded temperatures of the surface, at depths of 5 and $20\,\mathrm{cm}$, and of ambient air $5\,\mathrm{cm}$ above. He also evaluated radiation fluxes at short and long wavelengths, which he reported for one hour following solar noon. He then calculated a thermal diffusivity $\alpha_s \simeq 1.5\ 10^{-7}\,\mathrm{m}^2/\mathrm{s}$ for sand at his test site. Chen [44] measured similar thermal conductivities for four quartz sands at various compactions and water volume fractions.

As Carslaw and Jaeger [38] showed, thermal diffusion penetrates the interior of a dune at a speed $u_d \equiv 2\sqrt{\alpha_s \pi/\tau}$, which is set by the period τ of thermal forcing at the surface. Therefore, over a year with $\tau = 365$ days, seasonal variations penetrate into our dry sands at a rate $u_d \simeq 12\,\mathrm{m/yr}$. As Fig. 3.2 shows, because the mean dune speed U is comparable to u_d, the motion of the dune crucially affects its deep thermal response to seasonal variations. In contrast, thermal variations on the shorter diurnal time scale $\tau = 24\,\mathrm{hrs}$ only penetrate a relatively shallow region below the surface. Because the corresponding diffusion speed $\simeq 240\,\mathrm{m/yr}$ far exceeds U, dune motion hardly matters to the diurnal thermal problem.

In short, although prior work focused on diurnal thermal variations just below desert surfaces, little was known whether near-surface conditions allow microbial activity. Although dunes revealed a rich internal stratigraphy, the distribution of heat and moisture deep within fast-moving mobile dunes remained similarly unclear. To inform these questions, section 3.3 addresses conditions near the dune surface. Section 3.4 then considers heat and moisture deep within a mobile dune.

3.3 Near-surface diurnal variations

This section focuses upon diurnal variations of temperature and humidity just beneath the windward slope of the dune, towards establishing where microbes could be sheltered from hyper-arid ambient conditions. To that end, we report data from two separate invasive probes recording temperature and adsorbed moisture. Unlike semi-arid conditions investigated by Katata et al. [118], our dune is drier, so that evaporation plays a minor role in the heat balance. We show that a thermal model incorporating wind-driven thermal convection and net radiation flux can capture temperature variations near the surface. Modern data acquisition allows us to report data in greater detail than de Félice [50] and Kobayashi et al. [124, 125], and to produce a simultaneous animation of temperature depth profile, surface heat fluxes and wind speed. By measuring thermal diffusivity of our sands in situ, these near-surface observations set the stage for deeper and longer measurements of temperature and humidity with the buried probes discussed in section 3.4.

3.3.1 Instruments

On March 19, 2011, we deployed the two instruments on the windward toe of the mobile barchan sand dune in Fig. 3.1 at $25°00'34.7''$N, $51°20'24.9''$E. The temperature probe consisted of a $305\,\mathrm{mm}$-long glass-filled Delrin lance of $41\,\mathrm{mm}$ width and $11\,\mathrm{mm}$ thickness, with a $10\,°$ taper to facilitate insertion into dune sands (Fig. 3.3). Its long flat face was hollowed to lodge a Plexiglas housing of $227\,\mathrm{mm} \times 24\,\mathrm{mm} \times 9\,\mathrm{mm}$ protecting fifteen LM235 National Semiconductor temperature sensors and their associated wires and resistors, all bound by epoxy resin into the assembly. Housing material and bonding were chosen to match the thermal diffusivity of bulk sand, in an effort to minimize thermal disruption by the probe.

The robust temperature sensors were packaged in a small cylindrical capsule of $4.8\,\mathrm{mm}$ diameter that determines their vertical spatial resolution. They operated as two-terminal Zener diodes with breakdown voltage proportional to absolute temperature. We supplied their cathode with $\sim 10\,\mathrm{V}$ through a $12\,\mathrm{k\Omega}$ resistor, connected anode to ground, and recorded the breakdown voltage from

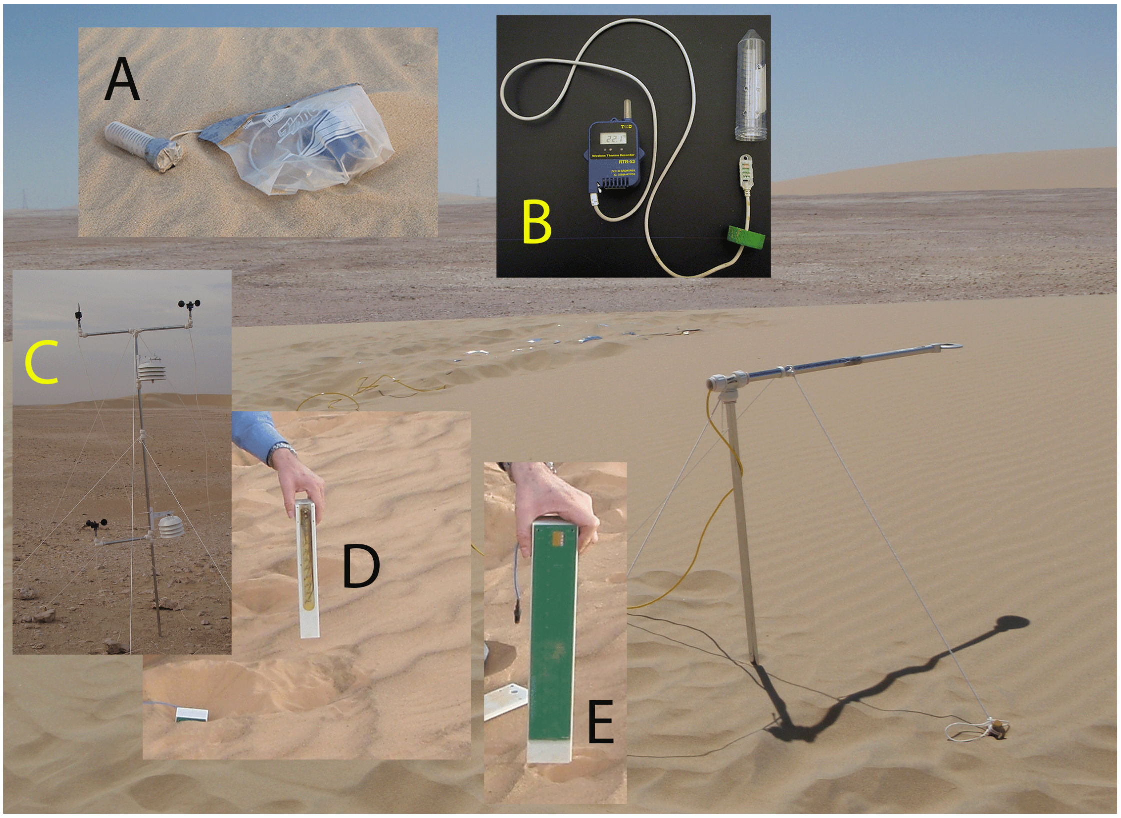

Figure 3.3: Instruments deployed. Background: radiometer at the tip of a Γ-shaped rod on the Qatar dune. (A) The probe described in section 3.4 resurfaces in July 2012. (B) Probe assembly: remotely-controlled logger unit connected to the temperature/humidity sensor protected in a conical with ventilation holes. (C) Temporary weather station with two RH and T instruments, two anemometers, and a wind vane. (D) 15-sensor temperature probe and (E) capacitance probe about to be inserted through the dune surface.

cathode to ground. Although these sensors were meant to output $10\,\mathrm{mV}/°\mathrm{K}$, we calibrated each of them in the laboratory against a known ambient temperature. Once buried in sand, the sensors provided temperature at fifteen independent depths x in the range $5 \leqslant x \leqslant 218\,\mathrm{mm}$ from the free surface.

We recorded the net radiation flux with a Kipp & Zonen "NR Lite 2" radiometer at $80\,\mathrm{cm}$ above the dune near the location where the temperature probe was buried. This robust instrument, shaped as a disk of $80\,\mathrm{mm}$ diameter, possessed a single component sensor that recorded the difference in a wide spectrum of wavelengths $0.2 < \lambda < 100\,\mu\mathrm{m}$ between the net flux received from below (sand albedo and emission) on a circular absorbing patch of $34\,\mathrm{mm}$ diameter and the corresponding flux striking a similar patch from above (solar flux and atmospheric emission). Because the calibrated instrument sensitivity was relatively low ($12.5\;10^{-6}\,\mathrm{Vm^2/W}$), we boosted the output voltage with an amplifier of 100 gain before data acquisition.

Signals from the temperature, moisture and radiometer signals were multiplexed to a National Instrument cRIO data acquisition chassis with a Real-Time micro-computer controlling the data stream to and from a field-programmable-gate-array. When powered with long-term Lithium-Polymer batteries (or with lead-acid batteries recharged by a 100W solar panel), the chassis was autonomous, selecting each channel in turn for measurement. We buried it away from the probe location under a reflective "survival blanket" to avoid extreme conditions that might damage its electronics.

Meanwhile, we erected a weather station on hard ground approximately $28\,\mathrm{m}$ upwind of the dune. It measured wind speed at elevations of $z_1 \simeq 0.9\,\mathrm{m}$ and $z_2 \simeq 2.4\,\mathrm{m}$ using two SecondWind "C-3" three-cup magnetic-induction anemometers producing an output frequency linear upon wind speed u, with detection threshold $\simeq 0.35\,\mathrm{m/s}$. We also recorded wind direction at $2.4\,\mathrm{m}$ with a NRG #200P potentiometer wind vane, as well as ambient temperature T_z at $z \simeq 0.9\,\mathrm{m}$ and $\simeq 2\,\mathrm{m}$ using two ThermoWorks TW-USB-2-LCD+ autonomous loggers with accuracy $T_z = \pm 0.3\,^\circ\mathrm{C}$, protected from direct and reflected solar radiation by open white plastic shields. A SecondWind "Nomad" data logger acquired wind speed, direction and temperature. All variables were recorded at $1\,\mathrm{min}$ intervals.

3.3.2 Moisture

To record moisture profiles near the surface (Fig. 3.4), we also deployed a probe similar to the one that Louge et al. [136] used on a Mauritanian sand dune, but possessing 15 sensors with spatial resolution of $\sim 3\,\mathrm{mm}$ in the vertical direction. Those authors provided an exhaustive description of the instrument. Its electronics produce a "loss tangent" $|\tan\varphi|$ that is correlated with the relative humidity in equilibrium with the surrounding sand grains. To find the correlation, we exposed samples of Qatar dune sand to a climate-controlled chamber at relative humidities in the range $0.30 < \mathrm{RH} < 0.82$ at $35\,^\circ\mathrm{C}$. (The highest RH is the upper stability limit of the electronics for this sand). We found

$$|\tan\varphi| \simeq |\tan\varphi_0|[\exp(\mathrm{RH}/\mathrm{RH}_0) - 1], \tag{3.1}$$

where $\varphi_0 = 0.0241 \pm 0.0045$ rad and $\mathrm{RH}_0 = 0.233 \pm 0.013$. Using the same chamber operated at $0.3 < \mathrm{RH} < 0.9$ with temperatures of 22 and $40\,^\circ\mathrm{C}$, we also related RH to the local fraction Ω of water mass adsorbed on sand grains relative to total sand mass by comparing weights of dry and moist samples. At our relatively low moisture levels, we followed Shahraeeni and Or [191] in assuming that water storage was dominated by film adsorption on a thickness

$$\ell_w = \left[\frac{M_w A}{6\pi\rho_w \hat{R} T \ln(\mathrm{RH})}\right]^{1/3}, \tag{3.2}$$

where M_w is the molecular weight of water, ρ_w is its liquid density, $A < 0$ is Hamaker's constant, and $\hat{R}$ is the fundamental gas constant [113]. This relation implies the following dependence of relative humidity and mass fraction:

$$\mathrm{RH} = \exp[-(\Omega_\ell/\Omega)^3]. \tag{3.3}$$

As inset B in Fig. 3.4 shows, data at relatively low moisture levels conformed to Eq. (3.3) despite limited hysteretic behavior between water adsorption and desorption at $22\,^{\circ}\mathrm{C}$ similar to what Shang et al. [193] observed.

Figure 3.4 shows two profiles of relative humidity recorded on March 20, 2011 through a depth of $30.5\,\mathrm{cm}$. At sunrise, dew briefly collected on the surface, raising the relative humidity to 60% there. Such level likely affected the erosion behavior of the sand surface, at least temporarily. For instance, Fraysse et al. [77] observed rising values of the maximum angle of stability for a granular pile with RH $\gtrsim 0.4$. Similarly, Ravi et al. [173] reported from wind tunnel tests that the aeolian shear velocity threshold undergoes a transition within $0.4 \lesssim$ RH $\lesssim 0.65$. As the sun later reached solar noon, humidity nearly vanished at the surface, thus exposing the latter to unbridled aeolian erosion.

Crucially, diurnal ambient humidity variations only affected the first $5\,\mathrm{cm}$. Relative humidity then gradually increased with depth x, reaching a nearly constant level at $x \gtrsim 20\,\mathrm{cm}$. We will discuss what this profile implies for microbiology in section 3.5.

3.3.3 Thermal model

Figure 3.5 and its animation available online show temperature profiles recorded with the 15-sensor probe in the first $22\,\mathrm{cm}$ from the surface. As de Félice [50] and Kobayashi et al. [124, 125] had already observed, harsh diurnal temperature variations were attenuated within a short distance $\sim 10\,\mathrm{cm}$ from the surface. To analyze this, we modeled sub-surface thermal conditions in response to solar radiation and to convection by surface winds. The model assumed that sand has uniform heat diffusivity $\alpha_s = k_s/(\rho_s c_s)$, conductivity k_s, bulk density ρ_s and specific heat per mass c_s. Because local moisture typi-

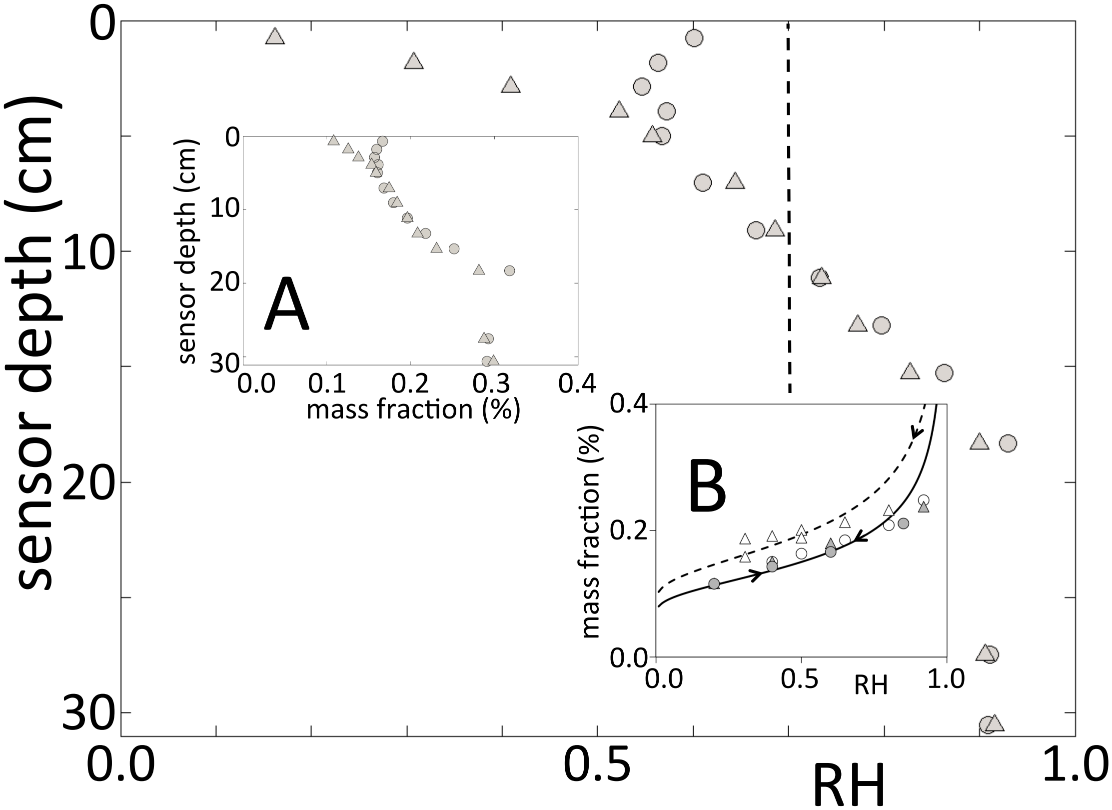

Figure 3.4: Depth profiles of relative humidity recorded at sunrise (circles) and as the sun culminated at solar noon (triangles) on March 20, 2011, inferred from Eq. (3.1) from the "loss tangent" of a 15-sensor variant of the capacitance probe of Louge et al. [136]. In this case, microbial survival was likely inhibited at depths $< 11\,\mathrm{cm}$, where RH $= a_w < 0.7$ [155] (left of vertical dashed line), but probably not below. (A) Profiles of mass fraction Ω inferred from Eq. (3.3). Diurnal moisture variations only affected the first $5\,\mathrm{cm}$, and gradually rose with depth. (B) Isotherm data (symbols), courtesy of M.-Jocelyn Comte, Xavier Lapert, Floran Pierre, and Patrick Perré, and their corresponding fits to Eq. (3.3) (lines). In this inset, circles and triangles denote, respectively, the adsorption isotherm at increasing RH, and its desorption counterpart at decreasing RH. At $40°$C (filled symbols), the two isotherms nearly coincide and are fitted to $\Omega_\ell \simeq 0.0013$ (solid line). As expected from the relative insensitivity of ℓ_w on T in Eq. (3.2), the adsorption isotherm at $22°$C (open circles) conforms to the same fit. However, desorption at $22°$C (open triangles) lies above adsorption (open circles) and is fitted to $\Omega_\ell \simeq 0.0017$ (dashed line). In inset A, mass fraction Ω was converted to water activity with $\Omega_\ell \simeq 0.0015$ intermediate between the two values of Ω_ℓ.

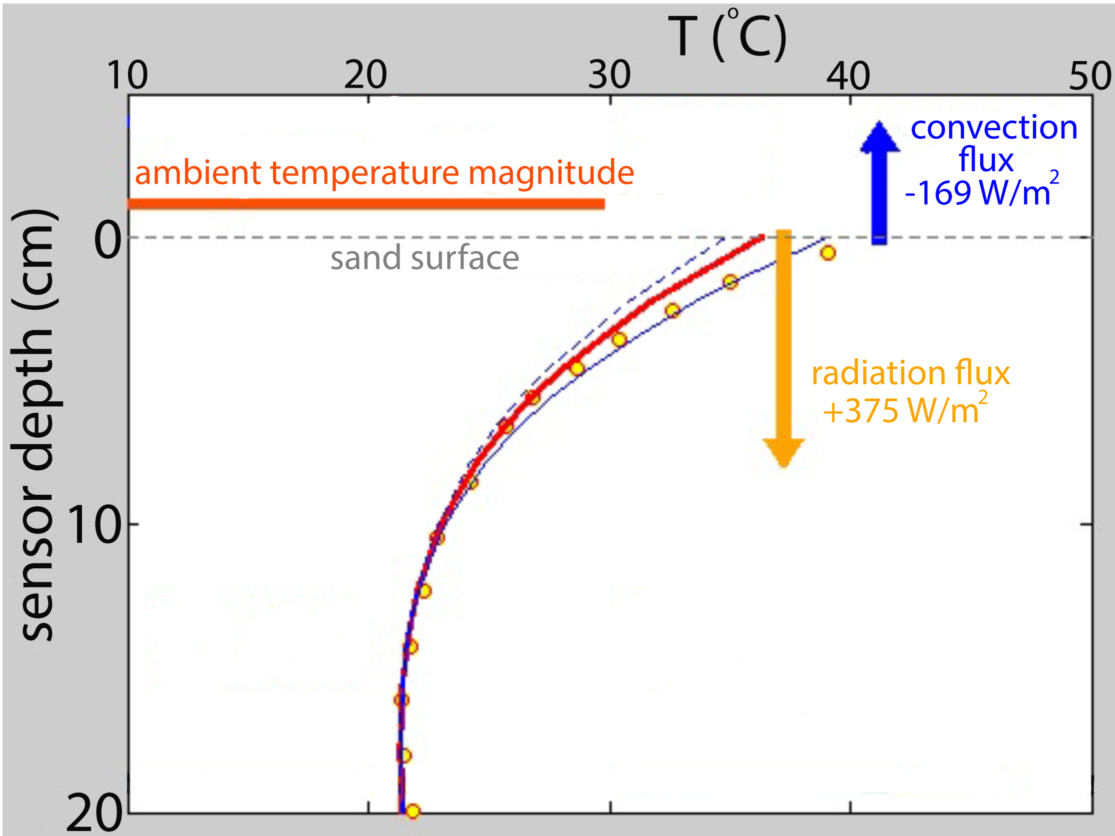

Figure 3.5: Typical temperature profile snapshot through the first $20\,\mathrm{cm}$ below the sand surface (horizontal dashed line) recorded at 11:09 am Qatar time(UT+$3\,\mathrm{hr}$) on March 21, 2011 with an instantaneous wind speed of $4.5\,\mathrm{m/s}$. The ordinate is depth in cm, and the abscissa is temperature in °C. The thick horizontal orange line shows ambient temperature T_z on that scale recorded at $z = z_T = 2\,\mathrm{m}$. Circles represent measurements, with symbol size equal to actual sensor diameter. The thick red line is the prediction of the thermal model with $\zeta \equiv u^*/u = 0.084$, $k_s = 0.49\,\mathrm{W/m.°K}$, $\rho c_p = 1170\,\mathrm{J/m^3.°K}$, $\alpha_s = 3.9\ 10^{-7}\,\mathrm{m^2/s}$, $\epsilon_a = 0.7$, $\epsilon = 0.86$, $\omega = 0.64$ and the depth boundary condition $T_s \to 295\,°\mathrm{K}$ as $x \to \infty$. The dashed and solid blue lines are, respectively, $\zeta = 0.084 + 0.059$ and $0.084 - 0.059$ corresponding to its range of uncertainty. The left and right vertical arrows indicate measured net radiation and calculated thermal convection fluxes, respectively, counted positive into the dune. An animation of this Fig. from March 19 to 21, 2011 is available in the supplementary information of Louge et al. [139].

cally represents $< 0.3\%$ of total sand mass anywhere near the surface, the model ignored latent heat release, or variations of k_s with water content [44]. It also neglected radiative transfer within the porous sand which, according to the analysis of Taine et al. [204], produces an effective radiation conductivity $< 2\ 10^{-3} k_s$. The conservation Eq. for sensible heat is then

$$\frac{\partial T_s}{\partial t} = \alpha_s \frac{\partial^2 T_s}{\partial x^2}, \tag{3.4}$$

where T_s is sand temperature in equilibrium with its surroundings, and x is the downward vertical along the probe. At the free surface, continuity of the thermal flux imposes the boundary condition

$$-k_s \frac{\partial T_s}{\partial x} = \dot{q}''_{\text{rad}} + \dot{q}''_{\text{wind}}, \tag{3.5}$$

where $\dot{q}''_{\text{rad}}$ and $\dot{q}''_{\text{wind}}$ are, respectively, the net radiation and turbulent thermal fluxes received by the dune (positive downward).

Appendices B.1 ("Radiation model") and B.2 ("Thermal boundary layer") provide detailed calculations of these fluxes, so Eq. (3.4) may be solved numerically. However, it is instructive to recall first the simpler solution of a harmonic forcing of the surface temperature [38], which captures well the increasing time lag $x\sqrt{J/(4\pi\alpha_s)}$ of the peak temperature at depth x,

$$T_s = \bar{T}_{s_0} + \Delta T_s \exp\left[-x\sqrt{\frac{\pi}{\alpha_s J}}\right] \sin\left[\frac{2\pi}{J}\left(t - \frac{J}{4}\right) - x\sqrt{\frac{\pi}{\alpha_s J}}\right], \tag{3.6}$$

where J is the diurnal period ($24\,\text{hr}$), $\bar{T}_{s_0}$ is the corresponding mean surface temperature, ΔT_s is total diurnal temperature excursion at the surface, and t is time from midnight, roughly halfway between sunset and sunrise. Following de Félice [50], we used Eq. (3.6) to infer a bulk thermal diffusivity $\alpha_s \simeq 3.9\ 10^{-7}\,\text{m}^2/\text{s}$ for our sands from records of temperature peak time versus depth. Equation (3.6) also predicts that surface temperature variations decay exponentionally on a scale $x_J = \sqrt{\alpha_s J/\pi}$. In our experiments, $x_J \simeq 104\,\mathrm{mm}$, which justifies the design length of the temperature probe.

Because the sky was free of clouds in these experiments, we estimated broadband radiative properties of our sands from the net flux collected by the differential radiometer. At night, the instrument recorded the difference between a relatively small atmospheric emission from above and infrared emission from the sand surface. This difference was mainly a measure of sand surface emissivity. During the day, it was struck above by solar radiation and atmospheric emission, and by reflected light from the sand surface below. As outlined in Appendix B.1, knowledge of the dune surface temperature time-history and the clear-sky solar flux $\dot{q}''_{\mathrm{sun}} \simeq 1353\,\mathrm{W/m^2}$ then yielded estimates of sand albedo $\omega \simeq 0.64$ and emissivity $\epsilon \simeq 0.86$ by least-squares-fitting the net radiometer signal over the entire experiment. We then used these quantities to predict the net radiative surface flux from solar ephemeris, taking into account local dune slant. (At the probe location, the skyward unit normal $\hat{\mathbf{n}}_d$ to the dune had an angular elevation of $77\,^\circ$ and a bearing of $300\,^\circ$).

Unfortunately, Eq. (3.6) was too crude to represent temperature variations driven by the complicated diurnal thermal flux through the sand surface. Instead, as detailed in Appendix B.2, we modeled the wind-generated convective contribution to the flux by invoking the Monin-Obukhov similarity [223]. To find the overall surface flux boundary condition, we then added the net radiative flux calculated in Appendix B.1. Finally, we integrated partial differential Eq. (3.4) using the *pdepe* toolbox of Matlab, subject to $T_s = 295\,^\circ\mathrm{K}$ at the distance $x = 5x_J$ deep into the dune.

As Fig. 3.5 shows, this thermal model captures temperature data well. To illustrate its ability to do so over two diurnal periods, we also provide an animation of the temperature profile for March 19-21, 2011 in the supplementary information of Louge et al. [139]. This movie reveals that Eqs. (3.4)–(3.5) produce accurate predictions, particularly at night, when the dune surface, colder than the air aloft, created a stably-stratified atmospheric boundary layer. The stabilization started approximately an hour before sunset, as the net radiation flux turned negative. The magnitude of the dune's radiation loss then reached a maximum and slowly decreased as surface temperature cooled. The net radiation flux turned positive about an hour after sunrise, rapidly inverting the temperature gradient at the surface, and producing an unstably stratified thermal boundary layer with warmer sand than ambient air. Around solar noon, the model overestimated the calculated convective flux, yielding a surface temperature $\sim 5\,^{\circ}\mathrm{C}$ too low at that time. This discrepancy, perhaps due to our choice of parameters in the Monin-Obukhov similarity, underlines the importance of wind-driven thermal convection, which increased with wind speed, but was either directed into or out of the dune depending on the difference between ambient air and sand surface temperatures. In future experiments, one should record atmospheric profiles of fluctuating wind speed and temperature, so accuracy of the Monin-Obukhov similarity could be refined in this arid situation.

Finally, it is interesting to note that, according to our calculations, the dune hardly experienced any heat gain or loss over the $24\,\mathrm{hr}$ period from the first sunrise to the next. During that time, the integrated net radiation input was $+4.62\ 10^6\ \mathrm{J/m^2}$, while the integrated convective loss was $-4.77\ 10^6\ \mathrm{J/m^2}$, which represented a net loss of $< 3\%$ of the radiation input. Therefore, this patch of dune was nearly in thermal equilibrium with its ambient surroundings over the duration of this experiment in mid-March. In particular, the recorded mean diurnal ambient temperature was $22.4\,^{\circ}\mathrm{C}$, an almost identical value to our predicted mean surface temperature of $23.0\,^{\circ}\mathrm{C}$. (Meanwhile, the recorded excursion in ambient temperature was $14.1 < T_z < 31.6\,^{\circ}\mathrm{C}$, and our prediction of surface temperature spanned $13.2 < T_{s_0} < 35.8\,^{\circ}\mathrm{C}$). However, as the next section suggests, such equilibrium of the surface flux does not persist over the whole year and/or on the entire dune.

3.4 Deeply self-buried probes

In this section, we report signals from self-buried probes confirming that temperature and humidity deep within the dune are unaffected by ambient diurnal variations. We show that, although deep temperature can be accurately inferred from solar ephemeris and statistics on wind strength, deep humidity is more unpredictable, as it is sensitive to the random timing of rainfall, subsequent non-linear water penetration, and dune motion.

3.4.1 Instruments

As Fig. 3.2 illustrated, the Qatar dunes establish an average forward speed that is inversely proportional to their length between toe and brink. We exploited this motion to investigate conditions deep beneath the surface by sinking two identical ThermoWorks TR-3310 temperature and humidity probes through the leeward avalanche face, waiting for the dune to overcome them. These instruments measured relative humidity RH $\pm\ 2\%$ in the range $5\% < \text{RH} < 95\%$ and temperature $T_s \pm 0.3\,^\circ\text{C}$ in $0 < T_s < 55\,^\circ\text{C}$. Each probe was attached to a RTR-53 recording unit that included a two-year battery, an antenna that allowed hand-held electronics to interrogate it remotely, and enough memory to record autonomously for 333 days. We protected them in a plastic container featuring several holes allowing humidity to pass, while securing them against small animals burrowing through the avalanche face. We programmed them to acquire data each hour, and interrogated them from time to time through sands as thick as $3\,\text{m}$. For a few days after burial and before emergence, we could infer probe depth x from our knowledge of sand thermal diffusivity α_s and the lag

$x\sqrt{J/(4\pi\alpha_s)}$ predicted by Eq. (3.6) from solar noon to the time of peak recorded temperature. However, for days in between, temperature oscillations were too small to infer depths $> 0.7\,\mathrm{m}$ in that way.

Probe 1 was first buried on March 26, 2011 at 12:50 Qatar time (09:50 universal time). The avalanche covered it progressively, but it resurfaced and slid about half-way down the incline. It remained there until May 1, 2011, when it finally disappeared as the dune overcame it. The probe and its recording unit resurfaced unscathed on July 6, 2012. Probe 2 remained below the surface from its burial on November 18, 2011 at 16:15 Qatar time until it emerged in March 2013.

Figure 3.1 shows a survey of the dune carried out on July 16, 2012 with a Leica TS-02 theodolite with extended-range ($> 1000\,\mathrm{m}$) electronic-distance-meter. With this instrument, we recorded precisely where probe 1 had emerged a few days earlier. Although the dune changed shape and tack somewhat between April 2011 and July 2012, we estimate that it migrated at constant speed above the immobilized probe 1, such that the latter appeared to "travel" on the reverse path shown as an arrow in Fig. 3.1 relative to the dune. Assuming a uniform dune speed calculated from overall distance travelled and duration between burial and emergence, we then estimated probe depth shown in Fig. 3.6.

3.4.2 Temperature

Once buried deeply, the probes experienced relatively mild temperatures with seasonal variations smaller than diurnal oscillations. To predict them, we developed the two-dimensional thermal model of the dune's interior that is summarized in Appendix B.4 ("Thermal advection-diffusion deep within a mobile dune"). Crucially, this model modifies the thermal Eq. (3.4) to include the dune velocity $\mathbf{U}$ explicitly,

$$\frac{\partial T_s}{\partial t} + \mathbf{U} \cdot \nabla T_s = \alpha_s \nabla^2 T_s. \tag{3.7}$$

Although we did not record the net surface radiation flux over the entire burial period, the sky was generally clear enough to estimate $\dot{q}''_{\text{rad}}$ from solar ephemeris and radiation parameters provided in Appendix B.1. To evaluate the surface convection flux, we first noted that wind speed data from the weather station could be described as a random variable with reproducible diurnal variations and a peak with log-normal distribution, described in Appendix B.3 ("Ambient temperature and wind"). This allowed us to estimate $\dot{q}''_{\text{wind}}$ with a Monte-Carlo technique and, by integrating Eq. (3.4) in a "diurnal boundary layer" below the dune surface (Appendix B.4), find the long-time variations of daily mean surface temperature $\bar{T}_{s_0}$ (Fig. 3.6, top). We then used $\bar{T}_{s_0}$ as a external boundary condition for 2D integration of Eq. (3.7), which captures dune mobility through the constant advection speed $\mathbf{U}$. As Fig. 3.7 and its animation in the supplementary information of Louge et al. [139] illustrate, such advection is crucial to the long time scales that are characteristic of the dune's interior.

Finally, for near-surface depths, we developed the simpler analytical 1D model of Eq. (D7). As Figs. 3.7 and 3.8 show, both models agreed well with measurements. For example, by properly accounting for dune mobility and variations in surface radiation and convection, they correctly predicted a lag of $70\,\text{days}$ between the minimum monthly-averaged ambient temperature in January and the corresponding minimum value later registered by probe 1 in March. As mentioned in section 3.2, because the dune moves at a similar rate than the thermal diffusion speed, ignoring dune advection would have instead

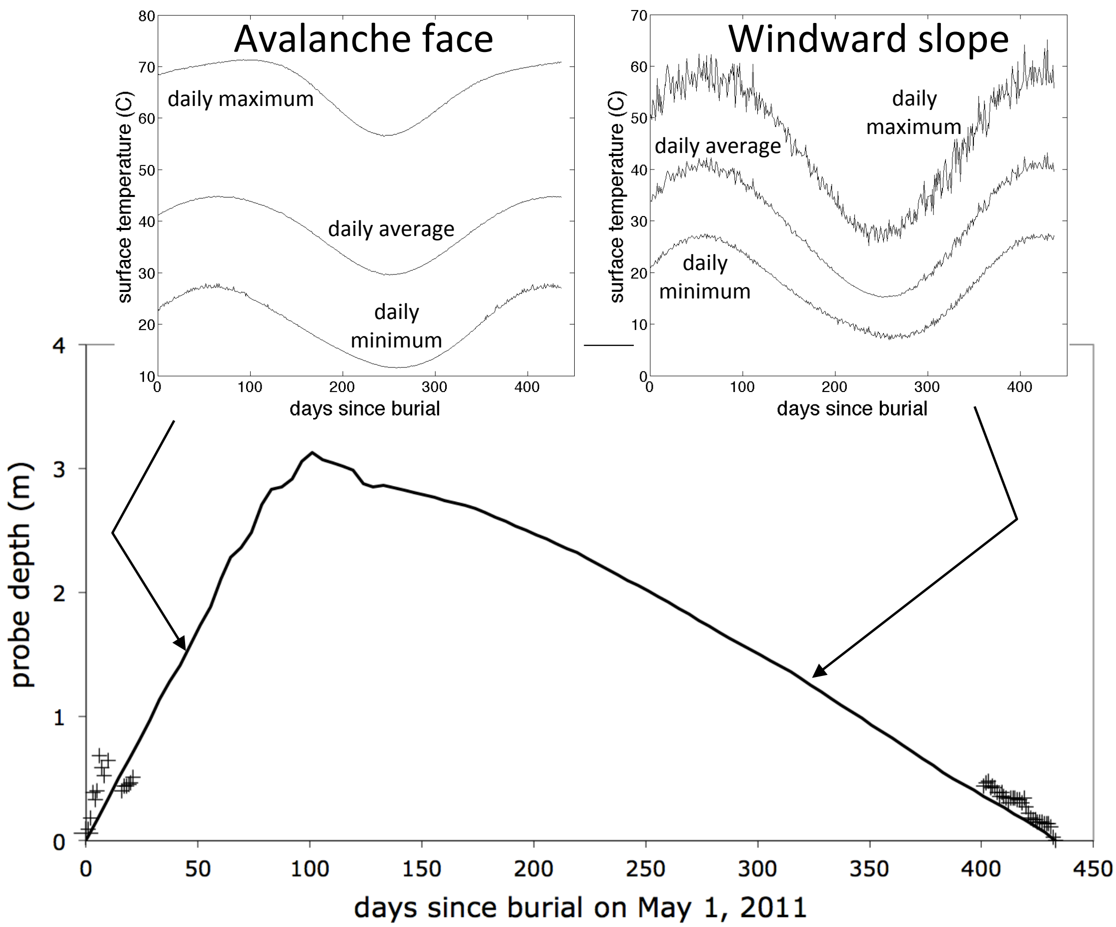

Figure 3.6: Bottom: vertical height of the sand column above probe 1 (line) estimated from the dune profile of Fig. 3.1 and a uniform dune speed $U \simeq 26.2\,\mathrm{m/yr}$ calculated from overall distance travelled and duration between burial and emergence. Such speed is 35% greater than the historical average $18.4\,\mathrm{m/yr}$ visible on Google Earth. Symbols are probe depth, inferred from recognizable time lags between solar noon and peak recorded temperature. Days are counted from April 30, 2011 until July 6, 2012. Top: daily minimum, average and maximum sand surface temperatures calculated as outlined in Appendix B.4 for the leeward avalanche face, assuming no convection (left); and for the windward slope with convection coefficient $\rho c_p \kappa \bar{\zeta} \bar{U}_m / \ln(z_T/\bar{\xi}_0) \simeq 18\,\mathrm{W/m^2.^\circ K}$.

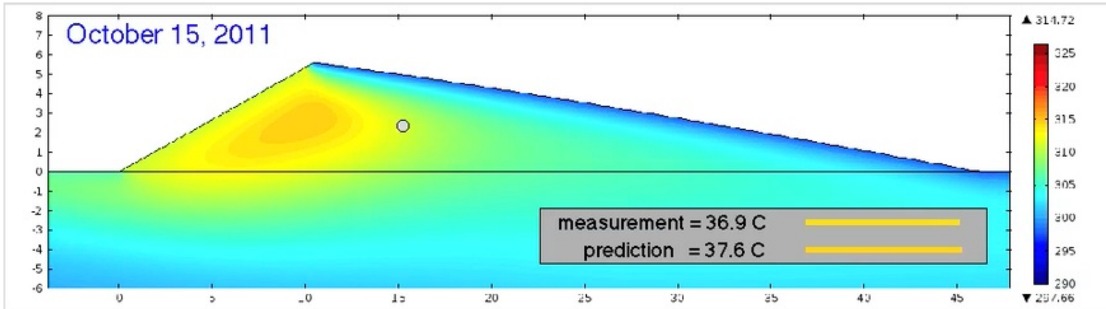

Figure 3.7: Two-dimensional simulation of Eq. (3.7) on the vertical dune cross-section where the buried probe resided (gray circle). The interior color scheme indicates sand temperature in °K. Distances are expressed in m. The inset compares temperatures measured by the buried probe and the corresponding model predictions in °C. The supplementary information of Louge et al. [139] includes an animation of this Fig.

produced erroneous predictions of its deep temperature field.

As Fig. 3.9 shows with probe 2, predictions from the 1D models in mid-2012 reveal dissimilarities in insolation and convection between the leeward and windward faces. As quantified in Appendix B.4, higher insolation and lower convection both contribute to raising the temperature on the leeward face above the corresponding value on the windward slope. Because the 1D model extrapolates surface temperature to the interior, it does not perform well deep within the dune, where temperature is equally affected by all nearby free surfaces. However, a 2D model similar to Figs. 3.7 and 3.8 should lie between the two 1D predictions, and therefore capture buried temperature data more accurately.

Figures 3.8 and 3.9 summarize buried probe observations. In Fig. 3.8, the top panes show the temperature history of probe 1 (red line and symbols), a fit of mean diurnal ambient temperature (dashed blue line) and, when the probe was close enough to the surface, times of sunrises and sunsets. Because our weather station did not operate before November 2011, we assumed that ambient tem-

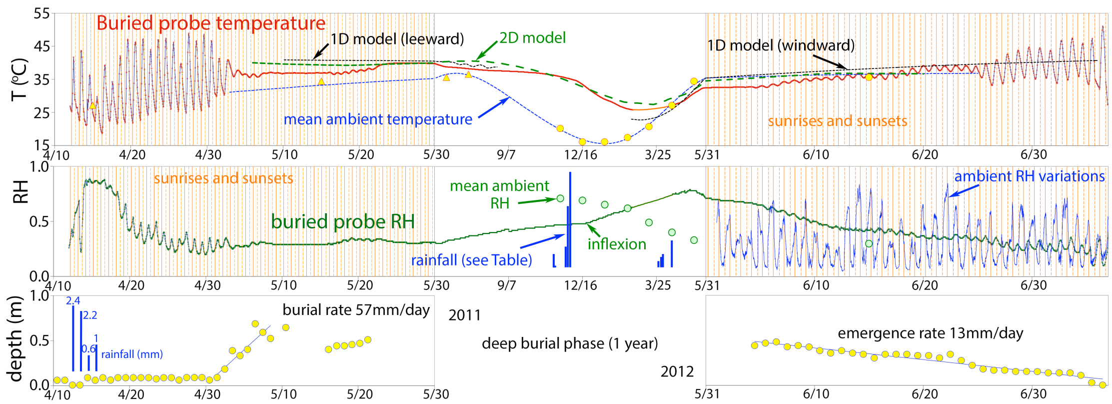

Figure 3.8: Data from probe 1 buried from April 2011 to July 2012. Top: three panes show buried temperature versus time. Time scales are magnified during burial and emergence phases to illustrate near-surface temperature oscillations similar to those discussed in section 3.3. Small red circles are individual buried temperature measurements at one-hour intervals; they merge into a thick red line as diurnal fluctuations attenuate. Vertical orange solid and dashed lines mark sunrises and sunsets, respectively. Data from February 2, 2012 to April 14, 2012 are interpolated from adjacent records when memory overflowed. The blue dashed line is the periodic fit (Eq. C1) of monthly-averaged ambient temperatures measured on our weather station (circles) for 12 months from November 2011. (Triangles are extrapolations from 2012 values for temperatures unrecorded prior to weather station setup). The black dashed line is the 1D thermal model of Eq. (D7). The green dashed line is from the 2D model in Fig. 3.7. Middle: three panes show RH (or water activity, green line), with inflexion around December 17. Blue vertical lines are proportional to rainfall quoted in Table 3.1. The blue line and green circles are, respectively, instantaneous and monthly-averaged relative humidity. Bottom: two panes separated by a whole year show daily burial depth inferred from peak temperature time lags after solar noon. (Rain data courtesy of Mohammad Al Sulaiti of the Qatar Civil Aviation Authority)

peratures were periodic annually, conforming to Eq. (C1), so that records in 2012 could be substituted for earlier times (triangles).

The bottom two panes of Fig. 3.8 show probe distance to the nearest free surface inferred using peak temperature lags from solar noon (Eq. 3.6). As expected from the steeper slope of the avalanche face (Fig. 3.1), burial was faster than emergence. As Fig. 3.6 shows, these inferred depths agree well with those

Table 3.1: Pluviometric record h_R (mm) and significant events. x is probe depth.

date	h_R (mm)	comments
January 2011	18.8	monthly aggregate
February 2011	1.8	monthly aggregate
March 19-21, 2011	0	near-surface diurnal measurements
April 12, 2011	2.4	
April 13, 2011	2.2	
April 14, 2011	0.6	
April 15, 2011	1.0	two weeks before probe 1 disappeared
May 1, 2011	0	probe 1 disappears in nearly dry sand
November 7, 2011	1.8	
November 9, 2011	0.2	
November 18, 2011	0	probe 2 is buried
November 23, 2011	2.8	moisture rises around probe 2
November 26, 2011	8.2	
November 27, 2011	1.2	
November 28, 2011	0	probe 2 reaches RH $\simeq 1$
November 29, 2011	12.8	
November 30, 2011	0.2	
December 5-17, 2011	0	probe 1 at $x \simeq 2.8\,\mathrm{m}$ feels November rains
March 26, 2012	0.8	
March 30, 2012	1.4	
March 31, 2012	0.2	
April 1, 2012	1.8	
April 2, 2012	0.4	
April 13, 2012	3.6	
June 21, 2012	0	RH at probe 2 becomes < 1
July 6, 2012	0	probe 1 surfaces
October 4, 2012	0.2	
December 1, 2012	0.2	
December 16, 2012	6.8	probe 2 at $x \simeq 0.6\,\mathrm{m}$
March 17-22, 2013		emergence of probe 2

calculated from the dune profile advancing at constant speed.

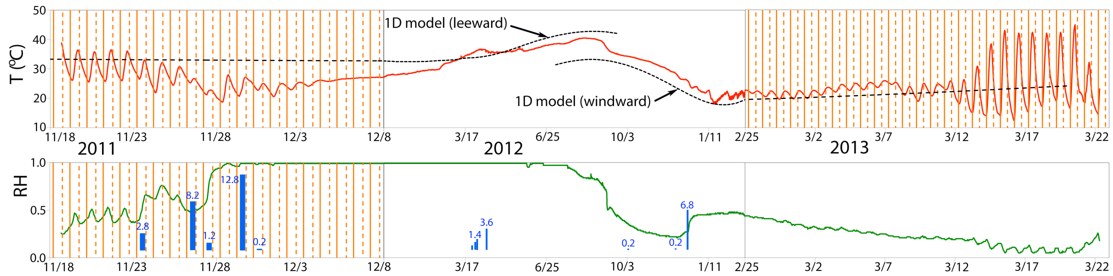

Figure 3.9: Data from probe 2. Lines, see Fig. 3.8. Top: buried temperature versus time from November 2011 to March 2013 with magnified time scales during burial and emergence phases. The 1D models are based upon the respective leeward and windward surface temperatures calculated in Appendix B.4. Bottom: relative humidity and rain records.

3.4.3 Moisture

The middle three panes in Figs. 3.8 and 3.9 show deep moisture records, with superimposed precipitation from Table 3.1. We interpret these data by modeling sand desorption and wetting using the equation of [177]

$$\frac{\partial \theta}{\partial t} = \nabla \cdot \Big[\frac{K}{\mu_w}(\rho_w g \hat{\mathbf{z}} - \frac{\partial \Psi}{\partial \theta} \nabla \theta)\Big], \tag{3.8}$$

which governs the evolution of the water volume fraction $\theta \simeq \rho_s \Omega / \rho_w$ in a porous sand of solid volume fraction ν, material density ρ_m and bulk density $\rho_s = \nu \rho_m$. In Eq. (3.8), μ_w and density ρ_w are, respectively, the dynamic viscosity and density of liquid water, g is gravitational acceleration, $\hat{\mathbf{z}}$ is the upward vertical unit vector, $\Psi > 0$ is capillary suction pressure, and K is the unsaturated permeability at θ. Although sand, like any soil with a distribution of pore size, exhibits a hysteretic water retention curve that we derived in chapter 2, desorption from saturation at $\theta = 1 - \nu$ has a limiting behavior that is conveniently modeled as $\theta = (1 - \nu)$ for $\Psi < \Psi_a$ and

$$\theta = (1 - \nu)(\Psi_a / \Psi)^{1/b} \tag{3.9}$$

otherwise [26], where Ψ_a is the "air entry potential", i.e. the suction pressure one must exceed to force air into the saturated porous medium. Although the initial water volume fraction is generally $< 1-\nu$ after desert rains, we adopt the formulation of Eq. (3.9) to derive simple analytical expressions for desorption of our sands. First, to estimate the unsaturated permeability K, we substitute it in the heuristic correction of Brooks and Corey [33]

$$K = K_0\Big(\frac{\theta}{1-\nu}\Big)^2 \frac{\int_{\theta'=0}^{\theta} d\theta'/\Psi^2}{\int_{\theta'=0}^{1-\nu} d\theta'/\Psi^2} = K_0\Big(\frac{\theta}{1-\nu}\Big)^{2b+3}, \tag{3.10}$$

where K_0 is the saturated sand permeability. In this case, Eq. (3.8) may be written

$$\frac{\partial\theta}{\partial t} + \mathbf{u}_{\text{eff}} \cdot \nabla\theta = \nabla \cdot \left(D_{\text{eff}}\, \nabla\theta\right), \tag{3.11}$$

with effective non-linear advection velocity

$$\mathbf{u}_{\text{eff}} = -\left[\frac{\rho_w g K_0}{\mu_w(1-\nu)}\right]\,(3+2b)\,\Big(\frac{\theta}{1-\nu}\Big)^{2b+2}\hat{\mathbf{z}}. \tag{3.12}$$

and diffusion coefficient

$$D_{\text{eff}} = \Big[\frac{\psi_a K_0}{\mu_w(1-\nu)}\Big]\; b\,\Big(\frac{\theta}{1-\nu}\Big)^{b+2}, \tag{3.13}$$

leading to a local Péclet number $u_{\text{eff}}\sqrt{K}/D_{\text{eff}} = (\rho_w g\sqrt{K_0}/\Psi_a)[(3+2b)/b][\theta/(1-\nu)]^{(3+2b)/2}$ sharply decreasing with θ. Therefore, because θ quickly falls as rain permeates the porous surface, diffusion controls desorption over long times. (This phenomenon is similar to the wetting of porous soils, where diffusion dominates advection at low θ, implying shallow water penetration. Conversely, at high θ near saturation, advection prevails).

To obtain analytical predictions for long-term moisture desorption, we assume that rain is initially accumulated at a uniform volume fraction over a thin layer, that evaporation or advection are negligible, and that the RH probe remains buried at the center of this region. Then, as Appendix B.6 ("Water desorption") shows , the solution of Eq. (3.11) is

$$\theta_p = (1-\nu)\left[\frac{h_R^2\mu_w}{(1-\nu)4\pi t\Psi_a K_0 b}\right]^{\frac{1}{4+b}}, \tag{3.14}$$

which decays rapidly at first, but then much more slowly. After rains of $h_R \simeq 27.2\,\mathrm{mm}$ fell in November 2011, Eq. (3.14) predicts that it would take $\simeq 240\,\mathrm{days}$ to desorb sands down to $\Omega = 1\%$. This predicted duration is on the order of the 200-day plateau at high water activity that "probe 2" experienced.

Without knowledge of pore geometry statistics similar to Fig. 2.3, we describe the wetting of initially dry sands by deducing its limiting retention curve from Eq. (3.9) using the heuristic construction that Parlange [161] proposed. As outlined in Appendix B.7 ("Wetting"), we then calculate the time t_p required for rainwater to penetrate a dry dune to the depth x_p,

$$t_p = \left[\frac{(2-b)\mu_w(1-\nu)x_p}{(4+b)(3+2b)\rho_w g K_0}\right]^{\frac{4+b}{2-b}}\left[\frac{(1-\nu)4\pi\Psi_w K_0 b}{h_R^2\mu_w}\right]^{\frac{2+2b}{2-b}}. \tag{3.15}$$

Combining with Eq. (3.14), we then estimate the peak water volume fraction at that depth,

$$\theta_p \simeq (1-\nu)\left[1+\frac{1}{b}\right]^{\frac{b(2+2b)}{(2-b)(4+b)}}\left[\frac{(4+b)(3+2b)h_R^2\rho_w g}{(2-b)(1-\nu)^2 4\pi b x_p\Psi_a}\right]^{\frac{1}{2-b}}. \tag{3.16}$$

These Eqs. imply that it only took $12\,\mathrm{days}$ for the November 2011 rains with cumulative $h_R \simeq 27.2\,\mathrm{mm}$ to reach "probe 1" buried down to $x_p \simeq 2.8\,\mathrm{m}$. This prediction has the right order of magnitude: Following the last major rainfall on November 29, "probe 1" recorded a noticeable downward temperature inflection $6\,\mathrm{days}$ later, and humidity visibly edged upward another $12\,\mathrm{days}$ afterwards (green arrow in Fig. 3.8). Equations (B.30) and (B.31) also show that substantial water can quickly sink to the depth $x_J = \sqrt{\alpha_s J/\pi}$ below which harsh diurnal temperature variations are inconsequential. For example, they predict that the $12.8\,\mathrm{mm}$ rain falling on November 29 reached $x_J \simeq 10\,\mathrm{cm}$ at the volume fraction $\theta_p \simeq 0.11$ in a mere $28\,\mathrm{min}$.

In short, the data support four principal conclusions. First, humidity around deep sand grains crucially depends on whether or not precipitation occurred when those grains were trapped below the leeward avalanche face. As Figs. 3.8 and 3.9 show, probe 1 finally disappeared below the surface two weeks after the last major rain, thus allowing sands to dry up around it. In contrast, because probe 2 was sunk just ahead of major precipitation, it recorded elevated relative humidity for 8 months.

Second, as probe 1 recorded shortly after precipitations in November 2011, some rain moisture quickly reaches depths at which it was sheltered from harsh diurnal ambient variations. Equations (B.30) and (B.31) capture this behavior by modeling water penetration.

Third, as probe 2 reveals, rainwater initially adsorbed on leeward-trapped sands can maintain high relative humidity nearby for a long time. As Eq. (3.13) suggests, this is because the effective diffusion of liquid water decreases as a power > 2 of volumetric water content θ, and thus keeps on slowing down during water desorption. This deep sustainability of rain moisture, which follows rapid water drainage and aeolian deposition of dry sands leeward, explains why Louge et al. [136] had observed more humid sands below the windward surface than near the crest of a mobile barchan dune in the Sahara.

Fourth, deep moisture emerging on the windward slope gradually dries up as it approaches the surface. There, variations in relative humidity become tied instead to a diurnal cycle similar to the one in Fig. 3.4. Thus, although morning dew might still produce a relatively high relative humidity affecting surface cohesion, such an effect remains ephemeral.

3.5 Microbiological implications

To gauge whether sufficient moisture is available for microorganism survival, microbiologists invoke the "activity" a_w of a water solution, which at equilibrium is equal to the relative humidity of the surrounding moist air, $a_w =$ RH [87]. To compete for water against nearby hydrophilic minerals, live microbes typically require $a_w \gtrsim 0.7$ [155], unless they are "xerophiles" that can withstand extreme desiccation [20, 165].

Adopting this benchmark, we identify regions within the sand dune where the threshold is reached. First, we note that Figs. 3.8 and 3.9 paint very different pictures of deep habitat around the two buried probes. Because probe 1 disappeared below the surface at a time when the surrounding sands were dry, it experienced a relative humidity less than what Mugnier and Jung [155] consider necessary to support microbes, except in the period from March 28 to June 1, 2012, when moisture gradually rose following deep penetration of rain water in November 2011. In contrast, because probe 2 was sunk just ahead of major precipitation, it recorded elevated water activity for 8 months in a range known to sustain microbial life. Crucially, once either probe reached a depth $\sim 20\,\mathrm{cm}$ where diurnal temperature variations disappear, temperature remained relatively mild throughout deep burial. This suggests that moisture alone governs microbial viability deep in the dune.

The data also implies that moisture is trapped locally, rather than distributed uniformly. As Eqs. (3.12)-(B.31) showed, because effective advection and diffusion of liquid water slow down with decreasing volume fraction, a small amount of rain moisture can endure for several months near the buried sands that collected it. In fast-moving mobile dunes, much of the moisture deposited by rain on the windward slope can be lost to aeolian drying and erosion. In contrast, moist sands trapped below the leeward avalanche face behave like probe 2, remaining humid until they emerge upwind. Therefore, individual regions within a relatively fast-moving mobile dune can possess (or not possess) sufficient moisture for microbial activity, depending on whether or not rain fell on the avalanche face months earlier. If they do, then moisture can persist much longer than typical microbial incubation times. As sands approach the surface, rain falling overhead can also add to their moisture. However, by and large, deep sands "remember" whether or not precipitation fell as they were trapped on the leeward avalanche.

Meanwhile, diurnal data from the near-surface instruments of section 3.3 confirmed that temperature is mild, steady and invariant at depths $x \gtrsim 20\,\mathrm{cm}$, while humidity remains nearly constant. As Fig. 3.4 showed, diurnal humidity variations were limited to depths $x \lesssim 5\,\mathrm{cm}$. Water activity then gradually increased with x, reaching a level conducive to microbial survival for $x > 11\,\mathrm{cm}$.

Using the live stain technique of Gommeaux et al. [84], our colleagues Anthony Hay and Sara Abdul-Majid confirmed that microbes were present on sand grains sampled below the upwind slope of the same dune (Fig. 3.10). There, they also found evidence of biological respiration by collecting gas samples at depths of 30, 60 and $90\,\mathrm{cm}$ in April 2012. To that end, they used a AMS gas-

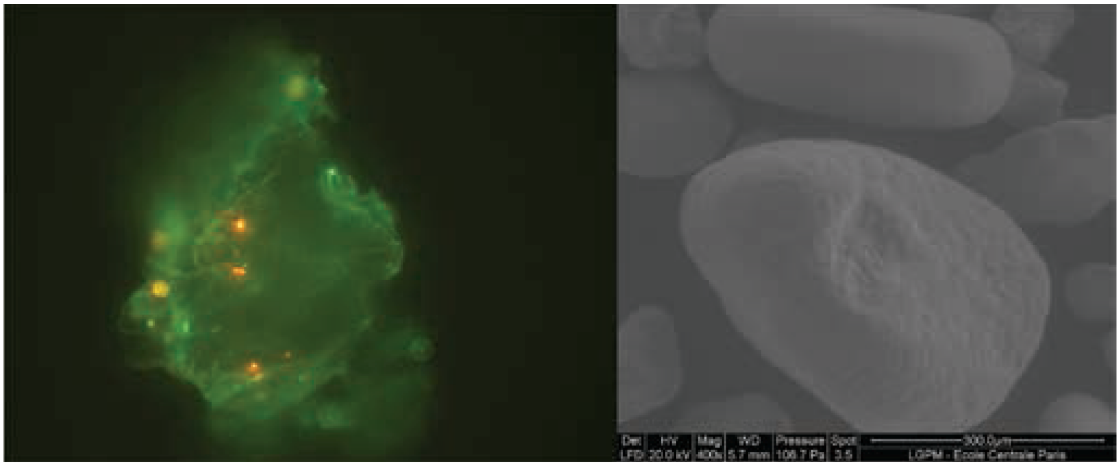

Figure 3.10: Microbial life on a Qatar dune sand grain. Left: Fluorescence micrograph of a single sand grain showing an abundance of bacteria. (Data courtesy of Anthony Hay) Live cells stained green with Syto 9 using a technique similar to Gommeaux et al. [84]. Cells stained red/orange with propidium iodide are dead or dormant (400x magnification using a Zeiss Axio LSM 710 Fluorescence Microscope). Right: image of a similar sand grain from an FEI Quanta 200 Environmental Scanning Electron Microscope (ESEM) in low vacuum mode. (Photograph courtesy of Nathalie Ruscassier) We report particle-size-distribution is Appendix B.5 ("Dunes, sand size and mass") of the supplementary information.

vapor-sampling kit connecting a conical tip via a teflon tube to a brass fitting hermetically holding a septum stopper. They withdrew dune gases through the septum using a syringe needle and, after quickly purging possible air contaminants, injected a sample by piercing the rubber septum of a vacutainer, slightly pressurizing the latter, so no gas could contaminate its contents during travel to Cornell's Stable Isotope Laboratory. There, a Thermo Delta V isotope ratio mass spectrometer interfaced to a "Gas Bench II" analyzer compared their stable isotope molar ratio $\Gamma \equiv {}^{13}\mathrm{CO}_2/{}^{12}\mathrm{CO}_2$ against the same ratio Γ_0 in the Vienna Pee Dee Belemnite standard [157]. Because respiration typically discriminates against ${}^{13}\mathrm{CO}_2$, its resulting $\delta^{13}\mathrm{C} \equiv (\Gamma/\Gamma_0) - 1$ is smaller than in CO_2 from abiotic origins.

First, our colleagues noted that the CO_2 mole fractions $511 \pm 25\,\mathrm{ppm}$ in the

17 samples collected were larger than the atmospheric value $391 \pm 4\,\mathrm{ppm}$. Then, they found that their $\delta^{13}\mathrm{C} = -12 \pm 1‰$ was not only under the value of $\delta^{13}\mathrm{C} \simeq -8‰$ in atmospheric CO_2, but it was also well below observations of $\delta^{13}\mathrm{C} = +2 \pm 1‰$ from carbonates present in the same dry sand. (Our colleagues found no significant variations in the mole fractions or the $\delta^{13}\mathrm{C}$ of CO_2 with depth $> 30\,\mathrm{cm}$). Therefore, CO_2 collected below the surface was partially of biological origin, adding further evidence to the microscopic observations in Fig. 3.10.

Finally, our colleagues Renee Richer, Sara Abdul-Majid, and Aurora Castilla frequently spotted on several mobiles dunes the "sand fish" *Scincus mitranus* seeking shelter by burrowing through the softer avalanche face [5], as well as insects like the desert beetles *Pimelia arabica* and *Adesmia cancellata*. These encounters suggested that hyper-arid mobile dunes also offer a hospitable habitat to creatures other than microbes.

3.6 Conclusions

Toward determining whether the protected core of hyper-arid mobile sands presents a habitat with the potential to support microbes, we reported measurements of temperature and moisture below the surface of a barchan dune in Qatar on two widely different time scales and depths.

On a diurnal period, strong variations in radiative and convective thermal fluxes were attenuated within the first $10\,\mathrm{cm}$ from the surface. Despite hyper-arid ambient conditions, we observed in March 2011 that relative humidity at depths $\gtrsim 11\,\mathrm{cm}$ exceeded 0.7, a threshold above which microbiological development is possible [155]. In fact, based on recorded CO_2 mole fraction and carbon isotope ratios, our collaborators found that respiration occurred below the surface and was partially of biotic origin, confirming their detection of microbes on collected sand grains.

We then measured humidity and temperature at greater depths using probes initially inserted through the leeward avalanche face, gradually overcome by the mobile dune, and emerging windward 15 months later. Treating dune motion as a uniform advection superimposed on thermal diffusion, our analysis showed that deep temperature is predictable from wind statistics, crucially depends on dune speed, and lags stronger ambient seasonal variations. Deep temperatures were also mild and stable, suggesting that microbial viability at depths $> 10\,\mathrm{cm}$ is governed by moisture alone.

With these self-buried autonomous probes, we observed that deep moisture was largely determined by random precipitation that had occurred months earlier on the leeward avalanche face. Our analysis then showed why such moisture could endure on sand grains, until the latter finally emerged on the windward slope. Therefore, unlike temperature, moisture deep within a mobile dune depends too strongly on random rains to be predictable ahead of time. Dune mobility gives rise to the apparent travel of this moisture windward, creating a complex patchwork of diverse humidity levels below the upwind slope. Because deep moisture dries up as it resurfaces windward, relative humidity within $5\,\mathrm{cm}$ of the surface follows diurnal ambient variations. At dawn, our records of March 2011 suggested that it might reach sufficient levels to affect sand cohesion temporarily.

We showed that hyper-arid barchans conceal regions of moderate temperature and sufficient humidity allowing microbes to exist. Judging from the importance of biological soil crusts in limiting soil erosion [*Bowker et al.*, 2008], one wonders whether some of these microbes could be harnessed to fix the surface of mobile dunes.

CHAPTER 4

PORE PRESSURE IN A WIND-SWEPT RIPPLED BED

4.1 Introduction

Winds blowing over desert sand seas create rippled surfaces on porous sand beds [14, 15, 48, 9, 47, 43]. As Kuzan et al. [127], Buckles et al. [34] and Gong et al. [85] found in water and air, turbulent flows on wavy surfaces produce pressure variations due to streamline expansion and contraction [96]. In permeable sands below the surface, Louge et al. [136] showed that these variations induce a kind of aeolian-driven “seepage”, whereby air penetrates ripple troughs where surface pressure is highest, and re-emerges at crests, where it is lowest. Although porous media are known to present an unusual boundary condition to external flows [19, 116, 156], it is unclear how seepage affects a turbulent boundary layer modulated by permeable ripples.

A related question is whether seepage causes porous ripples to act as a significant sink of aeolian dust below the sand suspension threshold. As long as wind speed is not fast enough to mobilize the more compact base on which ripples travel, Louge et al. [137] predicted that, despite its small velocity, seepage entrains dust below ripple troughs by a peculiar capture mechanism that is *enhanced* by wind, whereas conventional dust deposition processes arise with *weakening* wind and reduced turbulence [170, 86]. A similar process brings benthic nutrients through underwater ripples [145, 109, 79]. It may also contribute to hyporheic flow in river beds [29, 198] and seepage in lake sediments [158]. Although predicted by theory, this dust sequestration mechanism has yet to be fully quantified, since it is unknown how the underlying porous medium affects the turbulent flow responsible for the surface pressure variations that drive seepage.

Louge et al. [137] also suggested that the threshold for the onset of aeolian transport, which had hitherto been exclusively associated with the shearing of surface grains [14, 196], could be lowered by seepage-induced body forces, as pore pressure gradients within specific regions of the wavy permeable bed help relieve part of its weight. To establish whether these forces affect the transport threshold, it is necessary to quantify the pressure field that the turbulent flow induces within the permeable bed.

Because numerical simulations rely on turbulence closures in the free-stream [227, 40, 169] and on semi-empirical boundary conditions at the porous surface [19, 39], they are no substitute for experiments to evaluate the pore pressure field within a permeable wavy bed. For example, while Cardenas and Wilson [36] simulated the one-way coupling from main flow to seepage, they did not consider conversely how the porous substrate affects the main flow. On the dune scale, such omission is legitimate. However, as the simulations of Chan et al. [39, 40] and the experiments of Manes et al. [140, 141] showed for flat surfaces, substrate porosity can modify the turbulent boundary layer. Recently, [27] used particle-imaging-velocimetry to demonstrate that flows over porous triangular bedforms of coarse gravel differ significantly from those over impermeable surfaces of similar geometry. For these highly-separated flows, they noted that the permeable bed thwarts reattachment of the boundary layer by letting fluid pass through its interior. Therefore it is likely that a porous surface affects turbulence on the ripple scale. Yet it remains unclear whether such effect is limited to coarse beds.

Meanwhile, there exists a mature literature on turbulent flows over impermeable sinusoidal surfaces that includes experiments [119, 85, 34], theory [126, 73, 74], numerical simulations [98] and stability analyses [177, 58, 202, 43]. Most of these studies focused upon variations of the surface shear stress. Although there are limited measurements of mean surface pressure [119, 34, 98], no experiment or simulation has yet involved a porous sinusoidal substrate. Intriguingly, Gong et al. [85] observed that surface pressure on an impermeable sinusoidal surface with aerodynamic roughness $\xi_0 \simeq 400\,\mu\mathrm{m}$ is significantly smaller than on a smoother one with $\xi_0 \simeq 30\,\mu\mathrm{m}$, thus bringing to light the role played by microscopic surface features.

In short, it is unclear how porosity affects the turbulent boundary layer above a rippled surface. This raises the following questions: (1) Does porosity modify the surface pressure gradient that drives the flow and, if so, for what size of bed particles? (2) In light of differences between the rough and smooth data of Gong et al. [85], what is the magnitude of pressure variations on a porous substrate? (3) Are internal pore pressure gradients sufficient to produce seepage-induced dust sequestration beneath ripple troughs? (4) By relieving gravity, could these gradients affect the threshold for aeolian transport, traditionally attributed to surface shear stress alone? (5) What is the role of ripple aspect ratio?

To address these questions, we used a wind tunnel to record the pore pressure field within two artificial porous media with sinusoidal surface of wavelength $\lambda = 100\,\mathrm{mm}$ and half vertical trough-to-crest distance $h_0 = 3\,\mathrm{mm}$ and $6\,\mathrm{mm}$. We discerned the role of permeability by comparing our records of pressure on a porous surface to similar measurements on impermeable sinusoidal walls, the only shape for which such data have been published. As we discuss in this article, variations of surface pressure and shear stress scale with the aspect ratios h_0/λ, which is half the inverse of the "ripple index" RI $\equiv \lambda/(2h_0)$.

Ripples feature a wide variety of shapes that are normally asymmetric [205]. However, when h_0/λ is small, their cross-section can be sinusoidal [13, 137], likely for the absence of major flow recirculation behind crests. Although aeolian ripples are often triangular with a steeper leeward face, our experiments staged ripples of sinusoidal cross-section for three reasons. First, we endeavored to compare them with the mature literature on impermeable waves, which exclusively reported surface pressure on sinusoidal shapes. Second, adopting an asymmetric cross-section would have introduced an additional geometrical aspect ratio beside the single parameter h_0/λ, thus multiplying experimental rigs and complicating interpretation. Third, by comparing two sinusoidal ripples straddling a wide range of ripple index, we could gauge how this single parameter affects pressure within the ripple and on its surface, thus informing future modeling of the turbulent boundary layer and its suspension threshold.

4.2 Experiments

Measurements of pore pressure present exceptional challenges in shifting sands, even below the saltation threshold. First, wind-driven porous media produce tiny signals of only a few Pa amid turbulent fluctuations. Second, at wind speeds that make pore pressures detectable, erodible sand does not remain in place long enough to fix measurement locations precisely within ripples of millimetric amplitude. In underwater experiments, Elliott and Brooks [56] and Pack-

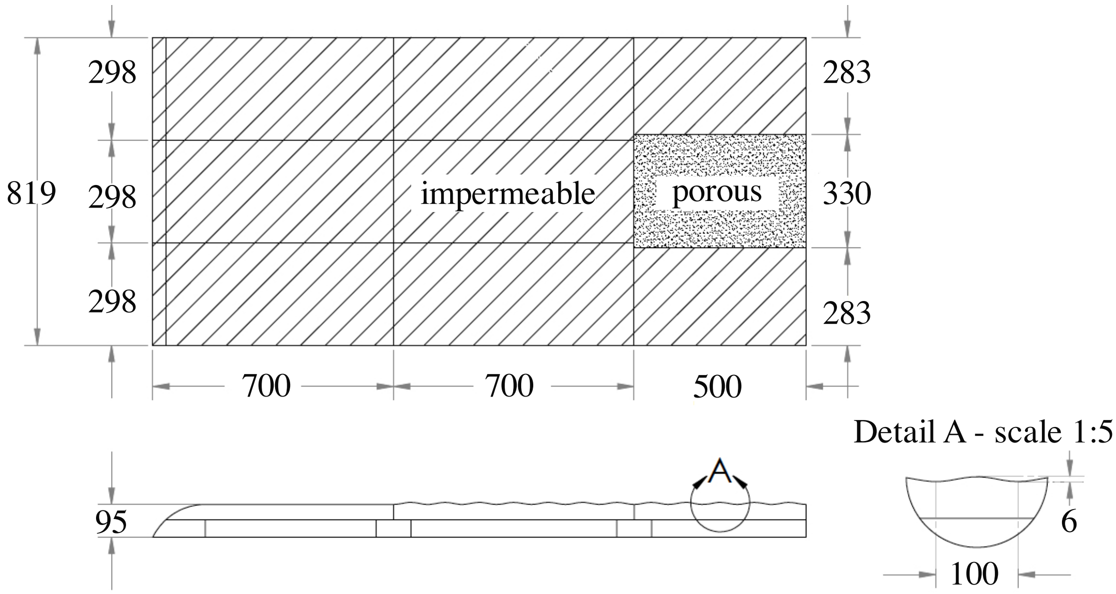

Figure 4.1: Drawing of the artificial rippled bed with $h_0/\lambda = 3\%$. (Facility built by Ryan Musa, Brian Mittereder, and Michael Berberich.) Dimensions in mm. Flow is from left to right. The rig with $h_0/\lambda = 6\%$ has similar design. (Facility built by Amin Younes and Frank Parish.)

man et al. [160] observed the flow of tracers through moving bedforms, but they did not measure pressure directly. Therefore, to expose how ripple porosity affects the turbulent boundary layer, our experiments employed a porous plastic with a permeability value that is similar to aeolian sands.

We conducted experiments in the wind tunnel described by Ribando [175] with cross-section $\simeq 1.2\,\mathrm{m}$ wide $\times$ $1\,\mathrm{m}$ high, fetch $\simeq 12\,\mathrm{m}$, featuring six variable-inlet-guide-vane tube axial exhaust fans of $11\,\mathrm{kW}$, each contributing $\simeq 5.5\,\mathrm{m/s}$ to the average wind speed U. Thus, to test how robustly pore pressure scales with the kinetic energy density $(\rho/2)U^2$ of air, we explored a wider range of speeds than typically observed in aeolian processes.

The rippled bed sketched in Fig. 4.1 was manufactured on a Computer Numerical Control (CNC) milling machine. It consisted of three parts: (1) along the flow direction, a developing impermeable RENSHAPE™plastic section with bluff nose and flat range, (2) transitioning smoothly to the first trough of a similar plastic surface with seven sinusoidal ripples of crestlines perpendicular to the flow, long enough to establish a periodic flow [85], and (3) ending with a porous plastic test section of five full wavelengths with similar cross-section around the assembly centerline, and flanked on both sides with similar RENSHAPE™ripples. Although its solid volume fraction $\nu_G \simeq 0.4$ was smaller than a packed granular solid, the porous GENPORE™plastic had a permeability $K = 3.4 \pm 0.9\, 10^{-11}\,\mathrm{m}^2$, corresponding to a mean pore diameter $\simeq 50\,\mu\mathrm{m}$, typical of desert sands [136].

To study the role of h_0/λ, Cornell undergraduate students manufactured two similar test beds featuring ripples of $h_0 = 3\,\mathrm{mm}$ and $6\,\mathrm{mm}$, carved in porous plastic with respective thickness $H = 32.5\,\mathrm{mm}$ and $42\,\mathrm{mm}$ (Table 4.1). The aspect ratio $h_0/\lambda = 3\%$ represented the smallest value that would produce detectable pressure signals. (However, as our measurements will indicate, any ripple of smaller aspect ratio should exhibit predictable pore pressure variations scaling with $\rho U^2 h_0/\lambda$).

We define a 2D cartesian coordinate system with unit vectors $(\hat{\mathbf{x}}, \hat{\mathbf{y}})$ along the flow and along the *downward* vertical, respectively, with origin in air above the leading trough at an elevation midway between trough and crest, such that the free surface satisfies

$$y = h_0 \cos\left(2\pi x/\lambda\right). \tag{4.1}$$

The third complete trough-crest-trough wavelength downstream of the leading edge of the porous section featured stainless steel tubes of $1.75\,\mathrm{mm}$ inside diameter inserted from below and snugly press-fit to the proper depth. The facility

Table 4.1: Experimental conditions and harmonic fits to the data using Eq. (4.14). The ratio $A_t \equiv u_*/U$ was recorded just ahead of the rippled section. Pressures marked with an asterisk are made dimensionless using Eq. (4.11) assuming $\rho = 1.2\,\mathrm{kg/m^3}$. p^*_{min} and p^*_{max} are their extrema on the surface. Overbars indicate that coefficients were fitted from the average $\overline{(p/\rho U^2)}(\lambda/h_0)$ among six experiments, each adding one more fan to the previous one. F_{min} and F_{max} are minimum and maximum values of F in Eq. (4.30) with $\tan\alpha = 0$. P^*_x and P^*_y are dimensionless forces on a unit ripple width in the x and y-directions from Eqs. (4.25) and (4.26), respectively. v^* is the dimensionless overall seepage into the porous bed through the ceiling of the box at $y = H$ calculated using Eq. (4.27). $v^* > 0$ means that the ripple inhales (for $h_0/\lambda = 3\%$) and $v^* < 0$ that it exhales (for $h_0/\lambda = 6\%$). Errors are 95% confidence intervals. (Data was acquired with Ryan Musa, Michael Berberich, Smahane Takarrouht, and Cian Carroll, with help from Daniel Balentine and Matthew Pizzonia.)

h_0 (mm)	3	6
λ (mm)	100	100
H (mm)	32.5	42
$A_t \equiv u_*/U$	0.0368 ± 0.0034	0.0383 ± 0.0058
$\bar{p}^*_1$	2.186 ± 0.139	1.057 ± 0.107
$\bar{p}^*_2$		0.371 ± 0.170
$\bar{p}^*_3$		-0.140 ± 0.099
$\bar{p}^*_a - p^*_0$	0.203 ± 0.087	0.085 ± 0.063
$\bar{\phi}_1$ (rad)	-0.186 ± 0.072	-0.499 ± 0.115
$\bar{\phi}_2$ (rad)		-2.28 ± 0.43
$\bar{\phi}_3$ (rad)		-0.02 ± 1.55
$\bar{p}^*_d$	2.2 ± 1.8	3.38 ± 0.38
n	80	90
ϕ_d (rad)	1.57	1.7
$p^*_{\mathrm{max}} - p^*_0$	1.98 ± 0.14	0.71 ± 0.15
$p^*_{\mathrm{min}} - p^*_0$	-2.52 ± 0.20	-2.06 ± 0.31
F_{max}	16.7 ± 1.1	15.1 ± 5.7
F_{min}	-12.5 ± 0.8	-8.7 ± 2.1
P^*_x	0.043 ± 0.016	0.085 ± 0.025
P^*_y	-0.09 ± 0.11	-0.64 ± 0.08
v^*	0.37 ± 0.32	-1.11 ± 0.20

with $h_0/\lambda = 3\%$ possessed 36 such tubes and the one with $h_0/\lambda = 6\%$ had 30. Each porous test section was bounded underneath by a box enforcing a calm, uniform ambient pressure p_0 on its ceiling located at $y = H$ (Fig. 4.1).

To minimize cross-calibration errors among all pore pressure measurements, the steel tubes were connected to a SCANIVALVE™(no longer available commercially, but equivalent to equipment made by VALCO™Instruments Co) that multiplexed them to a single MKS 120-A BARATRON™differential pressure transducer with $\simeq 1.33\,\mathrm{kPa}$ full scale, $10^{-3}\,\mathrm{Pa}$ resolution and 0.05% reading accuracy.

To verify that the turbulent boundary layer was fully-developed before reaching the rippled section, we recorded vertical profiles of mean air speed above the free surface using a DWYER™471-3 hot-wire anemometer with vertical resolution $\simeq \pm 1.5\,\mathrm{mm}$ and, wherever the profile conformed to Prandtl's law-of-the-wall, we extracted the shear velocity u_* by fitting data to

$$u = (u_*/\kappa)\ln(z/\xi_0), \tag{4.2}$$

where z is vertical upward elevation above the mean porous surface, ξ_0 is the "aerodynamic roughness", and $\kappa \simeq 0.41$ is von Kàrmàn's constant.

From these profiles, Buckles et al. [34] and Henn and Sykes [98] defined the bulk wind speed U as the mean speed integrated across the channel. Because the turbulent boundary layer is characterized by the shear velocity u_*, one may be tempted to scale pressures with u_* rather than U. However, because shear stress evolves along a slanted surface [114, 126, 100], the bulk speed U, which is invariant along the ripple, is a more robust characteristic of the locally undulating flow.

As Fig. 4.2 illustrates, a turbulent boundary layer with nearly uniform thick-

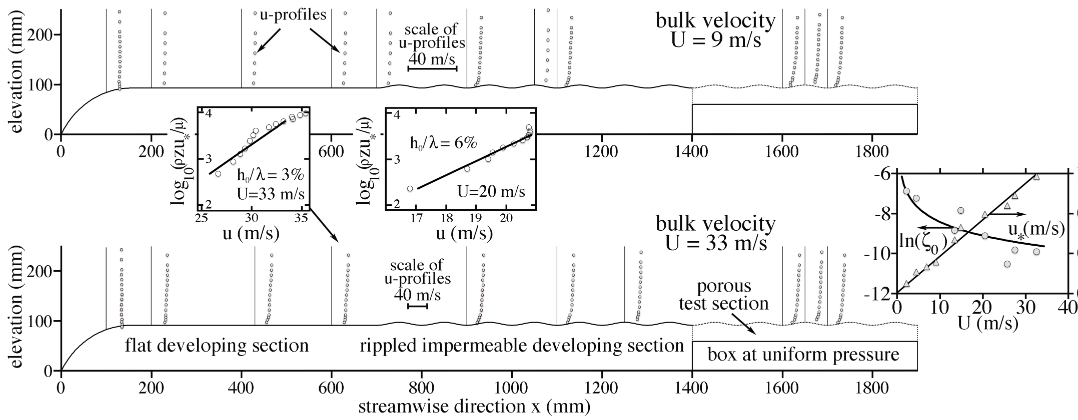

Figure 4.2: Streamwise evolution of velocity profiles for the rig in Fig. 4.1 at bulk velocities $U \simeq 9\,\mathrm{m/s}$ (top) and $33\,\mathrm{m/s}$ (bottom). Distances are in mm. Sections are identified in the bottom graph. Vertical lines are axes $u = 0$ and mark locations where profiles of time-averaged velocity u were recorded. Horizontal segments show a scale of $40\,\mathrm{m/s}$ for these profiles. The left inset is a semi-log profile of the wall coordinate $\log_{10}(\rho z u_*/\mu)$ vs u at the end of the flat developing section for this facility with $h_0/\lambda = 3\%$ at $U \simeq 33\,\mathrm{m/s}$. The straight line is a fit to Eq. (4.2) yielding aerodynamic roughness ξ_0 and u_* quoted in Table 4.1 at 95% confidence. The middle inset is for $h_0/\lambda = 6\%$ at $U \simeq 20\,\mathrm{m/s}$. The right inset shows the overall dependence of $\ln(\zeta_0) \equiv \ln(2\pi\xi_0/\lambda)$ (left axis, dimensionless) and shear velocity u_* (right axis, m/s) on U (m/s) for both rigs at $h_0/\lambda = 3\%$ and 6% over the whole range of bulk velocity considered.

ness and stable shear velocity was well-established before the end of the flat section. Following Zilker and Hanratty [231], we then defined the reference u_* “in terms of the wall shear stress that would exist if the wave section were replaced by a flat section,” and we recorded it just ahead of the rippled surface. The right inset in Fig. 4.2 shows that the ratio $A_t \equiv u_*/U$ is a constant, which we list in Table 4.1. As the same inset shows, the aerodynamic roughness ξ_0 conformed to $\ln(\rho u_* \xi_0/\mu) = -2.45 \pm 0.61$, where $\rho \simeq 1.2\,\mathrm{kg/m^3}$ and $\mu \simeq 1.8\ 10^{-5}\,\mathrm{kg/m.s}$ are, respectively, the density and dynamic viscosity of air. The corresponding values ($0.4 < \xi_0 < 11\,\mu\mathrm{m}$) are similar to a typical sand surface. We conducted experiments at conditions summarized in Table 4.1.

4.3 Data reduction

In turbulent boundary layers, pressure fluctuates as bursts with a spectrum of frequencies f [222]. Bursts of typical size $\ell_b \sim 100\mu/(\rho u_*)$ [122] produce fluctuations at $f \sim u_*/\ell_b = \rho U^2 A_t^2/(100\mu)$. For our experiments with $3 < U < 36\,\mathrm{m/s}$, we estimate $10\,\mathrm{Hz} \lesssim f \lesssim 1.5\,\mathrm{kHz}$. At these relatively low frequencies, it is not necessary to add the inertial terms $[\rho/(1-\nu_G)]\partial v/\partial t$ or $[\rho/(1-\nu_G)]v\partial v/\partial x$ to Darcy's law

$$\nabla p = -\frac{\mu}{K}\mathbf{v}, \tag{4.3}$$

since these terms scale, respectively, as $\rho f v$ and $\rho v^2 h_0/\lambda^2$, both of which are negligible compared with $\mu v/K$. In Eq. (4.3), $\mathbf{v}$, v, p and K are, respectively, seepage superficial velocity and its magnitude, pore pressure, and bed permeability. For nearly incompressible air, the mass conservation Eq.

$$\frac{\partial \rho}{\partial t} + \nabla \cdot (\rho \mathbf{v}) = 0 \tag{4.4}$$

adopts the divergence-free form $\nabla \cdot \mathbf{v} = 0$. With Eq. (4.3), the time-averaged pore pressure p then satisfies the Laplace Eq.

$$\nabla^2 p = 0. \tag{4.5}$$

However, while a steady pressure p can propagate through the bed according to the elliptic Eq. (4.5), [138] showed in their Appendix C that pressure fluctuations p' are attenuated in an isothermal porous medium according to

$$\frac{\partial p'}{\partial t} - \frac{K p_0}{\mu}\nabla^2 p' \simeq 0. \tag{4.6}$$

In our case, p is close to the ambient atmospheric pressure p_0. A solution of this Eq. shows that pressure fluctuations of frequency f decay exponentially with distance from the surface on a characteristic "acoustic depth"

$$h_d = \sqrt{\frac{K p_0}{\pi \mu f}}. \tag{4.7}$$

From Eq. (4.7), pressure bursts then induce pore pressure fluctuations down to an acoustic depth $h_d \sim D_d/U$, where $D_d \equiv [100 K p_0/(\pi A_t^2 \rho)]^{1/2}$ has units of a diffusion coefficient. For conditions that we explored, acoustic depths vary from $7\,\mathrm{mm}$ at the highest speed to $80\,\mathrm{mm}$ at the lowest. Equivalently, at $y \simeq H$, the boxes with $h_0/\lambda = 3\%$ and 6% experienced surface pressure fluctuations up to frequencies $f_d \lesssim 58\,\mathrm{Hz}$ and $\lesssim 35\,\mathrm{Hz}$, respectively, while faster fluctuations were damped by the porous medium. Conversely, these boxes were brought to the mean static pressure along the free surface in a relatively small time $\sim (2\pi f_d)^{-1} \simeq 3\,\mathrm{ms}$ and $\simeq 5\,\mathrm{ms}$.

In short, because the Laplace Eq. (4.5) is linear, time-averaged pore pressures can be reliably measured within permeable ripples in the wind tunnel. However, pressure fluctuations are naturally low-pass filtered by the porous medium through Eq. (4.6).

As Fourrière et al. [74] showed, the time-averaged surface pressure on a sinusoidal ripple with elevation in Eq. (4.1) and relatively low h_0/λ evolves along x as

$$p \simeq p_a + p_1 \cos(2\pi x/\lambda + \phi_1), \tag{4.8}$$

where p_1 scales as $\rho u_*^2 (h_0/\lambda)$ and $\phi_1 < 0$ is a small phase lag that Kendall [119] and Zilker and Hanratty [231] observed in experiments. In Eq. (4.8), the base pressure $p_a = p_0 + \tau_{zz}$ arises from a fluctuating turbulent normal stress $\tau_{zz} \simeq \rho u_*^2 \chi^2/3$, where $\chi \sim 3$ is a phenomenological constant [74].

By imposing Eq. (4.8) at the surface and the uniform ambient pressure $p = p_0$

on the ceiling of the box at $y = H$, integrating the Laplace Eq. (4.5) yielded the pore "gauge" pressure field

$$p - p_0 = (p_a - p_0)\left(1 - \frac{y}{H}\right) + \\ p_1 \cos(2\pi x/\lambda + \phi_1) \times \\ \left[\frac{\exp(-2\pi y/\lambda) - \exp(-4\pi H/\lambda)\exp(2\pi y/\lambda)}{1 - \exp(-4\pi H/\lambda)}\right]. \tag{4.9}$$

Our measurements provided $p - p_0$ at several x and y within the porous ripple. If surface pressure conforms to the single harmonic in Eq. (4.8), then Eq. (4.9) allowed us to extract $(p_a - p_0)$, p_1 and ϕ_1. Such is the case for the relatively low $h_0/\lambda = 3\%$ in the next section. However, at larger h_0/λ, we will later see that more harmonics are needed.

4.4 Pore pressure at low $h_0/\lambda = 3\%$

To estimate dust penetration into a rippled sand surface conforming to Eq. (4.1), Louge et al. [136] borrowed results from Gong et al. [85], who measured static pressure along a turbulent flow on impermeable smooth and rough wavy surfaces. To calculate pore pressure within a porous sand bed in closed form, they assumed that the data of Gong et al. [85] for a smooth undulating surface conformed to Eq. (4.8). In the Jackson and Hunt [114] theory for turbulent flow over slanted terrain, the surface shear stress scales with the aeolian kinetic energy density $\propto \rho U^2$ and roughly with slope, which, for ripples, grows with h_0/λ. Noting that, as a fluid normal stress, static pressure variations on a rippled surface follow the same scaling [73], [137] suggested that the pressure amplitude measured by Gong et al. [85] could be approximated with the expression

$$p_1 \approx \rho U^2 h_0/(\eta\lambda). \tag{4.10}$$

(An interpretation of the constant η is that p_1 is the static pressure amplitude that would arise in an ideal steady, incompressible, inviscid and irrotational flow on a sinusoidal surface located at a distance $\eta\lambda$ below a parallel flat wall).

The scaling in Eq. (4.10) suggests that pressure can be made dimensionless with

$$p^* \equiv \frac{p\lambda}{\rho U^2 h_0}. \tag{4.11}$$

If this scaling has merit, then the average value of p_1^* over experiments at different wind speeds, denoted by an overbar, should be equal to the inverse of the constant η that Louge et al. [137] introduced, $\bar{p}_1^* = 1/\eta$.

To gauge whether data for the rippled bed of low amplitude $h_0/\lambda = 3\%$ may be fit with Eq. (4.9), we separated variations along the streamwise and depth directions by defining the eigenfunctions

$$g_i(y/\lambda) \equiv \left[\frac{\exp(-2\pi i y/\lambda) - \exp(-4\pi i H/\lambda)\exp(2\pi i y/\lambda)}{1 - \exp(-4\pi i H/\lambda)}\right] \tag{4.12}$$

and

$$f_i(x/\lambda) \equiv \cos(2\pi i x/\lambda + \phi_i). \tag{4.13}$$

As Fig. 4.3 shows, pressure data at low h_0/λ is well represented by a single eigenfunction $(i = 1)$. Here, it is convenient to plot $(p - p_a)/[p_1 g_1(y/\lambda)]$ to highlight variations along the streamwise direction x, and $(p - p_a)/[p_1 f_1(x/\lambda)]$ to highlight the corresponding pore pressure decay along the depth y. This approach is equivalent to least-squares fitting the 2D data along (x, y) to Eq. (4.9), which represents a truncation of the Fourier series solution of Eq. (4.5) to its harmonic fundamental. We found that including higher harmonics for $h_0/\lambda = 3\%$

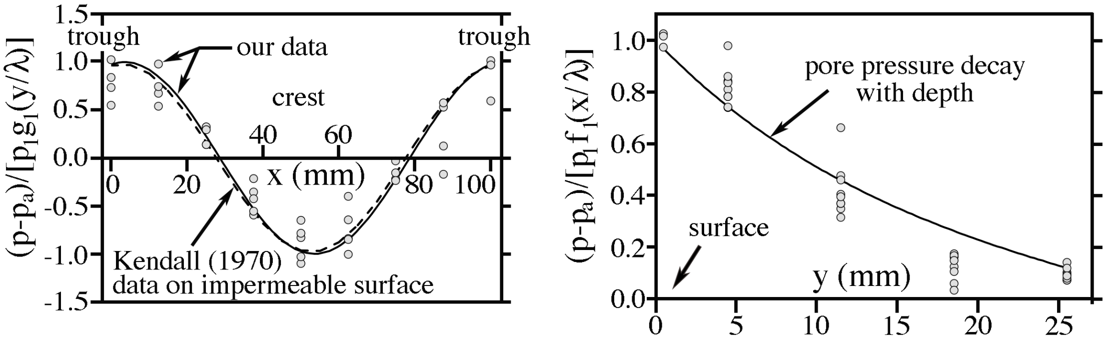

Figure 4.3: Pressure variations in a porous ripple of amplitude $h_0 = 3\,\mathrm{mm}$ and wavelength $\lambda = 100\,\mathrm{mm}$ swept by wind of bulk speed $U \simeq 9.1\,\mathrm{m/s}$. Left: Streamwise variations of the relative pore pressure $(p - p_a)/p_1$, divided by the function $g_1(y/\lambda)$ in Eq. (4.12) capturing variations in the depth. The dashed line is a fit through comparable data of Kendall [119] for an impermeable surface with similar $h_0/\lambda = 3.125\%$. With $U \simeq 10.6\,\mathrm{m/s}$, $\zeta_0 \simeq 4.10^{-4}$, and $u_*/U \simeq 0.024$, Kendall [119] found $p_1^* = 1.995 \pm 0.029$ and $\phi_1 = -0.169 \pm 0.015$ at 95% confidence, a result nearly identical to values in Table 4.1. Right: Variations of relative pore pressure divided by the function $f_1(x/\lambda)$ in Eq. (4.13) capturing streamwise variations. Points are data and lines are Eq. (4.9) with $p_a = 0.37\,\mathrm{Pa}$, $p_1 = 6.73\,\mathrm{Pa}$, and $\phi = -0.22\,\mathrm{rad}$.

did not improve the least-squares fit, as measured by the adjusted R-Squared criterion [63].

Thus, for $h_0/\lambda = 3\%$, we extracted $\eta = 1/\bar{p}_1^* \simeq 0.46 \pm 0.03$ from Eq. (4.10). As the dashed line in Fig. 4.3 shows, an extrapolation of our pore pressure measurements to the surface is nearly identical to the pressure data reported by Kendall [119] for an impermeable ripple of comparable wind speed and aspect ratio. Therefore, it appears that permeability similar to a typical sand hardly affects pressure variations on ripple surfaces of low h_0/λ. Later, section 4.6 will suggest why this is the case.

Synthesizing data from their own experiments and those of others, Gong et al. [85] had estimated $\eta \simeq 0.14$ and $\simeq 0.51$ for smooth and rough surfaces with $\xi_0 = 30\,\mu\mathrm{m}$ and $400\,\mu\mathrm{m}$, respectively. Inspired by those measurements and conscious of the relatively small aerodynamic roughness of desert sands [43], Louge et al. [137] and Louge et al. [136] adopted the "smooth" value of η that Gong et al. [85] had proposed. However, as the next section shows, this choice was not wise, largely because Gong et al. [85] conducted their measurements on ripples with higher aspect ratio, which are more likely to induce flow separation. Thus, our results show that Louge et al. [136] overestimated pore pressure amplitudes by a factor $\simeq 3$, and seepage-induced dust capture and moisture channeling by the same factor. Nonetheless, this mechanism of dust capture remains significant, and is now quantified.

Our data also show that, like over impermeable walls, surface pressure on a porous sinusoidal bed at $h_0/\lambda = 3\%$ (Eq. 4.1, with y pointing downward) is sinusoidal with a slight phase lag. Kuzan et al. [127] drew a phase diagram delimiting regimes of attached and separated flows over impermeable sine waves (Fig. 4.4). At the wind speeds of our experiments, this map suggests that flows are attached to the surface with $h_0/\lambda = 3\%$, except perhaps for the two smallest speeds that we staged, shown as the rightmost two diamond symbols in Fig. 4.4 with $U \simeq 4.4$ and $9.1\,\mathrm{m/s}$. In fact, Fig. 4.3 hints that such flow separation might have indeed occurred at $U \simeq 9.1\,\mathrm{m/s}$. For an attached turbulent boundary layer, pressure fluctuations are approximately $p' \sim 3\rho u_*^2$ [104]. Thus, relative to p_1, they are $p'/p_1 \sim (3A_t^2/\bar{p}_1^*)(\lambda/h_0)$, where $A_t \equiv u_*/U \simeq 0.04$ and $\bar{p}_1^* \simeq 2$ (Table 4.1), or $p'/p_1 \simeq 8\%$. There are regions along the ripple where pressure deviations exceed this estimate, particularly just after the crest ($x \simeq 60\,\mathrm{mm}$).

Because pressure amplitude scales with h_0/λ, ripples of lower aspect ratio (i.e. ripple index > 17) should also exhibit a similar, slightly delayed sinusoidal surface pressure, and their flow should be even less likely to separate. In con-

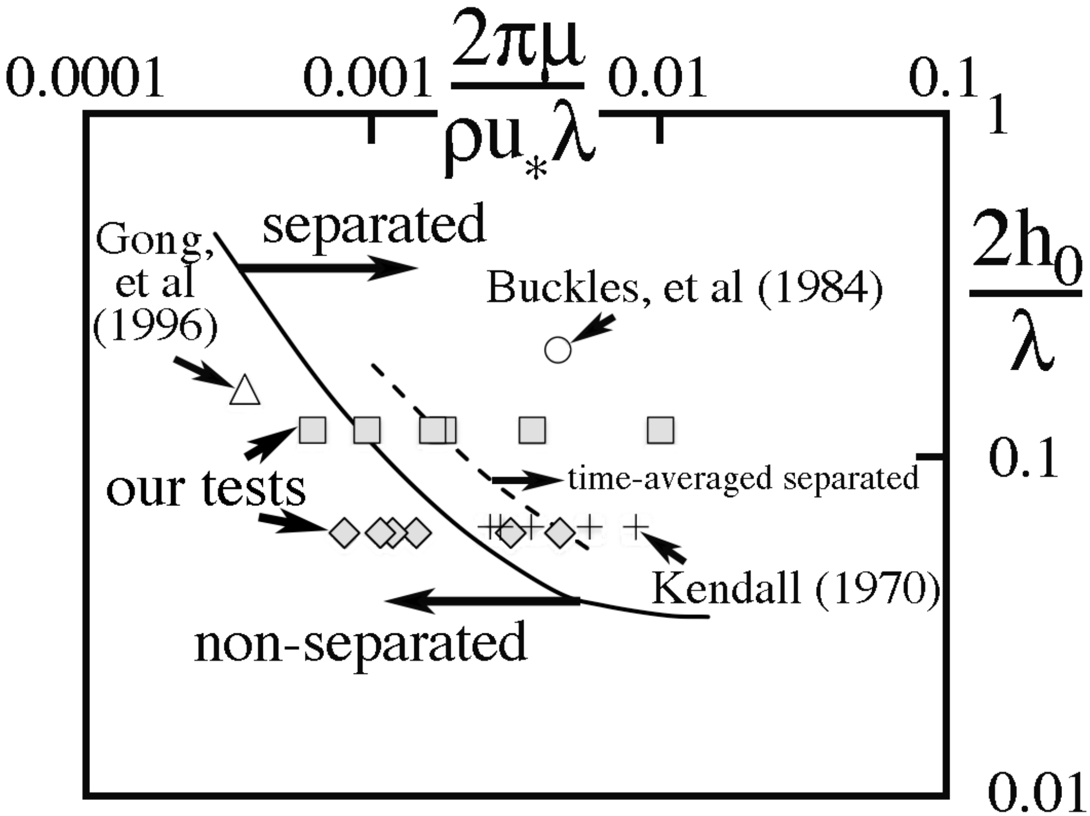

Figure 4.4: Regime map proposed by Kuzan et al. [127] for turbulent flows over sinusoidal impermeable ripples [78]. Solid lines delimit regions in the diagram of inverted Reynolds number $2\pi\mu/(\rho u_* \lambda)$ vs. ripple aspect ratio $2h_0/\lambda$, behaving as "separated" or "non-separated" flows [207]. To the right of the dashed line, Kuzan et al. [127] noted a transition to "time-averaged separated" flows remaining detached on longer time scales. The solid triangle marks experiments of Gong et al. [85]; the filled circle shows experiments of Buckles et al. [34], which [98] modeled with LES; plus signs are experiments of Kendall [119]; solid diamonds and squares indicate our own tests with $h_0/\lambda = 3\%$ and 6%, respectively.

trast, as h_0/λ grows (i.e., for lower ripple index), Fig. 4.4 suggests that the flow is more prone to detachment, and therefore our measurements at low aspect ratio are no longer sufficient to expose how the porous subsurface affects the turbulent flow. In fact, static pressure variations along the impermeable sinusoidal surface of Gong et al. [85] with $h_0/\lambda \simeq 7.9\%$ did not, strictly speaking, conform to the harmonic Eq. (4.8). Conscious of this shortcoming, we therefore staged a larger $h_0/\lambda = 6\%$ for comparison, as discussed next.

4.5 Pore pressure at $h_0/\lambda = 6\%$

Because turbulent flows over waves of large amplitude separate [127], we could no longer model pore pressure within artificial ripples of $h_0/\lambda = 6\%$ with a single harmonic. Instead, we found it necessary to interpret data using a longer series of eigenfunctions satisfying the boundary condition at $y = H$. We truncated the series to the third harmonic, beyond which we observed no further improvement in the R-Squared criterion that gauges confidence in the best fit,

$$p - p_0 = (p_a - p_0)\left(1 - \frac{y}{H}\right) + \sum_{i=1}^{3} p_i f_i(x/\lambda) g_i(y/\lambda) + p_d f_{1/n}(x/\lambda) g_{1/n}(y/\lambda). \tag{4.14}$$

To this series we added the last term $p_d f_{1/n} g_{1/n}$ representing the relatively small decay in mean static pressure that wind experiences on length scales $\gg \lambda$ as it drags the rippled surface. For compatibility with the Laplace Eq. (4.5), this "drag" term is a single slowly-varying sub-harmonic eigenfunction valid in the range $0 < x < \lambda$ of the form $f_{1/n}(x/\lambda) \equiv \cos[2\pi x/n\lambda + \phi_d]$ and $g_{1/n}(y/\lambda) \equiv [\exp(-2\pi y/n\lambda) - \exp(-4\pi H/n\lambda)\exp(2\pi y/n\lambda)]/[1 - \exp(-4\pi H/n\lambda)]$, which we obtain by substituting $i = 1/n$ in Eqs. (4.12) and (4.13). Because such drag-induced pressure reduction is small, the actual form of the subharmonic term $p_d f_{1/n} g_{1/n}$ matters little to our results. Values of n and p_d are found in Table 4.1.

As Fig. 4.4 shows, the more complicated form of pore pressure in Eq. (4.14) is consistent with the regime map that Kuzan et al. [127] drew for harmonically-rippled impermeable surfaces. This map implies that most of our tests at

$h_0/\lambda = 6\%$ separated behind crests, while those at $h_0/\lambda = 3\%$ did not. Despite a lower value of inverted Reynolds number $2\pi\mu/(\rho u_*\lambda)$, the experiments of Gong et al. [85] at $h_0/\lambda \simeq 7.9\%$ should not have separated either, according to this map. However, as Fig. 4.5 illustrates, surface pressures of Gong et al. [85] closely resemble those of Buckles et al. [34] and Henn and Sykes [98], suggesting that they too exhibited separated flow.

Further evidence of flow recirculation behind crests is the relatively low pressure recorded on impermeable surfaces in the range $0.7 \lesssim x/\lambda \lesssim 1$ and the delayed location of peak pressure. Unlike surface pressure profiles at $h_0/\lambda = 3\%$ (Fig. 4.3 left, with $y \sim 0$), peak pressures at larger h_0/λ in Fig. 4.5 are not located above troughs, but they are delayed to $x/\lambda \sim 0.25$ for impermeable surfaces (symbols) or to $x/\lambda \sim 0.16$ over our porous bed (solid line).

Finally, by comparing pressure data from wavy surfaces with different values of h_0/λ, Fig. 4.5 confirms that, like shear stress or u_*^2 [114], pressure scales with h_0/λ. However, as the inset of Fig. 4.5 reveals, there is a subtle dependence of the principal pressure harmonic p_1^* from Eq. (4.14) on wind speed.

More significantly, our extrapolation of pore pressure to the surface (solid line in Fig. 4.5) clearly deviates from similar measurements on impermeable surfaces. In the next section, we suggest why these deviations can be attributed to the porous medium.

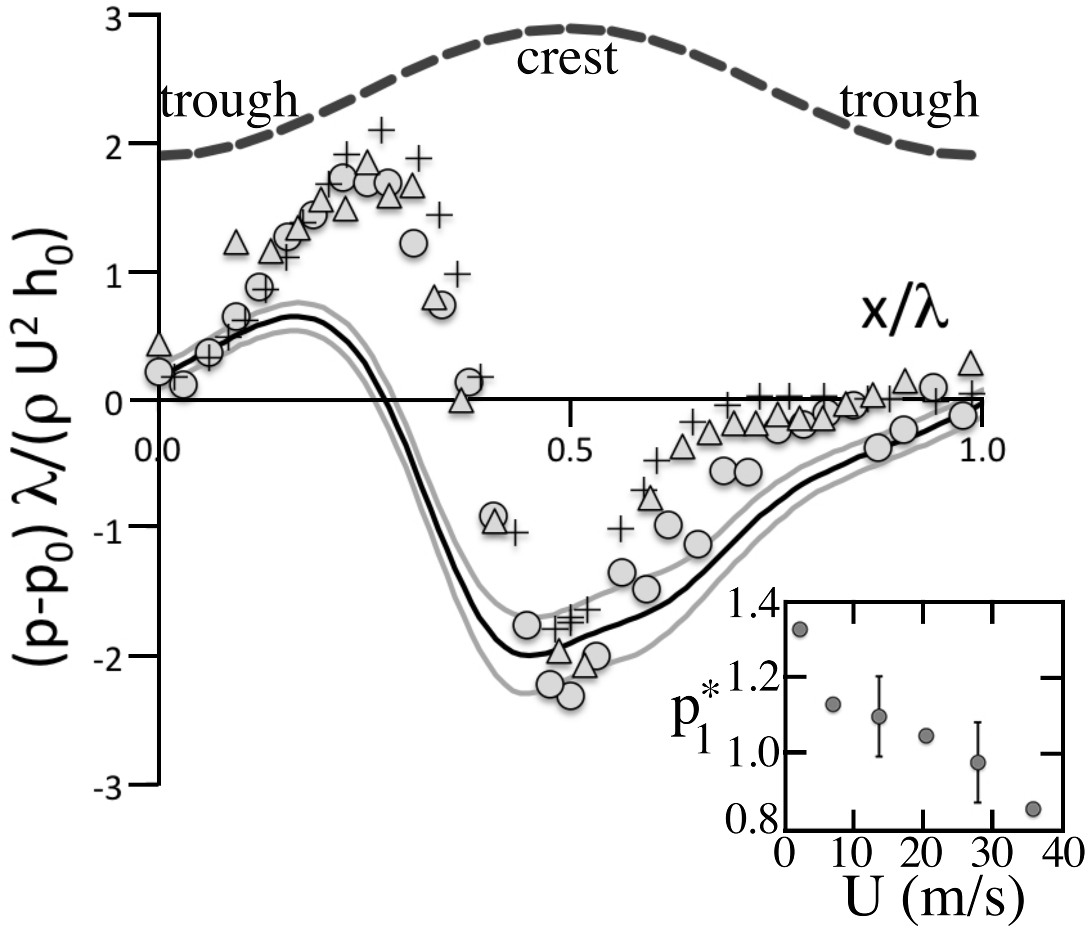

Figure 4.5: Comparison of static pressure on impermeable and porous surfaces. Symbols mark measurements on impermable solids by, respectively, Buckles et al. [34] (circles) and Gong et al. [85] (triangles, their "rough" surface), and computed in Large-Eddy-Simulations labelled "BHA1" by Henn and Sykes [98] (plus signs). The solid line is an extrapolation of measurements within our porous bed with $h_0/\lambda = 6\%$ to the surface using Eq. (4.14) (solid line), based on parameters in Table 4.1. Grey lines demarcate our 95% confidence interval. The abscissa is x/λ with origin over the trough; the ordinate is $(p^* - p_0^*)$. The upper sketch (exaggerated amplitude) shows positions of trough and crest. The inset shows variations of the main harmonic in Eq. (4.14) vs U with error bar from Table 4.1.

4.6 Significance for turbulent flows over porous rippled surfaces

Besides closely capturing pore pressure within the rippled bed, Eq. (4.14) provides an accurate record of static pressure on its surface, shown as the solid line in Fig. 4.5. Using a Monte-Carlo technique, we calculated where this line resides at 95% confidence. As Fig. 4.5 reveals, the dimensionless surface pressure at the porous crest with $h_0/\lambda = 6\%$ is identical within experimental errors to earlier measurements [34, 85] and numerical simulations [98] on impermeable wavy surfaces of similar aspect ratios, thus validating our measurements and suggesting that the scaling of pressure in Eq. (4.11) is robust. However, we find that surface pressure and its gradient in the region $0.1 \lesssim x/\lambda \lesssim 0.45$ between trough and crest are substantially lower on the porous ripple than they are on a similar impermeable surface.

This contrast between pressure profiles on impermeable and porous wavy surfaces suggests that the porous medium interferes with the turbulent flow overhead. At a porous surface of upward unit normal $\hat{\mathbf{n}}$, Beavers and Joseph [19] recorded a substantial slip velocity $\mathbf{u}_s$, which they related to the superficial velocity $\mathbf{v}$ in the bed through a boundary condition that Jones [116] later interpreted in terms of the surface shear stress τ [156]. In a clear-gas turbulent viscous sublayer, this condition writes

$$\tau \cdot \hat{\mathbf{n}} = \frac{\varpi \mu}{K^{1/2}} \left(\mathbf{u}_s - \mathbf{v} \right), \tag{4.15}$$

where ϖ is a constant of order unity. (As Saffman [182] pointed out, the superficial velocity of order K is small compared with the slip of order $K^{1/2}$, and thus it can be neglected).

Meanwhile, as Durán and Herrmann [52] explained, the "outer layer" far above a rippled surface of moderate h_0/λ behaves as a nearly inviscid potential flow having streamlines in phase with ripple elevation and a peak velocity located above crests. Closer to the surface, Reynolds stresses in the turbulent "inner layer" delay the response of fluid velocity to an imposed shear, thus compelling wall shear stress to peak ahead of crests and pressure maxima to lag behind troughs. Fourrière et al. [74] showed that the inner layer thickness ℓ satisfies $\ell/\lambda \sim \ln^{-2}(\ell/\xi_0)$. Closer to the surface, the viscous sublayer defines the aerodynamic roughness ξ_0 that the inner layer experiences. As long as the thickness of the viscous sublayer $\ell_v \simeq 5\mu/(\rho u_*)$ is small compared to that of the inner layer, then details of how aerodynamic roughness arises do not matter to the evolution of shear stress and pressure along the ripple. For our conditions, $1.5 < \ell < 3.1\,\mathrm{mm}$ is substantially larger than $59 < \ell_v < 400\,\mu\mathrm{m}$, but much smaller than λ, therefore validating the assumptions underlying the analysis of Fourrière et al. [74].

With these assumptions, Kroy et al. [126] extended the theory of Jackson and Hunt [114] for turbulent flows over topography to dunes and ripples. They showed that shear stress on a sinusoidal surface of moderate h_0/λ evolves as

$$\tau = \rho u_*^2 \left(1 - \hat{\tau}\right), \tag{4.16}$$

where $\phi_\tau = \arctan(B/A)$ and

$$\hat{\tau} \equiv 2\pi \left(\frac{h_0}{\lambda}\right) (A^2 + B^2)^{1/2} \cos\left(2\pi \frac{x}{\lambda} + \phi_\tau\right) \tag{4.17}$$

is a dimensionless excursion in shear stress. To a good approximation, Fourrière et al. [74] calculated

$$A \simeq 2 + \frac{a_1 + a_2 R + a_3 R^2 + a_4 R^3}{1 + a_5 R^2 + a_6 R^4} > 0, \tag{4.18}$$

$$B \simeq \frac{b_1 + b_2 R + b_3 R^2 + b_4 R^3}{1 + b_5 R^2 + b_6 R^4} > 0, \tag{4.19}$$

where $a_i \simeq (1.070, 0.0931, 0.108, 0.0248, 0.0416, 0.00106)$ and $b_i \simeq (0.0370, 0.158, 0.115, 0.00202, 0.00287, 0.000535)$. The dimensionless constants A and B are weakly related to the aerodynamic roughness ξ_0 through

$$R \equiv -\ln\left(\frac{\xi_0}{\lambda}\right) > 0. \tag{4.20}$$

Combining Eq. (4.15) with $v \simeq 0$ and Eq. (4.16), the ratio of slip to shear velocity is then

$$\frac{u_s}{u_*} \simeq \mathrm{Re}_K \left(1 - \hat{\tau}\right)/\varpi \tag{4.21}$$

where $\mathrm{Re}_K \equiv \rho u_* \sqrt{K}/\mu$. If for simplicity we assume that, at low h_0/λ, Prandtl's logarithmic law applies to the inner layer, then the velocity profile becomes $u = (u_*/\kappa)\ln(z/\xi_0) + u_s$ or, equivalently, $u = (u_*/\kappa)\ln(z/\xi_s)$, where ξ_s is an effective "slip roughness" that varies along the surface,

$$\xi_s \equiv \xi_0 \exp\left(-\frac{u_s \kappa}{u_*}\right) = \xi_0 \exp\left[-\frac{\kappa}{\varpi}\mathrm{Re}_K(1-\hat{\tau})\right]. \tag{4.22}$$

At low enough h_0/λ, $\hat{\tau} < 1$, so that the slip roughness ξ_s decreases everywhere sharply with wind speed.

As Manes et al. [140, 141] showed for flat beds of much higher permeability ($K \simeq 10^{-8} - 10^{-7}\mathrm{m}^2$), turbulence can also penetrate a permeable porous substrate, thus further perturbing the turbulent boundary layer, for example by reducing the apparent von Kármán constant κ as Re_K grows. However, the data of Manes et al. [140, 141] imply that these more dramatic effects disappear at the lower permeabilities typical of desert sands, where Re_K remains small.

Nonetheless, Eq. (4.21) suggests that a significant slip velocity can arise on a porous rippled surface. For example, with typical $A \simeq 4$ and $B \simeq 2$ at

$u_* = 0.3\,\mathrm{m/s}$, Eqs. (4.17) and (4.21) predict that our porous rig with $h_0/\lambda = 6\%$ and $K = 3.4\,10^{-11}\,\mathrm{m}^2$ can produce a peak slip $u_s/u_* \simeq 0.3$ that is a notable fraction of the shear velocity. Meanwhile, for the same conditions, the slip is much smaller on a flat surface ($h_0/\lambda = 0$), $u_s/u_* \simeq 0.1$. The form of Eq. (4.21) suggests that the rippled nature of the porous surface begins to produce a significant slip when the amplitude of $\hat{\tau}$ in Eq. (4.17) exceeds 1 or, equivalently, for aspect ratios $h_0/\lambda > 1/[2\pi(A^2 + B^2)^{1/2}]$. With typical values $A \simeq 4$ and $B \simeq 2$ [74], this occurs with $h_0/\lambda \gtrsim 4\%$, suggesting that the shallow ripples in section 4.4 possess a nearly uniform slip roughness $\xi_s \sim \xi_0 \exp{(-\kappa \mathrm{Re}_K/\varpi)}$. However, as h_0/λ grows to 6%, the slip should vary significantly anywhere along the ripple, unless surface shear stress collapses through flow separation.

In other words, as far as surface pressure is concerned, a porous ripple at $h_0/\lambda = 3\%$ should behave as an impermeable ripple with uniform, albeit smaller aerodynamic "slip" roughness. However, for greater h_0/λ, the slip roughness should evolve along porous ripples, thus modifying the character of the turbulent boundary layer.

Nonetheless, the reduction in slip roughness with u_* that is predicted by Eq. (4.22) seems at odds with the results of Gong et al. [85]. At relatively large values of $h_0/\lambda = 7.9\%$, these authors observed a *larger* pressure amplitude on a *smooth* impermeable sinusoidal surface with $\xi_0 = 30\,\mu\mathrm{m}$, than on a rougher surface with $\xi_0 = 400\,\mu\mathrm{m}$. Meanwhile, our plastic surfaces with $h_0/\lambda = 6\%$ have an aerodynamic roughness $0.4 < \xi_0 < 11\,\mu\mathrm{m}$ comparable to the smooth case of Gong et al. [85]. (Moreover, as Eq. (4.22) suggests, our porous ripples should produce a even smaller effective roughness by allowing slip at the wall). Therefore, based upon trends that Gong et al. [85] observed for the variations of pressure amplitude with aerodynamic roughness, our smoother porous ripples with $h_0/\lambda = 6\%$ should have produced a *larger* dimensionless pressure amplitude p^* than what Gong et al. [85], Buckles et al. [34] or Henn and Sykes [98] measured on impermeable ripples. Yet the opposite happened: as Fig. 4.5 shows, surface pressure variations declined from impermeable to porous ripples; further, as the inset of that Fig. shows, the first pressure harmonic p_1^* decreased with wind speed.

Therefore, another mechanism that is absent from impermeable experiments must be at play when h_0/λ is relatively large. Our observations suggest that porous ripples allow air to bypass the main flow. Because pore pressure satisfies the elliptic Laplace Eq. (4.5), the depression at the crest diffuses through the porous bed, thus substantially reducing surface pressure upstream. (Less noticeably, the depression also permeates leeward, producing a lower surface pressure in the range $0.6 \lesssim x/\lambda \lesssim 1$ than the corresponding value on an impermeable surface). Our measurements suggest that it does not take much air "seepage" to create an internal bypass attenuating the peak pressure through such retro-diffusion of the depression on the crest. An attenuation Δp^* across the dimensionless distance Δx^* requires a seepage velocity v given by Eq. (4.3) as

$$\frac{v}{U} \sim \left(\frac{\Delta p^*}{\Delta x^*}\right)\left(\frac{\rho K^{1/2} U}{\mu}\right)\left(\frac{h_0}{\lambda}\right)\left(\frac{K^{1/2}}{\lambda}\right) \tag{4.23}$$

For example, as Fig. 4.5 shows, the drop $\Delta p^* \simeq 1.2$ across $\Delta x^* \simeq 0.25$ from peak pressure at $x^* \simeq 0.25$ to crest depression at $x^* \simeq 0.5$ only requires a seepage velocity as small as $v \simeq 0.5\,\mathrm{mm/s}$ for $U = 10\,\mathrm{m/s}$. However, because seepage velocity scales as $K^{1/2}/\lambda$ in Eq. (4.23), an internal bypass that can attenuate surface pressure on the ripple scale is not important on the size of a dune, which has vanishingly small $K^{1/2}/\lambda$.

Because the principal ingredient in the theory of Jackson and Hunt [114] is local slope, represented in our sinusoidal case by h_0/λ, we expect that any porous bed with similar size and slope, such as triangular aeolian ripples [205], will create comparable slip roughness and attenuate surface pressure gradients in ways that are analogous to a sinusoidal profile. The recent experiments of [27] confirm this with coarse gravel beds. In their case, particles are so large that permeability is high, thus creating a visible fluid bypass through the bed.

Because by necessity our experiments were run without particles, they only applied, strictly speaking, to winds below the suspension threshold. However, we anticipate that our artificial rippled surfaces capture effects of porosity on surface slip and streamwise wind pressure gradient, whether or not the wind is laden with particles, for three reasons. First, our porous plastic has comparable $\sqrt{K} \simeq 5.8\,\mu\mathrm{m}$ to a typical sand bed ($\sqrt{K} \simeq 2\,\mu\mathrm{m}$). Second, because ripples travel at a speed $\ll u_*$, seepage is established much faster than ripple shape changes. Third, as Bagnold [15] noted, the momentum exchange between air and suspended solids binds altitude z_B and speed u_B at the top of the saltation layer. (For this reason, z_B is called the "Bagnold focal point"). Therefore, consistent with Prandtl's law of the wall, the particle-laden region presents to the turbulent inner layer aloft an effective aerodynamic roughness [52]

$$\xi_B \equiv z_B \exp\left(-\frac{u_B \kappa}{u_*}\right). \tag{4.24}$$

As Sherman and Farrell [195] reviewed, $g\xi_B/u_{*\mathrm{th}}^2$ grows with shear velocity above the transport threshold $u_{*\mathrm{th}}$ (in contrast with the slip roughness ξ_s that we introduced in Eq. (4.22), which instead decreases with wind speed). Because the coefficients in Eqs. (4.18)–(4.20) depend logarithmically on ξ_s, they change slowly. Meanwhile, to predict the streamwise evolution of surface pressure, Fourrière [73] derived other coefficients (called C and D) with similarly weak logarithmic dependence on roughness. Therefore, we expect that pore pressure evolution is qualitatively similar with or without sand transport, as Fourrière et al. [74] noted for shear stress. However, because the theory of Jackson and Hunt [114] is predicated upon an inner layer that is thicker than the viscous sublayer, a saltation region with $z_B \sim u_{*\mathrm{th}}^2/g$ may become too thick to uphold the theory's principal assumption, and therefore it might no longer produce quantitative predictions of shear stress and pressure. In addition, because particles near the surface affect the suspension viscosity [148], the clear-gas boundary condition in Eq. (4.15) should be changed accordingly, and τ should be replaced by the gas contribution to the total stress. Nonetheless, our experiments provide a first insight toward appreciating the role of bed porosity on aeolian rippled surface processes in deserts.

4.7 Pressure drag and lift

At the wavy surface with unit normal of components $[2\pi h_0^* \sin(2\pi x^*); 1]/[1 + 4\pi^2 h_0^{*2} \sin^2(2\pi x^*)]^{1/2}$ along x and y, pressure integrates to a force $\mathbf{P}$ exerted on a unit ripple width over the whole wavelength. Its projection along the flow amounts to a pressure drag force per unit width, expressed in dimensionless form as

$$P_x^* \equiv \frac{1}{\lambda} \frac{\mathbf{P} \cdot \hat{\mathbf{x}}}{\rho U^2} \left(\frac{\lambda}{h_0} \right) = \tag{4.25}$$

$$\int_0^1 (p^* - p_0^*) \frac{2\pi h_0^* \sin(2\pi x^*)}{[1 + 4\pi^2 h_0^{*2} \sin^2(2\pi x^*)]^{1/2}} \mathrm{d}x^*,$$

while its projection along y resembles a lift

$$P_y^* \equiv \frac{1}{\lambda}\frac{\mathbf{P}\cdot\hat{\mathbf{y}}}{\rho U^2}\left(\frac{\lambda}{h_0}\right) \tag{4.26}$$
$$= \int_0^1 (p^* - p_0^*)\frac{\mathrm{d}x^*}{[1+4\pi^2 h_0^{*2}\sin^2(2\pi x^*)]^{1/2}}.$$

In these expressions, distances are made dimensionless with λ and denoted by an asterisk. As Table 4.1 shows, the dimensionless net pressure drag force grows roughly in proportion to h_0/λ, thus suggesting that $\mathbf{P}\cdot\hat{\mathbf{x}} \propto \rho U^2 h_0^2/\lambda$. It is significantly smaller than the same quantities derived from the surface pressure data of Gong et al. [85] ("smooth" surface, $P_x^* \simeq 0.25$; and "rough" surface, $P_x^* \simeq 0.18$ at $h_0/\lambda \simeq 7.9\%$), Buckles et al. [34] ($P_x^* \simeq 0.24$ at $h_0/\lambda \simeq 10\%$), and from the LES of [98] ($P_x^* \simeq 0.22$ at $h_0/\lambda \simeq 10\%$), confirming that air seepage through the porous medium reduces pressure drag on the ripple surface.

Our experiments also yielded $P_y^* < 0$, indicating that the ripple surface was subject to an upward lift. Comparison of $|P_y^*|$ for ripples with $h_0/\lambda = 6\%$ and 3% in Table 4.1 suggests that $|P_y^*| \propto h_0^{*2}$, tentatively suggesting a lift force $\mathbf{P}\cdot\hat{\mathbf{y}} \propto \rho U^2 h_0^3/\lambda^2$. In contrast, earlier experiments over impermeable wavy surfaces could be of either sign; the "rough" surface of Gong et al. [85] had $P_y^* \simeq 0.10$; their "smooth" one had $P_y^* \simeq -0.28$; Buckles et al. [34] had $P_y^* \simeq -0.15$, but the corresponding LES found $P_y^* \simeq +0.14$ [98].

Finally, as Table 4.1 shows, we noted that ripples of relatively large aspect ratio induce a net seepage updraft. Making superficial velocity v dimensionless as $v^* \equiv v[\mu\lambda^2/(K\rho U^2 h_0)]$, the net seepage (positive downward) calculated at $y = H$ is

$$v^* = -\int_0^1 \hat{\mathbf{y}}\cdot\nabla^* p^* \mathrm{d}x^*. \tag{4.27}$$

The mean updraft at $h_0/\lambda = 6\%$ suggests that porous ripples of high aspect

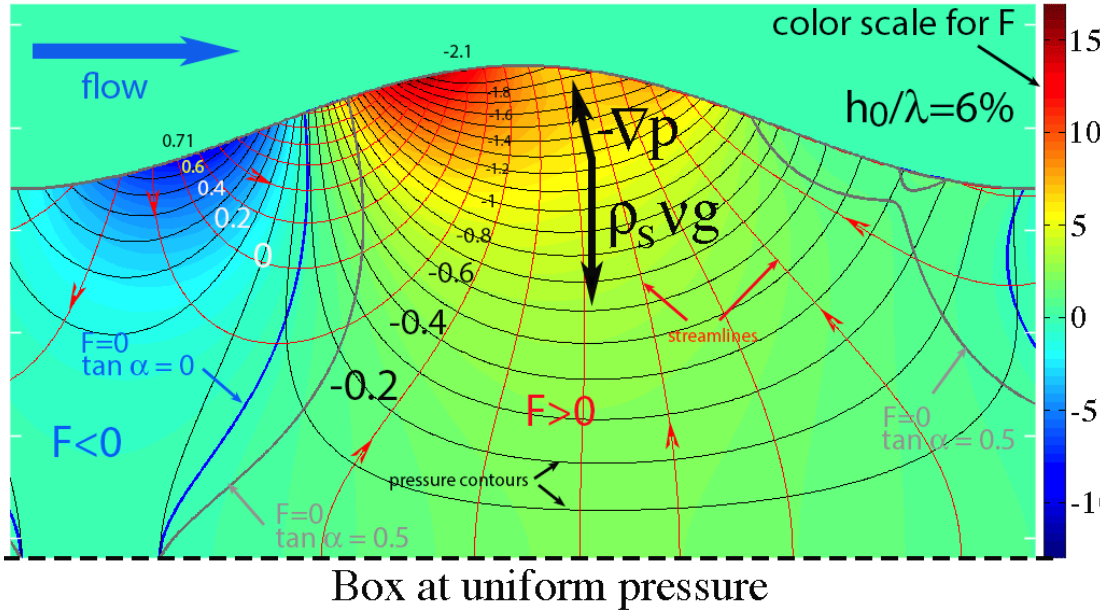

Figure 4.6: Contours of seepage streamlines and dimensionless gauge pore pressure $p^* - p_0^*$ across a section of the porous ripple with $h_0/\lambda = 6\%$, bounded on top by the harmonic ripple described in Eq. (4.1) and by a hermetic box with pressure p_a at $y = H = 42\,\mathrm{mm}$ below. Figure is drawn to-scale. Numerical values are reconstructed from Eq. (4.14) with dimensionless constants in Table 4.1. Red and black lines are, respectively, streamlines and contours of $p^* - p_0^*$ with values in the range $-2.1 < p^* - p_0^* < 0.71$. For a frictionless bed ($\tan\alpha = 0$), colors represent the magnitude of F in Eq. (4.30) with $-8.7 < F < 15.1$ and thick blue lines mark the locus of $F = 0$. The maximum $F_{\max} = 15.1$ is ahead of the crest at $x/\lambda \simeq 0.40$. Thick grey lines are the same locus for $\tan\alpha = 0.5$. Note that, because the term $\propto p_d$ in Eq. (4.14) dissipates pressure slightly from $x = 0$ to $x = \lambda$, patterns are aperiodic along x. Black arrows illustrate typical body forces exerted on a point within the porous ripple (not to-scale). In this sketch, the opposite of the pore pressure gradient $-\nabla p$ is not aligned with the gravitational body force $\rho_s \nu g$, but it contributes to relieving it.

ratio exhale a net amount of pore air as wind blows over their surface. At lower $h_0/\lambda = 3\%$, the draft is smaller and directed downward instead.

4.8 Body forces

We derive isobaric contours and seepage streamlines within the ripple from the two-dimensional fit of the pore pressure field in Eq. (4.14). They are sketched in Fig. 4.6 and 4.7. As Louge et al. [137] calculated in their Appendix A, the pore pressure gradient within a homogeneous porous sand bed exerts an equal and opposite body force $-\nabla p$ on the grain assembly. A frictionless bed with solid volume fraction ν and grains of material density ρ_s would therefore mobilize if the downward projection of this gradient $\hat{y} \cdot \nabla p$ balanced the gravitational body force $\rho_s \nu g$. If instead the bed failed as a Mohr-Coulomb material with internal friction, which nearly equals the tangent of the angle of repose α, then its local force balance would also involve the component of the gradient along $\hat{\mathbf{x}}$ [137]. In this case, grain mobilization would take place wherever

$$\frac{\partial p}{\partial y} - \tan\alpha \left| \frac{\partial p}{\partial x} \right| \geqslant \rho_s \nu g. \tag{4.28}$$

In criterion (4.28), the absolute value indicates that internal friction hinders the onset of mobilization by redirecting the body force $\partial p/\partial x$ to the downward vertical direction, whatever its sign. Tsinontides and Jackson [212] and Loezos et al. [135] elucidated a similar effect in gas-solid fluidized beds.

When sand ripples are buffeted by a strong wind, a pore pressure gradient directed downward can also relieve a substantial part of the bed weight below them, even without complete grain mobilization. On parts of the sand free surface where such downward gradient exists, the corresponding force can thus facilitate the onset of erosion. This contribution of pore pressure gradients is generally ignored, whereby grain ejection is thought to occur after u_* reaches a certain threshold, and subsequent erosion is entirely attributed to surface shear [196, 194]. Nonetheless, recent studies have shown that certain geophysical flow over a porous bed can develop static pressures below the mean ambient value, thus creating pore pressure gradients below the surface that affect flow dynamics [110, 179, 111, 138, 37].

In this section, we exploit our measurements to calculate the propensity of harmonic ripples to relieve gravity. From criterion (4.28), this is measured with the ratio

$$\mathbb{F} \equiv \frac{\partial p/\partial y - \tan\alpha |\partial p/\partial x|}{\rho_s \nu g}; \tag{4.29}$$

if $\mathbb{F} \geqslant 1$, then the bed is mobilized; if $0 < \mathbb{F} < 1$, gravity is partially relieved by pore pressure gradients, possibly leading to bed expansion [137]; if $\mathbb{F} < 0$, gravity is augmented by the gradients, perhaps contributing to bed compaction. To cast our results in more general terms, we define

$$F \equiv \frac{\partial p^*}{\partial y^*} - \tan\alpha \left| \frac{\partial p^*}{\partial x^*} \right|, \tag{4.30}$$

where distance is made dimensionless with wavelength, $(x^*, y^*) \equiv (x, y)/\lambda$, and p^* is given by Eq. (4.11). Then, the ratio in Eq. (4.29) becomes $\mathbb{F} = \mathbb{R}F$, where the dimensionless group

$$\mathbb{R} \equiv \frac{\rho U^2 h_0}{\rho_s \nu g \lambda^2} \tag{4.31}$$

has the structure of a Sleath number [197], and represents how wind kinetic energy counteracts the gravitational pull on a rippled sand bed. Louge et al. [137] introduced a similar dimensionless number governing rapid snow eruption as the front of a powder avalanche passes over a porous snow pack.

Equations (4.29)–(4.31) imply that, because $\mathbb{R}$ depends linearly on ripple amplitude but quadratically on wavelength, longer ripples are less susceptible to pore pressure gradients than smaller ones at a constant aspect ratio h_0/λ. If the flow did not separate behind crests at large aspect ratios h_0/λ, then we would

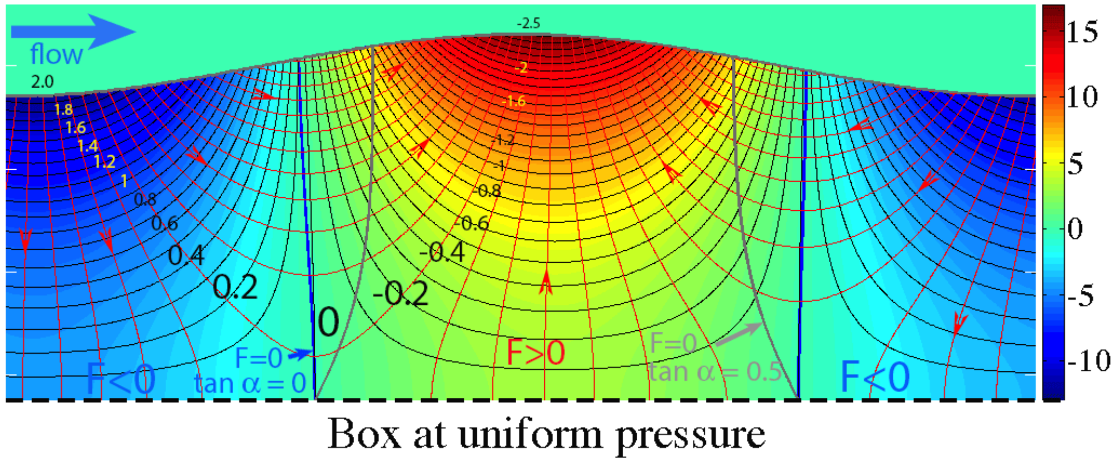

Figure 4.7: Cross-section of the porous ripple with $h_0/\lambda = 3\%$ and $H = 32.5\,\mathrm{mm}$. Figure is drawn to-scale. For the meaning of lines and color scale, see Fig. 4.6. Note the greater symmetry at this smaller aspect ratio. Ranges of $p^* - p_0^*$ and F are provided in Table 4.1. The maximum $F_{\max} = 16.7$ is behind the crest at $x/\lambda \simeq 0.53$.

expect F to remain roughly independent of wind speed, sand density, gravitational acceleration, ripple amplitude or wavelength, while the role of these quantities would be captured by $\mathbb{R}$. This is essentially what Gong et al. [85] suggested with the scaling in Eq. (4.10).

To gauge to what extent ripple aspect ratio matters, Figs. 4.6 and 4.7 contrast the distribution of F for $h_0/\lambda = 6\%$ and 3%. Here we calculate F by substituting average pressure coefficients ($\bar{p}_i^*$, $\bar{p}_a^*$, $\bar{p}_d^*$), phases ($\bar{\phi}_i$, ϕ_d) and index n from Table 4.1 in Eq. (4.14) and differentiating. As expected, F spans similar magnitudes for both aspect ratios (Table 4.1). If friction is introduced, the domain where pressure gradients relieve gravity ($F > 0$) becomes narrower. Although the maximum value of F decreases with increasing $\tan\alpha$, this reduction is small. For $\tan\alpha = 0.5$, $F_{\max} = 16.5$ at $h^* = 3\%$ and $F_{\max} = 13.8$ at $h^* = 6\%$.

Crucially, we find that, while porous ripples of low aspect ratio maintain a relatively symmetric seepage flow pattern (Fig. 4.7), ripples of a greater h_0/λ

possess a pressure field that is significantly skewed toward the upstream face (Fig. 4.6). Coincidentally, the greatest propensity for seepage to relieve gravity (i.e. where F peaks at F_{max}) lies approximately $(\lambda/10)$ ahead of the crest, where the theory of [114] also locates maximum shear stress. Thus, if ripples exhibit a large aspect ratio, it is possible for wind-induced grain mobilization to augment shear-induced erosion there.

To compare the relative importance of the two effects, we invoke the correlation of Shao and Lu [194] for the onset of aeolian transport at a threshold shear velocity $u_{*\text{th}}$. For cohesionless surface grains of diameter d, they wrote $\rho u_{*\text{th}}^2 \simeq A_N \rho_s g d$, where $A_N \simeq 0.0123$ is an empirical constant inspired by insights of Bagnold [14] and Shields [196]. For a typical turbulent boundary layer, the shear velocity u_* is related to U through $u_* = A_t U$. (Table 4.1 has $A_t \simeq 3.7\%$ and 3.8% for $h_0/\lambda = 3\%$ and 6%, respectively). Therefore, $u_{*\text{th}}$ can be converted to a threshold U_{Shields} in bulk wind speed,

$$\rho U_{\text{Shields}}^2 \simeq \frac{A_N}{A_t^2} \rho_s g d. \tag{4.32}$$

Meanwhile, grain mobilization by pore pressure gradients arises first where $F\mathbb{R} = 1$, i.e. where F is largest. Therefore, substituting Eq. (4.31), such incipient mobilization occurs past a minimum wind energy

$$\rho U_{\Delta}^2 = \frac{\rho_s g \nu \lambda^2}{F_{\text{max}} h_0}. \tag{4.33}$$

Note that this prediction of a threshold speed U_Δ independent of particle diameter is in sharp contrast with traditional gas-solid fluidized beds, in which the superficial gas velocity v_{mf} at minimum fluidization increases with particle size. As Tsinontides and Jackson [212] showed, a frictionless bed fluidizes as soon as v reaches v_{mf}, thus adopting the gravity-driven pressure gradient $\nabla p = \rho_s \nu \mathbf{g}$, so that $v_{\text{mf}} = K \rho_s \nu g/\mu$; because $K \simeq d^2(1-\nu)^3/(150\nu^2)$, then $v_{\text{mf}} \propto d^2$. The chief reason for interpreting differently the onsets of gas-solid fluidization and grain mobilization by pore pressure gradients is that the former must impose a *superficial gas velocity* $> v_{\text{mf}} \propto d^2$, while the latter reaches a wind-driven *pore pressure gradient* $> \rho_s \nu g$ through an Eq. (4.5) that is independent of K, and therefore of d. Sleath [197] and Foster et al. [72] described a mechanism for oscillatory flows over sediment beds that independent of d for a similar reason.

Comparing Eqs. (4.32) and (4.33), we predict that, as wind speed increases, grain mobilization by deep pore pressure gradients takes place before Shields erosion of surface grains whenever $U_\Delta < U_{\text{Shields}}$ or, equivalently, when

$$\frac{\sqrt{h_0 d}}{\lambda} > \sqrt{\frac{A_t^2 \nu}{A_N F_{\max}}}. \tag{4.34}$$

With $A_N \simeq 0.0123$ [194], $\nu \simeq 0.6$ for a typical sand bed, $A_t \simeq 0.03$, and $F_{\max} \simeq 15$ (Table 4.1), the constant on the right of Eq. (4.34) is $\simeq 0.054$. Thus, for typical desert ripples with $h_0 \simeq 4\,\text{mm}$, $\lambda \simeq 10\,\text{cm}$ and $d \simeq 350\,\mu\text{m}$ [9], pressure gradient-induced grain mobilization should not contribute significantly to overall erosion. However, if such ripples of small aspect ratio became armored by millimetric surface grains of diameter d immobilizing smaller particles below [142], then $\sqrt{h_0 d}/\lambda$ could rise to values approaching criterion (4.34). With such armoring, ripples should then naturally restructure into longer wavelengths to bring down $\sqrt{h_0 d}/\lambda$, lest their foundation of smaller particles disappeared under the action of pore pressure gradients. Such behavior might be relevant to the formation of "megaripples", which feature a large aspect ratio $h_0/\lambda > 3\%$, as well as coarse surface grains able to withstand greater shear velocity before being entrained themselves [225].

4.9 Summary and conclusions

We measured pore pressure below two sinusoidal surfaces of wavelength $\lambda = 100\,\mathrm{mm}$ and amplitude $h_0 = 3\,\mathrm{mm}$ and $6\,\mathrm{mm}$ subject to turbulent flows of bulk speed $3 < U < 36\,\mathrm{m/s}$ in the wind tunnel. The resulting aspect ratios $h_0/\lambda = 3\%$ and 6% straddled a wide range of "ripple index" RI observed in the field [205]. However, to permit comparisons with existing literature on impermeable wavy surfaces, we focused attention on sinusoidal ripples, ignoring for now the asymmetry of desert ripples.

Pore pressure at the smallest aspect ratio $h_0/\lambda = 3\%$ was a single harmonic function of streamwise distance lagging the crest slightly and decaying exponentially with depth. Its amplitude p_1 scaled with kinetic energy of the turbulent flow such that $p_1^* \equiv [p_1/(\rho U^2)](\lambda/h_0) = 2.04 \pm 0.13$, a value smaller than what Louge et al. [137] had assumed for calculating seepage, dust and humidity penetration in desert ripples. On the surface, the dimensionless pressure was nearly dentical in phase and amplitude to earlier measurements of Kendall [119] on an impermeable sinusoidal wall, thus suggesting that the porous substrate is relatively unimportant to surface pressure evolution at that aspect ratio. We showed that, because surface and pore pressure scale with h_0/λ, and because the flow mostly did not separate behind crests, these measurements were also relevant to any sinusoidal ripple with $h_0/\lambda \leqslant 3\%$ (i.e., RI $\gtrsim 16$).

Experiments at $h_0/\lambda = 6\%$ exhibited an asymmetric pore pressure distribution suggesting flow separation behind ripple crests and possible reattachment before the next trough. For this aspect ratio, we compared the evolution of surface pressure on our porous substrate with published data on similar impermeable sinusoidal ripples [34, 85, 98]. While the dimensionless depression that we measured at the crest was identical to those earlier results, we noted a sharp attenuation of surface pressure upwind of the crest, suggesting that the porous medium imposes a markedly different surface pressure gradient on the turbulent boundary layer than on comparable impermeable ripples. By invoking observations of [85] on aerodynamically smooth and rough impermeable ripples, we attributed this attenuation to the retro-diffusion of pore pressure through the bed. Using the boundary condition of Beavers and Joseph [19], we calculated that the porous bed also allows a substantial slip velocity to arise on the surface, further affecting turbulence in the main flow. For simplicity, we regarded such slip as an effective reduction in aerodynamic roughness.

Although pressure drag appeared to increase with $\rho U^2 h_0^2/\lambda$, it was significantly smaller than its counterpart on impermeable wavy surfaces [85, 34, 98]. At $h_0/\lambda = 6\%$, this pressure drag reduction could also be attributed to surface pressure attenuation by retro-diffusion. We recorded a lift force on the ripple surface that appeared to increase $\propto \rho U^2 h_0^3/\lambda^2$, although such scaling should be confirmed with new porous rigs at greater h_0/λ. Finally, we also noted that ripples with $h_0/\lambda = 6\%$ exhale a net amount of air, while ripples of $h_0/\lambda = 3\%$ do not.

Our measurements were sufficiently accurate to evaluate pore pressure gradients ∇p, and thus to gauge where the latter might defeat gravity and mobilize a bed of uniform volume fraction ν and grain material density ρ_s. The onset of mobilization arises when $F\mathbb{R} > 1$, where the number $\mathbb{R} \equiv \rho U^2 h_0/(\rho_s \nu g \lambda^2)$ regroups wind and bed parameters. Ignoring internal friction, $F \equiv (\partial p/\partial y)\lambda^2/(\rho U^2 h_0)$ peaks at $F_{\max} \simeq 17$ for $h_0/\lambda = 3\%$, and at the surprisingly similar value $F_{\text{max}} \simeq 15$ for 6%. For the smaller aspect ratio, the peak is reached near the crest; for the larger one, F_{max} arises at a distance $\simeq \lambda/10$ upstream of that point, nearby where the theory of Jackson and Hunt [114] also places the peak shear stress.

Exploiting our measurements and recalling the correlation of Shao and Lu [194] for threshold velocity in aeolian transport, we calculated that pressure gradient-induced fluidization of the porous bed would occur before shear-induced erosion of surface grains of diameter d whenever $\sqrt{h_0 d}/\lambda > 0.054$. While this criterion is rarely observed in aeolian ripples with relatively small h_0/λ [205], our measurements suggest that it may contribute to the shaping of megaripples with high aspect ratios and coarse surface grains. Because this criterion is independent of fluid properties, aqueous ripples may also owe their mobilization, at least in part, to pore pressure gradients within the underlying bed.

Finally, because ripples are generally asymmetrical unless their aspect ratio h_0/λ is small [13], future experiments should be conducted with cross-sections of various asymmetry [205], beginning with triangular shapes [27]. Because to our knowledge there is no data for the pressure evolution on impermeable bedforms of triangular cross-section, these future experiments will have to involve both porous and solid surfaces to discern the role of porosity. In this context, some useful insight might be found in the literature on "k-type roughness", in which the ratio w/k of "cavity length" $w \sim \lambda/2$ to "cavity height" $k \sim 2h_0$ exceeds 3 (or, in our notation, $h_0/\lambda < 1/12$) [162, 132]. Nonetheless, we would expect that the porous medium will play a similar role on a triangular ripple than it does on a sinusoidal one, namely that porosity should induce seepage through the bed, thus attenuating the surface pressure gradient, and allowing slip at the surface.

In conclusion, our wind tunnel experiments suggested that, for ripples of large amplitude relative to wavelength, bed porosity disrupts surface pressure gradients by allowing pore pressure to retro-diffuse through the bed and by establishing a slip velocity at the surface. For ripples of smaller relative amplitude, the data showed that bed porosity matters less to surface pressure. It also established the magnitude of pressure variations, which govern seepage through the bed and the possible capture of aeolian dust beneath ripple troughs. Finally, our experiments implied that seepage-induced fluidization may contribute to the shaping of megaripples with high aspect ratios and coarse surface grains.

APPENDIX A

APPENDICES OF STATISTICAL MECHANICS OF UNSATURATED POROUS MEDIA

A.1 Lagrange multiplier

In this Appendix, we show that the dimensionless Lagrange multiplier β' in Eq. (2.15) is very large during the reversible approach to the draining phase transition. (A similar calculation can be applied to the wetting transition). We consider an elementary removal of wetting fluid. Because at least one liquid phase is involved, the speed of sound is high enough for a typical system to re-equilibrate quickly and thoroughly to any small reduction $\mathrm{d}S < 0$ in saturation of the mesoscopic domain. The resulting change in dimensionless total entropy $\aleph_t$, which involves all active molecular degrees of freedom, has three contributions, $\mathrm{d}\aleph_t = \beta'\mathrm{d}\mathcal{H}' + d\aleph_g - d\aleph_\ell$. The first is from the change $\mathrm{d}\mathcal{H}'$ in dimensionless total energy [41]; the second is the entropy input of non-wetting fluid $\mathrm{d}\aleph_g = -[\rho_g \ell_0^3 \hat{s}_g/(k\mathrm{MW}_g)]\mathrm{d}S$; and the third is the corresponding entropy ouput of wetting fluid, $\mathrm{d}\aleph_\ell = -[\rho_\ell \ell_0^3 \hat{s}_\ell/(k\mathrm{MW}_\ell)]\mathrm{d}S$. In these expressions, k is Boltzmann's constant, and ρ_g, $\hat{s}_g$, and MW_g are, respectively, the density, absolute molar entropy and molecular weight of non-wetting fluid, while ρ_ℓ, $\hat{s}_\ell$, and MW_ℓ are the corresponding quantities for the wetting fluid. Because the process is reversible until the phase transition, $\mathrm{d}\mathbb{S}_t = 0$. Combining these relations,

$$\beta' = -\left(\frac{\mathrm{d}S}{\mathrm{d}\mathcal{H}'}\right)\left[\frac{\ell_0^3}{k}\left(\frac{\rho_\ell \hat{s}_\ell}{\mathrm{MW}_\ell} - \frac{\rho_g \hat{s}_g}{\mathrm{MW}_g}\right)\right]. \tag{A.1}$$

In typical situations, the term in straight brackets, which we call A, is very large. For the air-water system with $\hat{s}_\ell \simeq 70\,\mathrm{J/mol.K}$ and $\hat{s}_g \simeq 194\,\mathrm{J/mol.K}$, $A \simeq 3.10^{11}$ with $\ell_0 = 1\,\mu\mathrm{m}$. If decane is the non-wetting fluid ($\rho_g = 730\,\mathrm{kg/m^3}$, $\hat{s}_g \simeq$

$425\,\mathrm{J/mol.K}$), then $A \simeq 10^{11}$. In the spirit of the mean-field theory, we estimate the total energy from Eq. (2.31) as $\mathcal{H}' \simeq (0.5 - S)\left[-\psi' + \bar{\alpha}\cos\theta_c - (1-2S)\,\bar{\lambda}\right]$, such that $\mathrm{d}\mathcal{H}' \simeq 2\,(1-2S)\,\bar{\lambda}\mathrm{d}S - (0.5-S)\,\mathrm{d}\psi'$. Using Eq. (A.1),

$$\beta' \simeq \frac{2A/(2S-1)}{4\bar{\lambda} - \partial\psi'/\partial S}. \tag{A.2}$$

Toward the draining phase transition where $|\partial\psi'/\partial S| \ll 1$ and $S \sim 1$, $\beta' \sim A/2\bar{\lambda} \gg 1$.

A.2 Sphere packings

We consider porous media consisting of interstices within random, polydisperse, dense packings of spheres. Studies of such granular assemblies typically focus on compaction of the solid [12], rather than on the statistical distribution of voids and openings [46]. For example, Edwards and Oakeshott [55] applied statistical mechanics to powder compaction. However, the mean solid volume fraction ν matters less to the retention curve than it does to the mechanics of granular materials. Whereas a small increment in ν can induce jamming in random packings [45], such increment does not affect the void space as much and, consequently, the retention curve is not changed substantially.

To our knowledge, no research has yet established the joint distribution $F(\lambda, \alpha)$ of void space that random spherical packings create. As a first attempt to characterize F, we exploit the Delaunay triangulation, which subdivides space into irregular tetrahedra having vertices on the centers of spheres of diameter d_j. This triangulation is unique, as long as centers lie in "general position", i.e. no three centers are aligned, no four centers lie on a plane or a circle, and no five centers are arrayed on a sphere [49].

Here, links have planar cross-sections obtained by removing three circular sectors from each tetrahedral face. Similarly, the cavity of index i is what remains of a tetrahedron of volume v_{t_i} after excision of $n = 4$ spherical sectors centered on each apex j with solid angles ϖ_j subtending the opposite face. Then, cavity volume and area are, respectively $v_{c_i} = v_{t_i} - \sum \varpi_j d_j^3/24$ and $a_{c_i} = \sum \varpi_j d_j^2/4$ for $j = 1, n$. Figure 2.3 illustrates the resulting joint distribution for a packing obtained through numerical simulations.

Although triangulation is a robust method for identifying unambigously cavities and links in a packing of spheres, it only allows $n = 4$ near-neighbors around an individual cavity. Because accuracy of the mean-field theory grows with n [41, 203], one could contemplate grouping m adjacent tetrahedral cavities into a new unit cell with $n = 3m + 1$ external links and 2^m possible filling states, each with a different unit cell energy E. The partition function in Eq. (2.9) would then include 2^m terms. Unfortunately, there would now be three kinds of dimensionless ratios arising from the energy of a unit cell, namely m parameters similar to α, another m similar to λ and $m - 1$ independent ratios of cavity and unit cell volumes. For example, a unit cell with two cavities of index 1 and 2 would have seven links, four possible filling states $(\sigma_1, \sigma_2) = (+1, +1)$, $(+1, -1)$, $(-1, +1)$, or $(-1, -1)$, and a five-dimensional joint statistical distribution of independent geometrical parameters. While being more accurate [41, 203], this higher-order mean-field treatment would therefore trade-off the relative simplicity of interpretation that we have exploited in this article with $m = 1$. However, it would make it straightforward to handle relatively rare cavities that a triangulation subdivides artificially, such as a five-sphere pyramid with a square base.

A.3 Hysteresis Strength

Consider a $\mathbb{R}^{2+}$ parameter space (λ, α), like that shown in Fig. 2.3. From Eq. (2.14), the two domains Ω_- and Ω_+ are separated by the straight dividing line of slope $\bar{\sigma}/\cos\theta_c$ and intercept $\psi'/\cos\theta_c$, and are therefore complementary, i.e. $(\Omega_+ \cup \Omega_- = \mathbb{R}^{2+}; \Omega_+ \cap \Omega_- = \emptyset)$. Meanwhile, integrals in Eq. (2.21) can be interpreted as "masses" contained within each planar domain with "surface density" F. In that view, the "center of mass" of the entire plane has coordinates

$$\bar{\lambda} \equiv \iint \lambda\, F \,\mathrm{d}\lambda \mathrm{d}\alpha, \tag{A.3}$$

and

$$\bar{\alpha} \equiv \iint \alpha\, F \,\mathrm{d}\lambda \mathrm{d}\alpha. \tag{A.4}$$

When λ and α are single-valued (i.e. $\lambda = \bar{\lambda}$ and $\alpha = \bar{\alpha}$), the phase transitions described in section 2.3 arise when one of the two dividing lines $\mathcal{L}_-$ and $\mathcal{L}_+$ from Eq. (2.14) intersects the center of mass (Fig. 2.2, top). The corresponding intercepts mark the two transition pressures ψ'_- for $\bar{\sigma} = -1 \to +1$ (line $\mathcal{L}_-$) and ψ'_+ for $\bar{\sigma} = +1 \to -1$ (line $\mathcal{L}_+$). If the domain starts saturated $(\bar{\sigma} = -1)$, line $\mathcal{L}_-$ has negative slope $-1/\cos\theta_c$. If instead it starts dry, $\mathcal{L}_+$ has positive slope $+1/\cos\theta_c$.

Consider now a porous domain with broader surface density F (Fig. 2.3). Without loss of generality, assume that it begins saturated $(\bar{\sigma} = -1)$. Because the magnitude $|\bar{\sigma}_-|$ of the transition filling state is necessarily < 1, the slope of the dividing line between Ω_- and Ω_+ at phase transition is not as steep as $\mathcal{L}_-$. In addition, this dividing line can no longer pass through the center of mass, since doing so would imply an equal "mass" on both sides, which, from Eq. (2.21), would lead to $\mathbb{I} = 0$. However, because $\bar{\sigma}_- \neq 0$, $\mathbb{I} = 0$ could not be a solution to Eq. (2.20). Instead, the dividing line must be further displaced downward, so the Ω_- domains captures more mass, bringing $\bar{\sigma}_-$ to the negative sign that we expect. In short, there are two reasons why the new transition ψ'_- is lower with a broader F. First, the slope of the dividing line is not as steep, thus reducing the intercept $\psi'/\cos\theta_c$. Second, the latter moves farther down to satisfy Eq. (2.20).

A similar argument shows that ψ'_+ increases with a broader F. Overall, if the hysteresis strength is measured as the difference between the two capillary transition pressures, it is always weaker with a broad distribution of cavities and links than the single-valued case in Eq. (2.27), i.e.

$$\Delta\psi' \equiv \psi'_- - \psi'_+ < 2\bar{\lambda}. \tag{A.5}$$

A.4 Correlation probability

We calculate the probability that the m-th nearest neighbor of a cavity holds the same filling state, and we extract at which near-neighbor index this probability has decayed substantially. We restrict attention to the case where all cavities and links have a single size. (For complicated geometries, Monte-Carlo simulations contrained to uphold the overall voidage could refine predictions, albeit without the benefit of simplicity).

In a system with uniform cavity volume, the probability for a cavity to hold a filling state σ of the same sign as the volume-average $\bar{\sigma}$ is

$$\mathrm{Pr}_0 \equiv \mathrm{Pr}(\sigma\,\bar{\sigma} > 0) = (1/2)(1 + |\bar{\sigma}|). \tag{A.6}$$

(For example, if $\bar{\sigma} = 0$, cavities have equal probability to hold one or the other state; for $|\bar{\sigma}| = 1$, all cavities have the same sign). Equivalently, the probability

$\mathrm{Pr}(\sigma)$ for the original cavity to hold the state σ is Pr_0 if $\bar{\sigma} > 0$ or $1 - \mathrm{Pr}_0$ if $\bar{\sigma} < 0$.

First, consider a cavity filled with liquid ($\sigma = -1$). If $\bar{\sigma} > 0$, then the probability for its first-nearest neighbor to have the same filling state is $\mathrm{Pr}_1 = 1 - \mathrm{Pr}_0$. If instead $\bar{\sigma} < 0$, then $\mathrm{Pr}_1 = \mathrm{Pr}_0$. A similar argument applies to a gas-filled cavity. In general, $\mathrm{Pr}_1(\sigma) = (1 + \sigma\bar{\sigma})/2$. In the spirit of the mean-field theory, whereby the energy of a cavity is only affected by the state of its first nearest neighbors, Pr_1 is generalized recursively. Then, the probability for the m-th nearest neighbor to have the same σ is

$$\mathrm{Pr}_m(\sigma) = (1 + \sigma\bar{\sigma})^m / 2^m, \tag{A.7}$$

where σ can either be -1 or $+1$. Therefore, the probability to have a m-th nearest neighbor of the same filling state as the original cavity is $\mathrm{Pr}_c = \mathrm{Pr}_m(+1)\mathrm{Pr}(+1) + \mathrm{Pr}_m(-1)\mathrm{Pr}(-1)$. Overall, substituting saturation for $\bar{\sigma}$ using Eq. (2.23),

$$\mathrm{Pr}_c = (1 - S)^{m+1} + S^{m+1}. \tag{A.8}$$

A.5 Role of contact angle

Because a link involves a gas-liquid interface if σ changes sign across it, its area can deform away from the dry opening cross-section anytime the contact angle θ_c differs from $\pi/2$. In principle, capillary pressure could also modify the interface shape. However, because effects discussed in this article occur in a relatively narrow range of ψ around $\sim \gamma_{\ell g}/\bar{\ell}_0$, and because links are small, ψ should contribute negligibly to interface distortion.

Ignoring subtle details of interface geometry [159], we estimate the deformation for $\theta_c \neq \pi/2$ by invoking the similar case of a cylindrical capillary, in which the meniscus is small enough to be nearly spherical. In this analogy, the ratio of link interface area a_ℓ and its dry cross-section a_{ℓ_0} is similar to the ratio of meniscus area to capillary cross-section,

$$a_\ell/a_{\ell_0} \simeq 2/\left(1+\sin\theta_c\right), \tag{A.9}$$

where the subscript 0 represents "dry" geometrical quantities measured in the absence of liquid. A distortion of identical area occurs if gas resides on one side of the gas-liquid interface or the other. If instead a link connects two cavities with the same phase (gas or liquid), then its area does not matter to cavity energy, and may be conveniently taken to satisfy Eq. (A.9) as well. Therefore, all links adopt an area that is greater than the dry value a_{ℓ_0} by a common factor in the range $1 < a_\ell/a_{\ell_0} < 2$.

Similarly, the deformation of a link matters to the volume v_c in Eq. (2.2), only if it connects two cavities of a different phase. Therefore, the contribution of a single link to the difference $(v_c - v_{c_0})$ is either zero or a volume increment of magnitude Δv_c. Exploiting a similar capillary approximation than toward Eq. (A.9), and assuming for simplicity that all n links around a given cavity have the same area, interface distortion amounts to

$$\delta \equiv n\frac{\Delta v_c}{v_{c_0}} \simeq \frac{a_{\ell_0}^{3/2}}{v_{c_0}}\left(\frac{2-3\sin\theta_c+\sin^3\theta_c}{3\sqrt{n\pi}\cos^3\theta_c}\right). \tag{A.10}$$

Consider a cavity filled with liquid ($\sigma = -1$). Here, distortion of gas-liquid interfaces shrinks its dry volume v_{c_0} by an amount $\sigma n_{\neq}\Delta v_c$ contributed by its $n_{\neq}$ links connected to gas-filled neighbors. A similar argument can be constructed for a gas-filled cavity, where $n_{\neq}$ links to liquid-filled neighbors swell its dry volume, again by the amount $\sigma n_{\neq}\Delta v_c$. In all cases, using results in Appendix A.4, we have $n_{\neq}/n = 1 - \mathrm{Pr}_1$, so that $\left(v_c - v_{c_0}\right)/v_{c_0} = \sigma n \Delta v_c (1-\sigma\bar{\sigma})/2 =$

$n\Delta v_c(\sigma - \bar{\sigma})/2$. On average,

$$\overline{(v_c - v_{c_0})\,/v_{c_0}} \simeq \overline{\delta\,(\sigma - \bar{\sigma})}/2. \tag{A.11}$$

Therefore, by the ergodic condition $\bar{\sigma} = \langle\sigma\rangle$, this correction in average cavity volume vanishes whenever δ is constant, for example with single-valued dry link area and cavity volume. It also vanishes in the general case if, as expected, the domain statistics of $a_{\ell_0}^{3/2}/v_{c_0}$ are uncorrelated with those of σ. However, the mean absolute excursion $\overline{|v_c - v_{c_0}|/v_{c_0}} \simeq \overline{\delta\,(1 - \sigma\bar{\sigma})}/2$ does not vanish, but it is usually small, since λ_0 is typically $\sim O(1)$ and the terms in parentheses in Eq. (A.10) is $\leqslant 2/3\sqrt{n\pi}, \forall\theta_c$. For example, tetrahedral cavities in a hexagonal close packing have $a_{\ell_{0\triangle}}^{3/2}/v_{c_{0\triangle}} \simeq 2.49$ (see supporting information), so $\overline{|v_c - v_{c_0}|/v_{c_0}} < 0.23\,(1 - \bar{\sigma}^2)\,, \forall\theta_c < \pi/2$ and $< 0.1\,(1 - \bar{\sigma}^2)$ for typical $\theta_c > 35°$. Because phase transitions occur near $|\bar{\sigma}| \lesssim 1$, fluctuations in cavity volume due to contact angle can therefore be ignored in most cases.

Finally, because the position of the triple contact line on the link periphery is relatively insensitive to the contact angle, the internal cavity area a_c hardly depends upon θ_c either. Overall, hydrophilic contact angles chiefly affect the magnitude of λ. From Eq. (A.9),

$$\lambda/\lambda_0 \simeq 2/\left(1 + \sin\theta_c\right), \tag{A.12}$$

thereby predicting that hysteresis should strengthen at lower contact angle (Eq. 2.28).

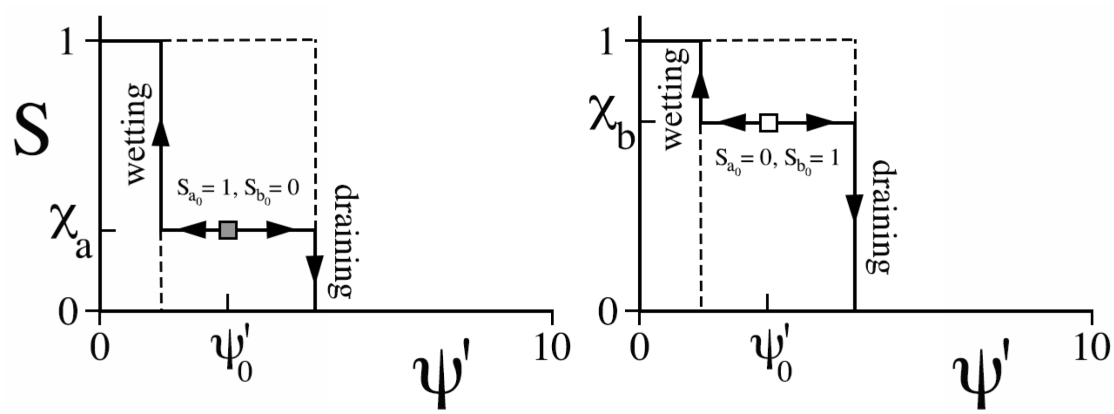

Figure A.1: Apparent macroscopic retention curve for two adjacent mesoscopic domains subject to the same capillary pressure but different initial mean saturation, and drawn for conditions of Fig. 2.2. Right: the open square represents initial saturations $S_{a_0} = 0$ and $S_{b_0} = 1$, and an initial capillary pressure ψ'_0 between ψ'_+ and ψ'_-. Left: The filled square is the same initial pressure but with $S_{a_0} = 1$ and $S_{b_0} = 0$. Both apparent retention curves invade the region between the main curves (dashed lines) shown in Fig. 2.2.

A.6 Macroscopic inhomogeneities

To illustrate the role of inhomogeneities, we consider a hypothetical porous medium consisting of two adjacent mesoscopic subdomains ⓐ and ⓑ occupying different parts $V_a = \chi_a V$ and $V_b = \chi_b V$ of the total cavity volume $V = V_a + V_b$ with distinct mean saturations S_a and S_b, but subject to the same dimensionless applied pressure ψ'. For clarity, the entire medium has single-valued cavity and link sizes. Therefore, ⓐ and ⓑ share the transition pressures ψ'_+ and ψ'_- (section 2.3).

Figure A.1 show the medium's response to generic initial conditions. If the two domains start with an initial capillary pressure $\psi'_0 < \psi'_+$ (fully saturated), or $\psi'_0 > \psi'_-$ (dry), they both experience the same saturation history and effectively behave as a single domain. If instead the two domains start at an intermediate pressure $\psi'_+ < \psi'_0 < \psi'_-$, then the overall saturation subsequently depends upon initial condition S_{a_0} and S_{b_0} for the two subdomains. If an initially saturated domain ⓐ ($S_{a_0} = 1$) is juxtaposed with a dry domain ⓑ ($S_{b_0} = 0$), then ⓐ stays saturated as ψ' rises from ψ'_0 until the phase transition ψ'_-. This produces a horizontal segment on the joint retention retention curve at an apparent mean saturation $S = \theta/(1-\nu) = \chi_a$. Conversely, if ⓐ starts dry while ⓑ is saturated, then the retention curve features a similar segment at $S = \chi_b = 1 - \chi_a$. In either case, these segments in the overall retention curve invade the region in the (ψ', S) state space. Similar invasions arise with a more general distribution $F(\lambda, \alpha)$, with positions that are sensitive to the initial inhomogeneous distribution of liquid.

A.7 Hexagonal close packing

In this Appendix, we derive the mesoscopic retention curve for an hexagonal close packing of identical spheres (HEX) in analytical form. This configuration is instructive, as it provides a Heaviside hysteresis, but with separation between the wetting and draining phase transitions that is narrower than what a hypothetical medium with single-valued $\bar{\lambda}$ and $\bar{\alpha}$ would produce. It may also constitutes a convenient test of the theory in future 3D tomographic experiments.

In such crystal, there are two kinds of cavities. The first is enclosed within regular tetrahedra of four touching spheres (denoted by the subscript $\triangle$). The second (denoted by $\square$) is found within pyramids consisting of four touching spheres with centers on a square and contacting a fifth sphere. The first kind has a dry cavity volume $v'_{c0_\triangle} = 1/6\sqrt{2} - \pi/3 + \arctan(\sqrt{2})$, a dry cavity surface area $a'_{c0_\triangle} = 2\pi - 6\arctan(\sqrt{2})$, and the sum of its $n_\triangle = 4$ dry link cross-section areas is $a'_{\ell_{0\triangle}} = \sqrt{3} - \pi/2$. The second kind has $v'_{c_{0\square}} = 1/3\sqrt{2} + \pi/4 - \arctan(\sqrt{2})$, $a'_{c_{0\square}} = 6\arctan(\sqrt{2}) - 3\pi/2$, and its $n_\square = 5$ links add up to $a'_{\ell_{0\square}} = 1 + \sqrt{3} - 3\pi/4$. In these expressions, primes denote quantities dimensionless with sphere diameter. Because in a HEX the two kinds are present in equal numbers, the mean dry cavity volume is $\bar{v}'_{0c} = \left(v'_{c_{0\triangle}} + v'_{c_{0\square}}\right)/2$, so that $\bar{\ell}_0 = \left(\sqrt{2} - \pi/3\right)^{1/3}/2$. Then, the cavity volume fractions are $\chi_\triangle = v'_{c_\triangle}/(v'_{c_\triangle} + v'_{c_\square})$, or

$$\chi_\triangle = 1 - \chi_\square = \frac{\left[\sqrt{2} - 4\pi + 12\arctan\left(\sqrt{2}\right)\right]}{\left(3\sqrt{2} - \pi\right)} \tag{A.13}$$

and $\chi_\square = 1 - \chi_\triangle = 0.716\cdots$. Consequently, the two kinds of cavities have different values λ_0 and α_0, namely

$$\lambda_{0\triangle} = \frac{3^{1/6}\left(3\sqrt{2} - \pi\right)^{1/3}\left(6 - \pi\sqrt{3}\right)}{\sqrt{2} - 4\pi + 12\arctan\left(\sqrt{2}\right)}$$

$$\alpha_{0\triangle} = \frac{4 \times 3^{2/3}\left(3\sqrt{2} - \pi\right)^{1/3}\left[\pi - 3\arctan\left(\sqrt{2}\right)\right]}{\sqrt{2} - 4\pi + 12\arctan\left(\sqrt{2}\right)} \tag{A.14}$$

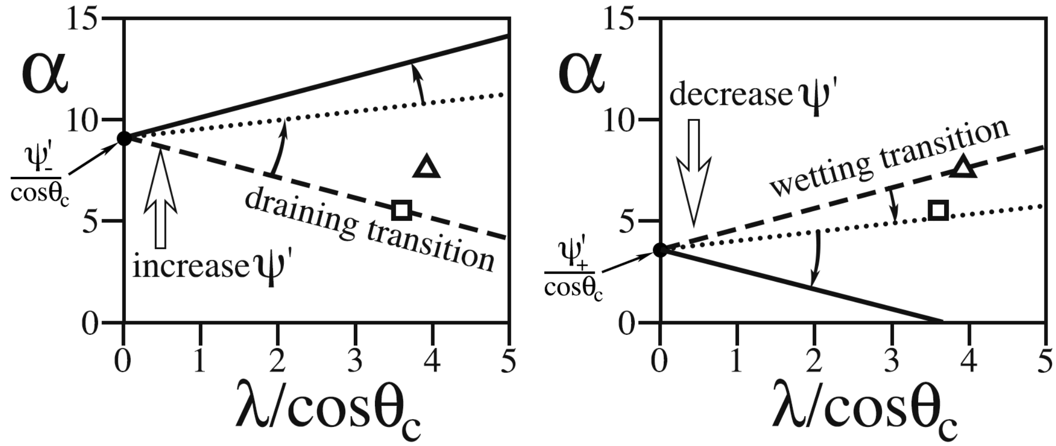

Figure A.2: Graphs of α vs $\lambda/\cos\theta_c$ illustrating the draining (left) and wetting (right) phase transitions for a HEX, drawn with $\theta_c = 50°$ and assuming $\alpha = \alpha_0$ and λ given by the estimate in Eq. (A.12). Left: increasing capillary pressure ψ' of an initially saturated sample brings the dashed line of slope $(\bar{\sigma} = -1)$ (Eq. 2.22) to the draining transition as it intersects the square at $(\alpha_\Box, \lambda_\Box)$ when $\psi' = \psi'_-$. The resulting integral $\mathbb{I}$ in Eqs. (2.20)-(2.21) then flips $\bar{\sigma}$ to $(\chi_\Box - \chi_\triangle) \approx 0.434$, thereby rotating the slope to that value. Because the resulting dotted line lies above the triangle at $(\alpha_\triangle, \lambda_\triangle)$, it is further rotated to $(\bar{\sigma} = +1)$, so that the phase transition drains the sample completely. Right: the reverse process as ψ' is reduced in an initially dry sample. Here, the wetting transition occurs as the dashed line of slope $(\bar{\sigma} = +1)$ reaches the triangle at $(\alpha_\triangle, \lambda_\triangle)$ with transition pressure ψ'_+. This reduces the slope to the same intermediate value $(\chi_\Box - \chi_\triangle)$ (dotted line), which lies just below the square, thereby completing the transition to complete wetting.

and

$$\lambda_{0\Box} = \frac{3^{2/3}\left(4 + 4\sqrt{3} - 3\pi\right)\left(3\sqrt{2} - \pi\right)^{1/3}}{6\pi + 4\left[\sqrt{2} - 6\arctan\left(\sqrt{2}\right)\right]}$$
$$\alpha_{0\Box} = \frac{3^{5/3}\left(3\sqrt{2} - \pi\right)^{1/3}\left(4\arctan\left(\sqrt{2}\right) - \pi\right)}{3\pi + 2\left[\sqrt{2} - 6\arctan\left(\sqrt{2}\right)\right]} \tag{A.15}$$

Combining with Eq. (A.13), we find $\bar{\lambda}_0 = \chi_\triangle\lambda_{0\triangle} + \chi_\Box\lambda_{0\Box} = 2.095\cdots$ and $\bar{\alpha}_0 = \chi_\triangle\alpha_{0\triangle} + \chi_\Box\alpha_{0\Box} = 6.128\cdots$. Therefore, the distribution F consists of two delta-functions centered at $(\lambda_\Box, \alpha_\Box)$ and $(\lambda_\triangle, \alpha_\triangle)$ with respective strengths $\chi_\Box$ and $\chi_\triangle$ (Fig. A.2).

Consider a saturated HEX with $\bar{\sigma} = -1$. As relative capillary pressure ψ'

is increased (Fig. A.2 left), the line $\alpha \cos\theta_c = \psi' + \bar{\sigma}\lambda$ eventually overtakes the $(\lambda_\square, \alpha_\square)$ delta-function (draining transition), thus raising $\bar{\sigma}$ to the intermediate dotted slope $(\chi_\square - \chi_\triangle)$ imposed by Eqs. (2.20) and Eq. (2.21). Because this line lies above the $(\lambda_\triangle, \alpha_\triangle)$ delta function, the transition must proceed to complete drainage, as indicated by two consecutive black arrows.

Conversely, as ψ' is reduced on a dry HEX, the wetting transition occurs as $(\lambda_\triangle, \alpha_\triangle)$ is reached with $\psi'_+ = \alpha_\triangle \cos\theta_c + \lambda_\triangle$, thus flipping the slope, once again, to the same intermediate value $(\chi_\square - \chi_\triangle)$. Because the resulting dotted line lies just below the square, the wetting process is also completed immediately. To guarantee this, $(\alpha_\triangle - \alpha_\square)\cos\theta_c$ must be $< \lambda_\triangle - \lambda_\square(\chi_\square - \chi_\triangle)$. Coincidentally, if we adopt the estimate in Eq. (A.12) and $\alpha = \alpha_0$, this inequality is always satisfied, albeit just so when $\theta_c = \pi/6$. Therefore, if our estimates of the role of contact angle (Appendix A.5) prove inaccurate, a two-step wetting transition may yet occur around $\theta_c \simeq \pi/6$.

In short, our prediction for retention curves of a HEX adopts the Heaviside shape in Fig. 2.2. However, the air-entry potential $\psi'_- = \alpha_\square \cos\theta_c + \lambda_\square$ of a HEX is closer to its wetting pressure $\psi'_+ = \alpha_\triangle \cos\theta_c - \lambda_\triangle$ than if both phase transitions occurred on a single delta-function $(\bar{\lambda}, \bar{\alpha})$.

Finally, we evaluate the latent energy involved in the first-order phase transitions of the HEX by summing Eq. (2.7) over all cavities. Once made dimensionless with $\gamma_{\ell g}/\bar{\ell}_0$, the result yields the total energy $\mathcal{H}'$ in a unit volume of the mesoscopic domain. For saturated and dry HEX, respectively,

$$\mathcal{H}'(\sigma = \mp 1) = \pm\frac{\psi'}{2} \mp \cos\theta_c \frac{(a_{c_\triangle} + a_{c_\square})}{4\bar{\ell}_0^2} - \frac{(a_{\ell_\triangle} + a_{\ell_\square})}{4\bar{\ell}_0^2}. \tag{A.16}$$

Then, the latent energy in the draining and wetting transition are, respectively, $\mathbb{L}'_{\mp} = \mathcal{H}'(\sigma = \pm 1) - \mathcal{H}'(\sigma = \mp 1)$, or

$$\mathbb{L}'_{-} = -\lambda_{\square} - \cos\theta_c \left[\alpha_{\square} - \left(a_{c_{\triangle}} + a_{c_{\square}}\right)/4\bar{\ell}_0^2\right] \tag{A.17}$$

and

$$\mathbb{L}'_{+} = -\lambda_{\triangle} + \cos\theta_c \left[\alpha_{\triangle} - \left(a_{c_{\triangle}} + a_{c_{\square}}\right)/4\bar{\ell}_0^2\right], \tag{A.18}$$

which can be used to predict the behavior of Haines jumps as in section 2.6.

A.8 Slope of the retention curve

A practical use of the solution in Eq. (2.20) is to find the derivative $\partial\psi/\partial S$ that appears in Richards' Eq. (3.8). To that end, we calculate $\partial\bar{\sigma}/\partial\psi' = \partial\mathbb{I}/\partial\psi'$ by differentiating first the left integral in Eq. (2.21). By Leibniz's theorem,

$$\frac{\partial}{\partial\psi'} \iint\limits_{\Omega_+} F \,\mathrm{d}\lambda\mathrm{d}\alpha = \tag{A.19}$$
$$\iint\limits_{\Omega_+} \frac{\partial F}{\partial\psi'} \,\mathrm{d}\lambda\mathrm{d}\alpha + \oint_{C_+} F \frac{\partial \mathbf{M}_+}{\partial\psi'} \cdot \mathbf{n}_+ \mathrm{d}s,$$

where C_+ is the contour of the Ω_+ domain in (λ, α) space, $\mathbf{n}_+$ is its outward unit normal at the point M_+, and $\mathrm{d}s$ is the curvilinear coordinate on C_+. Assuming for simplicity that F is not affected by ψ', the first term to the right of Eq. (A.19) vanishes. Then, the only contribution to the second term is from the only part of C_+ that can change with ψ', namely the part of the straight line satisfying

$$\alpha = (\lambda\bar{\sigma} + \psi')/\cos\theta_c \equiv \alpha_C(\lambda), \tag{A.20}$$

such that λ and α remain positive. On that line, $\partial\mathbf{M}_+/\partial\psi' = (0, 1/\cos\theta_c)$ and $\mathbf{n}_+\mathrm{d}s = (-\bar{\sigma}/\cos\theta_c, 1)\mathrm{d}\lambda$ from Eq. (2.22). Therefore,

$$\frac{\partial}{\partial\psi'} \iint\limits_{\Omega_+} F \,\mathrm{d}\lambda\mathrm{d}\alpha = \int_{\lambda_{\min}}^{\lambda_{\max}} F\left(\lambda, \alpha_C\right)\mathrm{d}\lambda/\cos\theta_c, \tag{A.21}$$

in which $\lambda_{\text{min}} = 0$ and $\lambda_{\text{max}} = \max(0, -\psi'/\bar{\sigma})$ for $\bar{\sigma} < 0$, and $\lambda_{\text{min}} = \max(0, -\psi'/\bar{\sigma})$ and $\lambda_{\text{max}} = +\infty$ for $\bar{\sigma} > 0$. A similar calculation yields the right integral in Eq. (2.21). There, Leibniz's theorem is invoked on the Ω_- domain with contour C_-, yielding the equal and opposite result to Eq. (A.21). Overall, $\partial\mathbb{I}/\partial\psi'$ is twice the result in that Eq. Finally, using Eq. (2.23) to convert $\bar{\sigma}$ to θ, we find

$$\frac{\partial S}{\partial \psi'} = -\frac{1}{\cos\theta_c}\int_{\lambda=\lambda_{\text{min}}}^{\lambda_{\text{max}}} F\left(\lambda, \alpha_C\right) \mathrm{d}\lambda. \tag{A.22}$$

Our experience with the numerical integration of Eq. (A.22) is that it is precise for ψ' up to the draining transition. However, its accuracy deteriorates for wetting. For that transition, a better alternative is to express Eq. (A.22) in terms of α. Defining $\lambda_C \equiv \left(\alpha\cos\theta_c - \psi'\right)/\bar{\sigma}$, a similar calculation yields

$$\frac{\partial S}{\partial \psi'} = -\frac{1}{\bar{\sigma}}\int_{\alpha=\alpha_{\text{min}}}^{\alpha_{\text{max}}} F\left(\lambda_C, \alpha\right) \mathrm{d}\alpha, \tag{A.23}$$

where $\alpha_{\text{min}} = 0$ and $\alpha_{\text{max}} = \max(0, \psi'/\cos\theta_c)$ for $\bar{\sigma} < 0$, and $\alpha_{\text{min}} = \max(0, \psi'/\cos\theta_c)$ and $\alpha_{\text{max}} = +\infty$ for $\bar{\sigma} > 0$.

The transition pressures $\psi'_\pm$ and their corresponding filling states $\bar{\sigma}_\pm$ satisfy simultaneously

$$\frac{\partial\mathbb{I}}{\partial\bar{\sigma}}(\bar{\sigma}_\pm, \psi'_\pm; \theta_c) = +1 \tag{A.24}$$

and

$$\bar{\sigma}_\pm = \mathbb{I}(\bar{\sigma}_\pm, \psi'_\pm; \theta_c). \tag{A.25}$$

Solutions of these two non-linear Eqs. can be obtained by iteration. Whereas evaluating $\mathbb{I}(\bar{\sigma}, \psi'; \theta_c)$ requires two double integrations (Eq. 2.21), the derivative expression in Eq. (A.24) can again be simplified using Leibniz' theorem,

$$\frac{\partial\mathbb{I}}{\partial\bar{\sigma}}(\bar{\sigma}, \psi'; \theta_c) = \frac{2}{\cos\theta_c}\int_{\lambda=\lambda_{\text{min}}}^{\lambda_{\text{max}}} F\left(\lambda, \alpha_C\right) \lambda \mathrm{d}\lambda, \tag{A.26}$$

which can be used to evaluate Eq. (A.24).

APPENDIX B

APPENDICES TO TEMPERATURE AND HUMIDITY WITHIN A MOBILE BARCHAN SAND DUNE

B.1 Radiation model

Because the sky was free of clouds, we could infer broadband radiative properties of our sands from the net radiation collected by the Kipp & Zonen NR Lite 2 instrument of unit normal aligned with the vertical $\hat{\mathbf{z}}$. Using solar ephemeris, we calculated the unit vector $\hat{\mathbf{n}}_s$ along the solar energy flux of magnitude $\dot{q}''_{\text{sun}} \simeq 1353\,\mathrm{W/m^2}$. Regarding sand as a gray body, we then least-squares-fitted its albedo ω and emissivity ϵ over the entire experiment duration to the observed net radiation

$$\dot{q}''_{\text{KZ}} = \dot{q}''_{\text{sun}}(-\hat{\mathbf{z}} \cdot \hat{\mathbf{n}}_s)(1-\omega) - \epsilon\sigma_B T_{s_0}^4 + \epsilon_a \sigma_B T_z^4, \tag{B.1}$$

where T_{s_0} is the sand surface temperature at $x = 0$ and $\sigma_B \simeq 5.6760\,10^{-8}\,\mathrm{W/m^2.K^4}$ is the Stefan-Boltzmann constant. To account for the emission of thermal radiation from the relatively dry clear sky, we adopted an emissivity $\epsilon_a = 0.7$ [167] and used T_z as an estimate of its temperature. We found $\omega \simeq 0.64$ and $\epsilon \simeq 0.86$, values that are typical of arid sands in the region [171]. With these values, we modeled the net radiation striking and leaving the sand surface using Eq. (B.1), in which we replaced $\hat{\mathbf{z}}$ by the unit normal $\hat{\mathbf{n}}_d$ to the point where temperature measurements were carried out within the dune.

B.2 Thermal boundary layer

The Monin-Obukhov similarity [223] couples turbulent transports of momentum and heat in the atmospheric surface layer by expressing gradients of streamwise velocity u and ambient temperature T as

$$\frac{\kappa z}{u^*}\frac{\partial u}{\partial z} = \phi_m\Big(\frac{z}{L}\Big) \tag{B.2}$$

and

$$\frac{\kappa z u^*}{\dot{q}''_{\text{wind}}/\rho c_p}\frac{\partial T}{\partial z} = \phi_h\Big(\frac{z}{L}\Big). \tag{B.3}$$

In Eqs. (B.2) and (B.3), $\kappa \simeq 0.41$ is von Kàrmàn's constant, u^* is shear velocity, z is upward vertical elevation from the ground, g is gravitational acceleration, and ρ and c_p are, respectively, density and specific heat per mass of air. The Monin-Obukhov length is

$$L = \frac{u^{*3}\,\rho c_p T}{\kappa g\,\dot{q}''_{\text{wind}}}. \tag{B.4}$$

In our unusual sign convention where fluxes are counted positive downward into sand, L is negative when the ground loses heat by thermal convection ($\dot{q}''_{\text{wind}} < 0$), and positive otherwise. The atmospheric surface layer is stable upon a temperature inversion whereby the ground is colder than the air aloft i.e., $\dot{q}''_{\text{wind}} > 0$ or $\partial T/\partial z > 0$. In this case, which is typical of the desert at night when buoyancy suppresses turbulent velocity fluctuations, experiments carried out in Kansas in 1968 yielded [223]

$$\phi_m = 1 + a_{m_N} z/L \tag{B.5}$$

where $a_{m_N} \simeq 4.8$, and

$$\phi_h = 1 + a_{h_N} z/L, \tag{B.6}$$

where $a_{h_N} \simeq 7.8$.

When the air is unstable with $\dot{q}''_{\text{wind}} < 0$ or $\partial T/\partial z < 0$, which is typical during the day as the sun warms up the sand surface,

$$\phi_m = \left(1 - a_{m_D} z/L\right)^{-1/4} \tag{B.7}$$

where $a_{m_D} \simeq 19.3$, and

$$\phi_h = \left(1 - a_{h_D} z/L\right)^{-1/2}. \tag{B.8}$$

where $a_{h_D} \simeq 12$.

Because our wind mast only recorded speed $u_1 < u_2$ at two relatively close altitudes $z_1 < z_2$, we could not infer u^* with sufficient accuracy to justify modeling the momentum boundary layer at the precision suggested by Eq. (B.2). Thus for simplicity we adopted $\phi_m \simeq 1$, writing the turbulent velocity profile as

$$u \simeq \frac{u^*}{\kappa} \ln\left(\frac{z + \xi_0}{\xi_0}\right), \tag{B.9}$$

where ξ_0 is surface roughness. We then extracted the ratio of shear velocity and mean flow speed

$$\zeta \equiv \frac{u^*}{\bar{u}} \approx \frac{\kappa}{\ln(z_2/z_1)} \left(\frac{u_2 - u_1}{\bar{u}}\right), \tag{B.10}$$

where $\bar{u} \equiv (u_1 + u_2)/2$ with result $\zeta = 0.084 \pm 0.059$ and $\xi_0 = 11 \pm 1\,\text{mm}$. This magnitude of ζ is typical of turbulent boundary layers profiles [4]. The relatively large roughness is consistent with an abundance of jagged rocks of typical $10\,\text{cm}$ size on hard ground around the dune.

The differential Eq. (B.3) yields relations between convective heat flux at the surface and the difference between sand surface temperature T_{s_0} and ambient air temperature T_z measured at altitude z_T. For $\dot{q}''_{\text{wind}} > 0$, we substitute Eq. (B.6) and integrate to find

$$\frac{\dot{q}''_{\text{wind}}\sqrt{\alpha_s J}}{k_s T_z} = \left(\frac{\bar{u}}{U_r}\right)^2 \frac{\ln(z_T/\xi_0)}{2a_{h_N}}\Xi^* \times$$
$$\left[-\left(\frac{\bar{u}}{U_r}\right) + \sqrt{\left(\frac{\bar{u}}{U_r}\right)^2 + \frac{4a_{h_N}}{\Xi^* \ln^2(z_T/\xi_0)}\left(\frac{T_z - T_{s_0}}{T_z}\right)}\right] \tag{B.11}$$

where

$$\Xi^* \equiv \left(\frac{k_s}{\rho c_p}\right)^2 \frac{1}{\kappa^4 \alpha_s J g z_T} \tag{B.12}$$

is a dimensionless number, and

$$U_r \equiv \frac{k_s}{\kappa \zeta \rho c_p \sqrt{\alpha_s J}} \tag{B.13}$$

is a reference velocity. For $\dot{q}''_{\text{wind}} < 0$, integration of Eq. (B.3) and (B.8) yields an implicit relation to be solved numerically for $\dot{q}''_{\text{wind}}$,

$$\left(\frac{\bar{u}}{U_r}\right)\frac{k_s(T_z - T_{s_0})}{\dot{q}''_{\text{wind}}\sqrt{\alpha_s J}} =$$
$$\ln\left[\frac{1-\sqrt{1-a_{h_D} z_T^*}}{1-\sqrt{1-a_{h_D}\xi_0^*}}\right] + \ln\left[\frac{1+\sqrt{1-a_{h_D}\xi_0^*}}{1+\sqrt{1-a_{h_D} z_T^*}}\right], \tag{B.14}$$

where

$$z_T^* \equiv \frac{\dot{q}''_{\text{wind}}\sqrt{\alpha_s J}}{k_s T_z \Xi^*}\left(\frac{U_r}{\bar{u}}\right)^3 \tag{B.15}$$

and $\xi_0^* \equiv z_T^*(\xi_0/z_T)$.

B.3 Ambient temperature and wind

We recorded temperature and relative humidity at an elevation $z_T \simeq 2\,\text{m}$ from November 2011 to November 2012 using a RM Young RH/T probe with

Table B.1: First line: two-harmonic annual fits of mean temperature $\bar{T}$ in ambient air recorded at $z_T \simeq 2\,\mathrm{m}$ (Eq. B.16). Last three lines: mean temperatures $\bar{T}_{s_0}$ calculated for the sand surfaces shown (Eq. B.18), in which $\bar{\bar{T}}$, ΔT_1 and ΔT_2 represent, respectively, $\bar{\bar{T}}_{s_0}$, $\Delta T_{s_{0_1}}$ and $\Delta T_{s_{0_2}}$. Units are °C (temperatures) and days (t_1, t_2). (Data reduced by Michel Babany.)

	$\bar{\bar{T}}$	ΔT_1	t_1	ΔT_2	t_2
ambient $\bar{T}$	25.9	10.5	96	0.9	289
windward slope $\bar{T}_{s_0}$	28.0	12.7	94	0.7	99
avalanche face $\bar{T}_{s_0}$	37.9	7.5	98	0.7	239
sheltered flats $\bar{T}_{s_0}$	36.0	14.2	91	0.8	60

RH $\pm 2\%$ and $T \pm 0.3\,\mathrm{C}$ accuracy. To a good approximation, monthly-averaged ambient temperatures conformed to the first two harmonics of a Fourier series

$$\bar{T} \simeq \bar{\bar{T}} + \sum_{j=1}^{2} \Delta T_j \sin\left[2\pi j (t - t_j)/Y\right], \tag{B.16}$$

where t_j is the time lag of harmonic
$T_j \equiv \Delta T_j \sin\left[2\pi j (t - t_j)/Y\right]$ with amplitude ΔT_j, and $\bar{\bar{T}}$ is the yearly-averaged surface temperature. Values are found in Table B.1.

On a shorter time scale, ambient temperatures conformed well to the simple model $T \simeq \bar{T} + f_D \delta_D$, where $f_D \simeq f_{D_1} \sin[2\pi(t - t_{D_1})/J] + f_{D_2} \sin[4\pi(t - t_{D_2})/J]$ is a universal dimensionless function capturing diurnal variations with $f_{D_1} \simeq 0.461$, $f_{D_2} \simeq 0.116$, $t_{D_1} \simeq 7.89\,\mathrm{hrs}$, $t_{D_2} \simeq 9.04\,\mathrm{hrs}$ and $J = 24\,\mathrm{hrs}$. The function $\delta_D \simeq \delta_{D_0} + \delta_{D_1} \sin[2\pi(t - t_{\delta_1})/Y] + \delta_{D_2} \sin[4\pi(t - t_{\delta_2})/Y]$ captured diurnal temperature excursions over the whole year $Y = 365\,\mathrm{days}$ with $\delta_{D_0} \simeq 15.3\,°\mathrm{C}$, $\delta_{D_1} \simeq 3.7\,°\mathrm{C}$, $\delta_{D_2} \simeq 1.8\,°\mathrm{C}$, $t_{\delta_1} \simeq 118\,\mathrm{days}$, and $t_{\delta_2} \simeq 217\,\mathrm{days}$.

Over the entire year of measurements, we found that wind speed at elevation z could be modeled as the product $(\bar{\zeta}/\kappa) \ln[(z + \bar{\xi}_0)/\bar{\xi}_0] \times f_W(t) \times U_m$, where the dimensionless function $f_W(t) = 0.588 + 0.423\sin[(2\pi t/J) - (2\pi/3)] + 0.052\sin[4\pi t/J] + 0.096\sin[6\pi t/J]$ captured diurnal variations of wind speed, and $\bar{\zeta} \simeq 0.0574$, and $\bar{\xi}_0 \simeq 1.2\,\mathrm{mm}$ described the mean boundary layer. In this product, U_m is a random *maximum* daily wind speed with log-normal probability density function, such that the elementary probability to find U_m in the range $[U_m, U_m + \mathrm{d}U_m]$ is

$$\mathrm{d}p = \frac{\mathrm{d}U_m}{\sigma U_m\sqrt{2\pi}}\exp\left[-\frac{1}{2}\left(\frac{\ln(U_m/\bar{U}_m)}{\sigma} + \frac{\sigma}{2}\right)^2\right], \tag{B.17}$$

where $\bar{U}_m \simeq 4.8\,\mathrm{m/s}$ is the mean peak wind speed and $\sigma \simeq 0.319$ is the standard deviation of $\ln(U_m/\bar{U}_m)$.

B.4 Thermal advection-diffusion deep within a mobile dune

In the reference frame of its center of mass, the long-term motion of the dune is equivalent to a uniform sand advection at the average speed $\mathbf{U}$ directed *against* the prevailing wind. As the horizontal dashed line in Fig. 3.2 shows, this speed is comparable to the thermal diffusion velocity $u_d = \partial x/\partial t = 2\sqrt{\alpha_s \pi/Y}$ arising from a seasonal version of Eq. (3.6) in which the annual period $Y = 365\,\mathrm{days}$ is substituted for J. Therefore, to describe long-term variations of temperature deep within the dune, Eq. (3.7) must be substituted for Eq. (3.4). In general, the solution of Eq. (3.7) is subject to the rapidly-varying flux boundary condition as in Eq. (3.5). However, as section 3.3 shows, because instantaneous thermal fluctuations on the surface nearly disappear at depths $x \gtrsim 5x_J$, it is more convenient to integrate Eq. (3.7) in two matched domains, namely a surface layer and a deeper interior region.

Like a thermal boundary layer, the former is subject to Eq. (3.5) at $x = 0$, and it resides just below the surface ($0 < x \lesssim 5x_J$). There, the time scale of thermal fluctuations is short enough to ignore dune advection $\mathbf{U}$, and to assume that heat flux vanishes at $x \simeq 5x_J$. Because skies are mostly clear, the radiation forcing flux $\dot{q}''_{\text{rad}}$ on the surface layer is captured by an expression similar to Eq. (B.1), in which we substitute the local dune surface normal for $\hat{\mathbf{z}}$, invoke sand albedo and emissivity calculated in Appendix B.1, and use the instantaneous ambient temperature T from Appendix B.3 to evaluate atmospheric emission $\epsilon_a \sigma_B T^4$.

Because it depends on wind speed and direction, the convection flux imposed on the surface layer is more random. To estimate it, we simplify the Monin-Obukhov similarity with $\phi_m = \phi_h = 1$ and write $\dot{q}''_{\text{wind}} \simeq \rho c_p \kappa \bar{\zeta} U_m f_W(t)(T - T_{s_0})/\ln(z_T/\bar{\xi}_0)$. In this expression, we adopt the instantaneous ambient temperature T recorded at $z_T \simeq 2\,\mathrm{m}$ and the diurnal wind function $f_W(t)$ provided in Appendix B.3. On a daily basis, we draw a random variable U_m consistent with the log-normal wind distribution in Eq. (B.17). This formulation naturally introduces a convection coefficient $\bar{h}_{\text{wind}} = \rho c_p \kappa \bar{\zeta} \bar{U}_m/\ln(z_T/\bar{\xi}_0)$.

We use the *pdepe* toolbox in MATLAB to integrate PDE (3.7) in the surface layer along x and t, from which we extract the instantaneous surface temperature T_{s_0} over several years. The top panes of Fig. 3.6 illustrate the wide range of daily surface temperature fluctuations produced by this integration. At the toe, T_{s_0} typically peaks between 13:00 and 13:30, and it is lowest between 4:15 and 6:00 (Qatar time). On the symmetry plane of the avalanche face, these times are 12:30 to 13:00, and 4:30 to 6:30, respectively. As expected, T_{s_0} and its fluctuations depend crucially on local surface convection and seasonal orientation to solar influx.

Because Eq. (3.7) is linear in T_s, we filter wide diurnal fluctuations by averaging T_{s_0} over each day, and use the resulting $\bar{T}_{s_0}$ as a boundary condition for the dune's interior region. In general, the diurnal average surface temperature $\bar{T}_{s_0}$ can be represented by a harmonic expression like Eq. (B.16), but with different coefficients for each point on the surface,

$$\bar{T}_{s_0} \simeq \bar{\bar{T}}_{s_0} + \sum_{j=1}^{2} \Delta T_{s_{0_j}} \sin\left[2\pi j(t - t_j)/Y\right], \tag{B.18}$$

To account for the dune's complicated geometry, we integrate Eq. (3.7) in its interior region using COMSOL MULTIPHYSICS. However, because the buried probe rested near the center plane of symmetry of the dune, we treat the problem as two-dimensional (2D). For simplicity, we only distinguish three regions where to evaluate $\bar{T}_{s_0}$, namely the windward slope, the leeward avalanche face, and flats downstream of the dune. Unless wind blew against its prevailing direction, convection was substantially smaller in the nearly stagnant wake, which sheltered the avalanche and a substantial portion of the flats. Ignoring convection in those two regions, we calculate parameters of the harmonic fits in Eq. (B.18) for each region (Table B.1). We then prescribe a vanishing heat flux on a horizontal line at the far-away depth $15x_Y$, where $x_Y \equiv \sqrt{\alpha_s Y/\pi}$ is the characteristic length for annual thermal variations, extend the domain of integration a distance $\sim 20x_Y$ behind the avalanche face and $\sim 40x_Y$ upwind, make the corresponding vertical boundaries periodic, and run the numerical simulation over several annual cycles to reach a stationary periodic solution. Fig. 3.7 focuses upon a narrower domain for animating the solution.

In a region far enough below the surface for diurnal temperature fluctuations to be filtered ($x \gtrsim 0.2\,\mathrm{m}$), but close enough that the problem remains one dimensional (1D) ($x \lesssim 1\,\mathrm{m}$), it is instructive to derive a 1D solution along the depth x

normal to the dune, ignoring more complicated three-dimensional thermal interactions. In this simple view, the average daily temperature imposed at the surface diffuses along x while advecting at the speed $U_d \equiv -\mathbf{U} \cdot \hat{\mathbf{n}}_d$ projected along the outward unit normal $\hat{\mathbf{n}}_d$ of the dune's slanted surface. Such effective advection speed is positive along x beneath the leeward avalanche face and negative beneath the weakly slanted windward surface. The corresponding partial differential Eq. is then $\partial T_s/\partial t + U_d \partial T_s/\partial x = \alpha_s \partial^2 T_s/\partial x^2$, subject to the thermal forcing $T_s = \bar{T}_{s_0}$ at $x = 0$ and $T_s \to \bar{\bar{T}}_{s_0}$ as $x \to \infty$, where $\bar{T}_{s_0}$ is given by Eq. (B.18) for the surface of interest (coefficients in Table B.1).

In this problem, it is natural to make distance and time dimensionless with, respectively, x_Y and Y, such that $t^\dagger \equiv t/Y$ and $x^\dagger \equiv x/x_Y$. Because Eq. (3.7) is linear, we can write the solution in terms of its individual harmonics T_{s_j}. From Eq. (3.7) each T_{s_j} then satisfies

$$\frac{\partial T_{s_j}}{\partial t^\dagger} + 2\pi U^\dagger \frac{\partial T_{s_j}}{\partial x^\dagger} = \pi \frac{\partial^2 T_{s_j}}{\partial x^{\dagger 2}}, \tag{B.19}$$

where $U^\dagger \equiv U_d/u_d$. The solution that is always finite as $x \to +\infty$ and conforms to the surface boundary condition $T_s = \bar{T}_{s_0}$ from Eq. (B.18) is

$$T_{s_j} = \Delta T_{s_{0_j}} \exp\left[-x^\dagger/f_j\right] \sin\left[2\pi j(t^\dagger - t_j^\dagger) - x^\dagger/g_j\right], \tag{B.20}$$

where

$$f_j \equiv \left[\left(4j^2 + U^{\dagger 4}\right)^{1/4} \cos\alpha_j - U^\dagger\right]^{-1}, \tag{B.21}$$

$$g_j \equiv \left[\left(4j^2 + U^{\dagger 4}\right)^{1/4} \sin\alpha_j\right]^{-1}, \tag{B.22}$$

and

$$\alpha_j \equiv (1/2)\arctan\left(2j/U^{\dagger 2}\right). \tag{B.23}$$

Then, the 1D solution to the two-harmonic surface forcing observed in Qatar is

$$T_s = \bar{\bar{T}}_{s_0} + \sum_{j=1}^{2} \Delta T_{s_{0_j}} \exp\left[-\frac{x}{x_Y f_j}\right] \sin\left[2\pi j \frac{(t - t_j)}{Y} - \frac{x}{x_Y g_j}\right]. \tag{B.24}$$

Table B.2: Position on October 10, 2002, distance D between toe and brink, speed U derived from Google Earth satellite imagery from October 2002 to September 2009, and turn-over time D/U of barchans in the Qatar dune field (Fig. 3.2). The boldfaced line is the dune under study.

Latitude	Longitude	D (m)	U (m/yr)	$\frac{D}{U}$ (mo)
$25°02'34.7''$N	$51°19'51.9''$E	20	49	5
$25°00'22.8''$N	$51°19'40.0''$E	22	27	10
$25°02'50.8''$N	$51°19'46.8''$E	25	39	8
$25°00'40.0''$N	**$51°20'22.9''$E**	**48**	**18.4**	**31**
$25°01'22.6''$N	$51°20'36.2''$E	54	14	46
$24°59'57.0''$N	$51°19'46.6''$E	65	8.9	88
$25°01'15.4''$N	$51°19'21.5''$E	76	11	86
$25°01'48.1''$N	$51°21'02.7''$E	90	6.8	160
$25°00'50.9''$N	$51°19'54.2''$E	165	4.9	400

B.5 Dunes, sand size and mass

Positions of selected dunes shown in Fig. 3.2 are listed in Table B.2. The material density of this sand is $\rho_m \simeq 2630\,\mathrm{kg/m^3}$ and its typical solid volume fraction is $\nu \simeq 0.67$, yielding a typical bulk density $\rho_s \simeq 1760\,\mathrm{kg/m^3}$. Our colleague Jean-Luc Métayer measured the particle-size-distribution (PSD) below $500\,\mu\mathrm{m}$ of sand samples dispersed in water with sodium hexametaphosphate using a CILAS 1064 laser-diffraction analyzer. PSD results are given in section 3.2.

Our collaborator Theis Solling measured sand mineral composition with a quantitative electron microscope scanner (QEMScan) [7], and found 40.78% quartz, 36.68% calcite, 6.47% albite, 3.07% K-feldspar, 2.22% dolomite, 2.15% pores, 0.64% illite, and 0.37% zoisite by surface, with 6.08% unclassified.

B.6 Water desorption

We consider the desorption of rain water of dynamic viscosity μ_w and density ρ_w within a porous sand of solid volume fraction ν, material density ρ_m and bulk density $\rho_s = \nu\rho_m$. The evolution of the water volume fraction $\theta \simeq \rho_s\Omega/\rho_w$ is governed by Eq. (3.8) [177]. We model the limiting behavior of the hysteretic water retention curve using Eq. (3.9) [26]. To estimate its coefficients b and Ψ_a, our colleague Robert Schindelbeck laid a water-saturated puck of our Qatar sands on a saturated porous plate having an air entry potential of $10^5\,\mathrm{Pa}$ in a "Tempe cell", exerted increasingly large suction, and recorded gravimetrically θ at each step. We fitted the resulting water desorption curve to Eq. (3.9) with $b \simeq 0.39$ and $\Psi_a \simeq 2530\,\mathrm{Pa}$. Separately, we measured the saturated permeability $K_0 \simeq 2.4\ 10^{-12}\,\mathrm{m}^2$. For simplicity, we adopt the constant water viscosity $\mu_w \simeq 7\ 10^{-4}\,\mathrm{kg/m.s}$ at $310\,^\circ\mathrm{K}$, and we ignore the inclined stratigraphy described in Appendix B.5, which is likely to segregate moisture.

Although the initial water volume fraction is generally $< 1-\nu$ after desert rains, we adopt Eq. (3.9) to derive simple analytical expressions for desorption of our sands. First, to estimate the unsaturated permeability K, we substitute it in Eq. (3.10) [33]. In this case, the Richards Eq. (3.8) yields Eqs. (3.11)-(3.13).

To obtain analytical predictions for long-term moisture desorption, we assume that rain is initially accumulated at the uniform volume fraction θ_0 in a region of thickness δ_0, that evaporation or advection are negligible, and that the RH probe remains buried at the center of this region. Then, the solution of Eq. (3.11) yields the water volume fraction θ_p that it experiences [38]

$$\theta_p = \theta_0 \ \mathrm{erf}\left(\delta_0/4\sqrt{tD_{\mathrm{eff}}}\right). \tag{B.25}$$

At long times, this equation tends to

$$\theta_p \to h_R/2\sqrt{\pi t D_{\text{eff}}}, \tag{B.26}$$

where $h_R = \theta_0 \delta_0$ is rain height recorded by the pluviometer. Combining Eqs. (3.13) and (B.26), we then estimate the effective diffusion D_{eff} in a self-consistent manner,

$$D_{\text{eff}} = \Big[\frac{\Psi_a K_0 b}{\mu_w (1-\nu)}\Big]^{\frac{2}{4+b}} \Big[\frac{h_R/(1-\nu)}{\sqrt{4\pi t}}\Big]^{\frac{2(2+b)}{4+b}}, \tag{B.27}$$

and find the resulting θ_p given in Eq. (3.14)

B.7 Wetting

As we articulated in chapter 2 the relation between water volume fraction $\theta = f(\Psi)$ and suction pressure Ψ lies between two limiting curves corresponding to the wetting of initially dry sands $\theta = (1-\nu) f_w(\Psi)$ and to the desorption of initially saturated sands $\theta = (1-\nu) f_d(\Psi)$. In a porous medium with a distribution of pore sizes, because desorption begins with the rapid drainage of large pores, while wetting is initially drawn into small ones by capillarity, the two limiting curves do not coincide, but instead obey $f_w(\Psi) \leqslant f(\Psi) \leqslant f_d(\Psi)$. In general, the local state depends upon prior history of successive wetting and desorption cycles. However, because hyper-arid dunes are subject to infrequent rains followed by long dry spells, wetting often begins with nearly dry sands subject to the limiting saturation curve f_w. Without knowledge of geometrical statistics similar to Fig. 2.3, we deduce this curve from its measured desorption counterpart using the heuristic construction suggested by Parlange [161], which amounts to solving the ODE $\mathrm{d}f_w/\mathrm{d}\Psi = (f_w - f_d)/\Psi$. Substituting Eq. (3.9), its general solution is $f_w = [b/(b+1)](\Psi_a/\Psi)^{1/b} + \varpi\Psi$. The constant ϖ must vanish to guarantee that f_w is finite and positive at large Ψ. In this simple formulation, wetting is therefore described by $\theta = (1-\nu)$ for $\Psi < \Psi_w$ and

$$\theta = (1-\nu)(\Psi_w/\Psi)^{1/b} \tag{B.28}$$

otherwise. Wetting ends at the saturation potential

$$\Psi_w \equiv \Psi_a \left(\frac{b}{1+b}\right)^b < \Psi_a. \tag{B.29}$$

Once again, Richard's Eq. (3.8) can be recast as Eq. (3.11), where u_{eff} is given by Eq. (3.12). Effective diffusion is slower than in the drying case, whereby D_{eff} is given by Eq. (3.13), in which the smaller Ψ_w is now substituted for Ψ_a. Thus, at long times, the peak water volume fraction θ_p of the wetting region is well approximated by Eq. (3.14), in which Ψ_w replaces Ψ_a, and it descends at a speed u_{eff} with $\theta \simeq \theta_p$. Substituting this Eq. (3.14) in Eq. (3.12) and integrating $\mathrm{d}x_p/\mathrm{d}t = u_{\text{eff}}$ yields an analytical estimate of the time t_p required for rainwater to penetrate a dry dune to the depth x_p,

$$t_p = \left[\frac{(2-b)\mu_w(1-\nu)x_p}{(4+b)(3+2b)\rho_w g K_0}\right]^{\frac{4+b}{2-b}} \left[\frac{(1-\nu)4\pi\Psi_w K_0 b}{h_R^2\mu_w}\right]^{\frac{2+2b}{2-b}}. \tag{B.30}$$

Combining with Eq. (3.14), we find the peak value of θ at x_p,

$$\theta_p \simeq (1-\nu)\left(1+b^{-1}\right)^{\frac{b(2+2b)}{(2-b)(4+b)}} \times \left[\frac{(4+b)(3+2b)h_R^2\rho_w g}{(2-b)(1-\nu)^2 4\pi b x_p \Psi_a}\right]^{\frac{1}{2-b}}. \tag{B.31}$$

BIBLIOGRAPHY

[1] URL `http://www.theguardian.com/global-development/2011`.

[2] URL `http://worldwind.arc.nasa.gov`.

[3] A. Ahmadi, A. A. Abbasian Arani, and D. Lasseux. Numerical simulation of two-phase inertial flow in heterogeneous porous media. *Transport in Porous Media*, 84(1):177–200, 2010. doi: 10.1007/s11242-009-9491-1.

[4] Ould Ahmedou, A. Ould Mahfoudh D., P. Dupont, A. Ould el Moctar, A. Valance, and K. R. Rasmussen. Barchan dune mobility in Mauritania related to dune and interdune sand fluxes. *J. Geophys. Res*, 112:F02016:1–18, 2007.

[5] A. M. Al-Johany, M. K. Al-Sadoon, and S. A. Al-Farraj. Thermal ecology and activity of the sand fish lizard, Scincus mitranus (Scincidae) in Central Arabia. *Journal-King Saud University Science*, 11:1–16, 1999.

[6] R. I. Al-Raoush and C. S. Willson. Extraction of physically realistic pore network properties from three-dimensional synchrotron X-ray microtomography images of unconsolidated porous media systems. *Journal of Hydrology*, 300(1):44–64, 2005.

[7] J. L.. Allen, C. L. Johnson, M. J. Heumann, J. Gooley, and W. Gallin. New technology and methodology for assessing sandstone composition: A preliminary case study using a quantitative electron microscope scanner (qemscan). *Geological Society of America Special Papers*, 487:177–194, 2012. doi: 10.1130/2012.2487(11).

[8] B. Andreotti, P. Claudin, and S. Douady. Selection of dune shapes and

velocities. Part 1: Dynamics of sand, wind and barchans. *Eur. Phys. J. B*, 28:321–339, 2002.

[9] B. Andreotti, P. Claudin, and O. Pouliquen. Aeolian sand ripples: Experimental study of fully developed states. *Phys. Rev. Lett*, 96:028001, 2006. doi: 10.1103/PhysRevLett.96.028001.

[10] R. T. Armstrong and S. Berg. Interfacial velocities and capillary pressure gradients during Haines jumps. *Phys. Rev. E*, 88(4):043010, 2013.

[11] S. Assouline and D. Or. The concept of field capacity revisited: Defining intrinsic static and dynamic criteria for soil internal drainage dynamics. *Water Resources Research*, 50(6):4787–4802, 2014.

[12] T. Aste, M. Saadatfar, and T. J. Senden. Geometrical structure of disordered sphere packings. *Phys. Rev. E*, 71:061302, 2005. doi: 10.1103/PhysRevE.71.061302.

[13] J. H. Baas. A flume study on the development and equilibrium morphology of current ripples in very fine sand. *Sedimentology*, 41:185–209, 1994.

[14] R. Bagnold. The movement of desert sand. *The Geographical J*, 85:342–365, 1935.

[15] R. A. Bagnold. *The Physics of Blown Sand and Desert Dunes*. William Morrow & Co, NY, 1942.

[16] G. I. Barenblatt. Filtration of two nonmixing fluids in a homogeneous porous medium. *Fluid Dynamics*, 6(5):857–864, 1971. doi: 10.1007/BF01013869.

[17] P. C. Baveye. Comment on “Averaging theory for description of environmental problems: What have we learned?” by W. G. Gray, C. T. Miller, and B. A. Schrefler. *Advances in Water Resources*, 52(0):328 – 330, 2013. doi: http://dx.doi.org/10.1016/j.advwatres.2012.08.012.

[18] A. Bayer, H.-J. Vogel, O. Ippisch, and K. Roth. Do effective properties for unsaturated weakly layered porous media exist? An experimental study. *Hydrology and Earth System Sciences Discussions*, 2(3):1087–1105, June 2005.

[19] G. S. Beavers and D. D. Joseph. Boundary conditions at a naturally permeable wall. *J. Fluid Mech*, 30:197–207, 1967.

[20] K. Beblo, E. Rabbow, R. Rachel, H. Huber, and P. Rettberg. Tolerance of thermophilic and hyperthermophilic microorganisms to desiccation. *Extremophiles*, 13:521–531, 2009.

[21] J. Belnap. Crusts: Biological. In *Encyclopedia of Soils in the Environment*, pages 339–347. Elsevier, NY, 2004. doi: 10.1016/B0-12-348530-4/00131-4.

[22] E. Ben-Dor, N. Levin, A. Singer, A. Karnieli, O. Braun, and G. J. Kidron. Quantitative mapping of the soil rubification process on sand dunes using an airborne hyperspectral sensor. *Geoderma*, 131:1–21, 2006.

[23] S. Berg, H. Ott, S. A. Klapp, A. Schwing, R. Neiteler, N. Brussee, A. Makurat, L. Leu, F. Enzmann, J. O. Schwarz, et al. Real-time 3D imaging of Haines jumps in porous media flow. *Proceedings of the National Academy of Sciences*, 110(10):3755–3759, 2013.

[24] G. Bertotti. *Hysteresis in Magnetism: for Physicists, Materials scientists, and Engineers*. Academic Press, San Diego, CA, 1998.

[25] K. Binder and A. P. Young. Spin glasses: Experimental facts, theoretical concepts, and open questions. *Reviews of Modern physics*, 58(4):801, 1986.

[26] M. Bittelli, F. Ventura, G. S. Campbell, R. L. Snyder, F. Gallegati, and P. Rossi Pisa. Coupling of heat, water vapor, and liquid water fluxes to compute evaporation in bare soils. *J. Hydrology*, 362:191–205, 2008.

[27] G. Blois, J. L. Best, G. H. Sambrook Smith, and R. J. Hardy. Effect of bed permeability and hyporheic flow on turbulent flow over bed forms. *Geophys. Res. Lett*, 41:6435–6442, 2014. doi: 10.1002/2014GL060906.

[28] H. A. Bokhary. Mycoflora of desert sand dunes of Riyahd region, Saudi Arabia. *J. King Saud Univ. - Science*, 10:15–29, 1998.

[29] A. J. Boulton, S. Findlay, P. Marmonier, E. H. Stanley, and H. M. Valett. The functional significance of the hyporheic zone in streams and rivers. *Ann. Rev. of Ecology and Systematics*, 29:59–81, 1998.

[30] M. A. Bowker, J. Belnap, V. B. Chaudhary, and N. C. Johnson. Revisiting classic water erosion models in drylands: The strong impact of biological soils crusts. *Soil Biology and Chemistry*, 40:2309–2316, 2008.

[31] C. Bristow, S. Bailey, and N. Lancaster. The sedimentary structure of linear sand dunes. *Nature*, 406:56–59, 2000.

[32] R. Brooks and A. Corey. Hydraulic properties of porous media. *Colorado State University Hydrology Paper*, 3:27, 1964.

[33] R. H. Brooks and A. T. Corey. Hydraulic properties of porous media. *Colorado State University Hydrology Paper*, 3:27, 1964.

[34] J. Buckles, T. J. Hanratty, and R. J. Adrian. Turbulent flow over large-amplitude wavy surfaces. *J. Fluid Mech*, 140:27–44, 1984.

[35] N. E. Burdine. Relative permeability calculations from pore size distribution data. *AIME Petroleum Trans.*, 198:73–78, 1953.

[36] M. B. Cardenas and J. L. Wilson. Dunes, turbulent eddies, and interfacial exchange with permeable sediments. *Water Resour. Res*, 43:W08412, 2007. doi: 10.1029/2006WR005787.

[37] C. S. Carroll, M. Y. Louge, and B. Turnbull. Frontal dynamics of powder snow avalanches. *J. Geophys. Res*, 118:913–924, 2013. doi: 10.1002/jgrf.20068.

[38] H. S. Carslaw and J. C. Jaeger. *Conduction of Heat in Solids*. Clarendon Press, Oxford, second edition, 1959. pp. 54-65.

[39] H. C. Chan, W. C. Huang, J. M. Leu, and C. J. Lai. Macroscopic modeling of turbulent flow over a porous medium. *Int. J. Heat and Fluid Flow*, 28: 1157–1166, 2007. doi: 10.1016/j.ijheatfluidflow.2006.10.005.

[40] H. C. Chan, J. M. Leu, C. J. Lai, and Y. Jia. Turbulent flow over a channel with fluid-saturated porous bed. *J. Hydraul. Eng*, 133:610–617, 2007. doi: 10.1061/ASCE0733-94292007133:6610.

[41] D. Chandler. *Introduction to Modern Statistical Mechanics*. Oxford Univ. Press, Oxford, UK, 1987.

[42] R. Chandler, J. Koplik, K. Lerman, and J. F. Willemsen. Capillary displacement and percolation in porous media. *J. Fluid Mech.*, 119:249–267, 1982.

[43] F. Charru, B. Andreotti, and P. Claudin. Sand ripples and dunes. *Annu. Rev. Fluid Mech*, 45:469–93, 2013.

[44] S. X. Chen. Thermal conductivity of sands. *Heat Mass Transfer*, 44:1241–1246, 2008.

[45] M. P. Ciamarra, R. Pastore, M. Nicodemi, and A. Coniglio. Jamming phase diagram for frictional particles. *Phys. Rev. E*, 84:041308, 2011. doi: 10.1103/PhysRevE.84.041308.

[46] A. Cihan, J. Birkholzer, T. H. Illangasekare, and Q. Zhou. A modeling approach to represent hysteresis in capillary pressure saturation relationship based on fluid connectivity in void space. *Water Resources Research*, 50:119–131, 2014. doi: 10.1002/2013WR014280.

[47] M. Creyssels, P. Dupont, A. Ould el Moctar, A. Valance, I. Cantat, J. T. Jenkins, J. m. Pasini, and K. R. Rasmussen. Saltating particles in a turbulent boundary layer: experiment and theory. *J. Fluid Mech*, 625:47–74, 2009. doi: 10.1017/S0022112008005491.

[48] Z. Csahók, C. Misbah, F. Rioual, and A. Valance. Dynamics of aeolian sand ripples. *Eur. Phys. J. E*, 3:71–86, 2000.

[49] M. de Berg, O. Cheong, M. van Kreveld, and M. Overmars. Delaunay triangulations. *Computational Geometry: Algorithms and Applications*, pages 191–218, 2008.

[50] P. de Félice. Etude des échanges de chaleur entre l'air et le sol sur deux sols de nature différente. *Geoph. Biokl., Ser. B*, 16:70–80, 1968.

[51] J. T. DeJong, M. B. Fritzges, and K. Nüsslein. Microbially induced cementation to control sand response to undrained shear. *Journal of Geotechnical and Geoenvironmental Engineering*, 132(11):1381–1392, 2006.

[52] O. Durán and H. Herrmann. Vegetation against dune mobility. *Phys. Rev. Lett*, 97:188001, 2006.

[53] J. H. Dymond and H. A. Øye. Viscosity of selectd liquid n-alkanes. *J. Phys. Chem. Ref. Data*, 23(1):41–53, 1994.

[54] S. F. Edwards and P. W. Anderson. Theory of spin glasses. *Journal of Physics F: Metal Physics*, 5(5):965, 1975.

[55] S. F. Edwards and R. B. S. Oakeshott. Theory of powders. *Physica A*, 157: 1080–1090, 1989. doi: 10.1016/0378-4371(89)90034-4.

[56] A. H. Elliott and N. H. Brooks. Transfer of nonsorbing solutes to a streambed with bed forms: laboratory experiments. *Water Resour. Res*, 33:137–151, 1997.

[57] J. A. Enderby. The domain model of hysteresis. Part 1: Independent domains. *Trans. Faraday Soc.*, 51:835–848, 1955.

[58] F. Engelund and J. Fredsøe. Sediment ripples and dunes. *Ann. Rev. Fluid Mech*, 14:13–37, 1982.

[59] D. H. Everett. A general approach to hysteresis. Part 3: A formal treatment of the independent domain model of hysteresis. *Trans. Faraday Soc.*, 50: 1077–1096, 1954.

[60] D. H. Everett. A general approach to hysteresis. Part 4: An alternative formulation of the domain model. *Trans. Faraday Soc.*, 51:1551–1557, 1955.

[61] D. H. Everett and F. W. Smith. A general approach to hysteresis. Part 2: Development of the domain theory. *Trans. Faraday Soc.*, 50:187–197, 1954.

[62] D. H. Everett and W. I. Whitton. A general approach to hysteresis. *Trans. Faraday Soc.*, 48:749–757, 1952.

[63] B. S. Everitt. *Cambridge Dictionary of Statistics*. Cambridge University Press, Cambridge, U.K, third edition, 2006.

[64] R. P. Ewing and S. C. Gupta. Percolation and permeability in partially structured networks. *Water Resources Research*, 29(9):3179–3188, 1993.

[65] F. Falk. Ginzburg-Landau theory of static domain walls in shape-memory alloys. *Zeitschrift für Physik B Condensed Matter*, 51(2):177–185, 1983.

[66] H. Y. Fang, Q. G. Cai, H. Chen, and Q. Y. Li. Mechanism of formation of physical soil crust in desert soils treated with straw checkerboards. *Soil & Tillage Research*, 93:222–230, 2007.

[67] I. Fatt, H. Dykstra, et al. Relative permeability studies. *Journal of Petroleum Technology*, 3(09):249–256, 1951.

[68] A. Ferrari, J. Jimenez-Martinez, T. Le Borgne, Y. Méheust, and I. Lunati. Challenges in modeling unstable two-phase flow experiments in porous micromodels. *Water Resources Research*, 2015. doi: 10.1002/2014WR016384.

[69] R. P. Feynman, R. B. Leighton, and M. Sands. The Feynman Lectures on Physics. Vol. ii: Mainly Electromagnetism and Matter, 1964.

[70] S. M. Forster. Microbial aggregation of sand in an embryo dune system. *Soil Biol. Biochem*, 11:537–543, 1979.

[71] S. M. Forster and T. H. Nicolson. Aggregation of sand from a maritime embryo sand dune by microorganisms and higher plants. *Soil Biol. Biochem*, 13:199–203, 1981.

[72] D. L. Foster, A. J. Bowen, R. A. Holman, and P. Natoo. Field evidence of pressure gradient induced incipient motion. *J. Geophys. Res*, 111:C05004, 2006. doi: 10.1029/2004JC002863.

[73] A. Fourrière. *River morphodynamics : Width selection, ripples and dunes*. PhD thesis, Université Paris Diderot, Paris, France, 2009.

[74] A. Fourrière, P. Claudin, and B. Andreotti. Bedforms in a turbulent stream: formation of ripples by primary linear instability and of dunes by nonlinear pattern coarsening. *J. Fluid Mech*, 649:287–328, 2010. doi: 10.1017/S0022112009993466.

[75] X. Frank and P. Perré. Droplet spreading on a porous surface: A lattice Boltzmann study. *Phys. Fluids*, 24:042101, 1981. doi: 10.1063/1.3701996.

[76] X. Frank and P. Perré. Droplet spreading on a porous surface: A Lattice Boltzmann study. *Phys. Fluids*, 24(4):042101, 2012. doi: http://dx.doi.org/10.1063/1.3701996.

[77] N. Fraysse, H. Thomé, and L. Petit. Humidity effects on the stability of a sandpile. *Eur. Phys. J. B*, 11:615–619, 1999.

[78] K. A. Frederick and T. J. Hanratty. Velocity measurements for a turbulent nonseparated flow over solid waves. *Exp. Fluids*, 6:477–486, 1988.

[79] J. S. Fries and G. L. Taghon. Particle fluxes into permeable sediments: Comparison of mechanisms mediating deposition. *Journal of Hydraulic Engineering*, 136(4):214–221, 2010.

[80] L. Furuberg, K. J. Måløy, and J. Feder. Intermittent behavior in slow drainage. *Phys. Rev. E*, 53:966–977, Jan 1996. doi: 10.1103/PhysRevE.53.966.

[81] L. D. Gelb, K. E. Gubbins, R. Radhakrishnan, and M. Sliwinska-Bartkowiak. Phase separation in confined systems. *Reports on Progress in Physics*, 62(12):1573, 1999.

[82] B. Ghanbarian, A. G. Hunt, R. P. Ewing, and M. Sahimi. Tortuosity in porous media: A critical review. *Soil Science Society of America Journal*, 77 (5):1461–1477, 2013.

[83] J. A. Gili and E. E. Alonso. Microstructural deformation mechanisms of unsaturated granular soils. *Int. J. for Numer. & Anal. Meth. in Geomechanics*, 26(5):433–468, 2002.

[84] M. Gommeaux, M. Barakat, G. Montagnac, R. Christen, F. Guyot, and T. Heulin. Mineral and bacterial diversities of desert sand grains from South-East Morocco. *Geomicrobiology J*, 27:76–92, 2010. doi: 10.1080/01490450903393066.

[85] W. Gong, P. A. Taylor, and A. Dörnbrack. Turbulent boundary-layer flow over fixed aerodynamically rough two-dimensional sinusoidal wave. *J. Fluid Mech*, 312:1–31, 1996.

[86] D. Goossens. The effect of surface curvature on the deposition of loess: A physical model. *Catena*, 15:179–194, 1988.

[87] W. D. Grant. Life at low water activity. *Phil. Trans. R. Soc. Lond. B*, 359: 249–267, 2004. doi: 10.1098/rstb.2004.1502.

[88] J.-P. Gras, J.-Y. Delenne, F. Souli, and M.S. El Youssoufi. DEM and experimental analysis of the water retention curve in polydisperse granular media. *Powder Technology*, 208(2):296 – 300, 2011. doi: http://dx.doi.org/10.1016/j.powtec.2010.08.019.

[89] J. M. N. T. Gray and K. Hutter. Pattern formation in granular avalanches. *Continuum Mech. Thermodyn*, 9:341–345, 1997.

[90] W. G. Gray and C. T. Miller. Thermodynamically constrained averaging theory approach for modeling flow and transport phenomena in porous medium systems: 1. Motivation and overview. *Advances in Water Resources*, 28(2):161 – 180, 2005. doi: http://dx.doi.org/10.1016/j.advwatres.2004.09.005.

[91] W. G. Gray and C. T. Miller. TCAT analysis of capillary pressure in non-equilibrium, two-fluid-phase, porous medium systems. *Advances in Water Resources*, 34:770–778, 2011. doi: 10.1016/j.advwatres.2011.04.001.

[92] W. G. Gray, C. T. Miller, and B. A. Schrefler. Averaging theory for description of environmental problems: What have we learned? *Advances in Water Resources*, 51(0):123 – 138, 2013. doi: http://dx.doi.org/10.1016/j.advwatres.2011.12.005. 35th Year Anniversary Issue.

[93] W. G. Gray, C. T. Miller, and B. A. Schrefler. Response to comment on averaging theory for description of environmental problems: What have we learned? *Advances in Water Resources*, 52:331 – 333, 2013. doi: 10.1016/j.advwatres.2012.10.006.

[94] C. M. Gribble, G. P. Matthews, G. M. Laudone, A. Turner, C. J. Ridgway,

J. Schoelkopf, and P. A. C. Gane. Porometry, porosimetry, image analysis and void network modelling in the study of the pore-level properties of filters. *Chemical Engineering Science*, 66(16):3701–3709, 2011.

[95] A. K. Gunstensen, D. H. Rothman, S. Zaleski, and G. Zanetti. Lattice Boltzmann model of immiscible fluids. *Phys. Rev. A*, 43(8):4320, 1991.

[96] A. Günther and P. R. von Rohr. Large-scale structures in a developed flow over a wavy wall. *J. Fluid Mech*, 478:257–285, 2003.

[97] W. B. Haines. Studies in the physical properties of soil. V. The hysteresis effect in capillary properties, and the modes of moisture distribution associated therewith. *The Journal of Agricultural Science*, 20(01):97–116, 1930.

[98] D. S. Henn and R. I. Sykes. Large-eddy simulation of flow over wavy surfaces. *J. Fluid Mech*, 383:75–112, 1999.

[99] S. Herminghaus. Dynamics of wet granular matter. *Advances in Physics*, 54:221–261, 2005. doi: 10.1080/00018730500167855.

[100] P. Hersen. On the crescentic shape of barchan dunes. *Eur. Phys. J. B*, 37: 507–514, 2004.

[101] P. Hersen, K. H. Andersen, H. Elbelrhiti, B. Andreotti, P. Claudin, and S. Douady. Corridors of barchan dunes: Stability and size selection. *Phys. Rev. E*, 69:011304, 2004.

[102] T. Heulin, M. Barakat, R. Christen, M. Lesourd, L. Sutra, G. De Luca, and W. Achouak. *Ramlibacter tataouinensis* gen. nov., sp. nov., and *Ramlibacter henchirensis* sp. nov., cyst-producing bacteria isolated from subdesert soil in Tunisia. *Int. J. Syst. Evol. Microbiol.*, 53:589–594, 2003.

[103] T. Heulin, G. De Luca, M. Barakat, A. de Groot, L. Blanchard, P. Ortet, and W. Achouak. Bacterial adaptation to hot and dry deserts. In H. Stan-Lotter et al., editor, *Adaptation of Microbial Life to Environmental Extremes*, pages 69–85. Springer-Verlag, Wien, 2012.

[104] J. O. Hinze. Turbulence. *second ed., Mc-Graw-Hill, NY, p.*, 673, 1975.

[105] T. D. Ho, A. Valance, P. Dupont, and A. Ould El-Moctar. Scaling laws in aeolian sand transport. *Phys. Rev. Lett*, 106:094501, 2011.

[106] J. J. Hopfield. Neural networks and physical systems with emergent collective computational abilities. *Proceedings of the national academy of sciences*, 79(8):2554–2558, 1982.

[107] C. Hu, Y. Liu, L. Song, and D. Zhang. Effect of desert soil algae on the stabilization of fine sands. *J. of Applied Phycology*, 14:281–292, 2002.

[108] C. Hu, Y. Liu, B. S. Paulsen, D. Petersen, and D. Klaveness. Extracellular carbohydrate polymers from five desert soil algae with different cohesion in the stabilization of fine sand grain. *Carbohydrate Polymers*, 54:33–42, 2003.

[109] M. Huettel, P. L. M. Cook, F. Janssen, G. Lavik, and J. J. Middelburg. Transport and degradation of a dinoflagellate bloom in permeable sublittoral sediment. *Mar. Ecol. Prog. Ser*, 340:139–153, 2007.

[110] R. M. Iverson. Regulation of landslide motion by dilatancy and pore pressure feedback. *J. Geophys. Res*, 110:F02015, 2005. doi: 10.1029/2004JF000268.

[111] R. M. Iverson, M. E. Reid, M. Logan, R. G. LaHusen, J. W. Godt, and J. P. Griswold. Positive feedback and momentum growth during debris-flow

entrainment of wet bed sediment. *Nature Geoscience*, 4:116–121, 2011. doi: 10.1038/ngeo1040.

[112] S. M. Iveson, J. A. Beathe, and N. W. Page. The dynamic strength of partially saturated powder compacts: the effect of liquid properties. *Powder Tech.*, 127:149–161, 2002.

[113] M. Iwamatsu and K. Horii. Capillary condensation and adhesion of two wetter surfaces. *J. Colloid and Interface Science*, 182:400–406, 1996.

[114] P. S. Jackson and J. C. R. Hunt. Turbulent wind flow over a low hill. *Quart. J. R. Met. Soc*, 101:929–955, 1975.

[115] H. Y. Jennings. The effect of temperature and pressure on the interfacial tension of benzene-water and normal decane-water. *Journal of Colloid and Interface Science*, 24(3):323–329, 1967.

[116] I. P. Jones. Low reynolds number flow past a porous spherical shell. *Proc. Camb. Philos. Soc*, 73:231–238, 1973.

[117] A. Kaestner, E. Lehmann, and M. Stampanoni. Imaging and image processing in porous media research. *Advances in Water Resources*, 31(9):1174–1187, 2008.

[118] G. Katata, H. Nagai, H. Ueda, N. Agam, and P. R. Berliner. Development of a land surface model including evaporation and adsorption processes in the soil for the land-air exchange in arid regions. *J. HydroMet*, 8:1307–1324, 2007.

[119] J. M. Kendall. The turbulent boundary layer over a wall with progressive surface waves. *J . Fluid Mech*, 41:259–281, 1970.

[120] G. J. Kidron, I. Herrnstadt, and E. Barzilay. The role of dew as a moisture source for sand microbiotic crusts in the Negev Desert, Israel. *J. of Arid Environments*, 52:517–533, 2002. doi: 10.1006/jare.2002.1014.

[121] E. Kierlik and M. L. Rosinberg. Density-functional theory for inhomogeneous fluids: adsorption of binary mixtures. *Phys. Rev. A*, 44(8):5025, 1991.

[122] H. T. Kim, S. J. Kline, and W. C. Reynolds. The production of turbulence near a smooth wall in a turbulent boundary layer. *J. Fluid Mech*, 50:133–160, 1971.

[123] C. Kittel and J. K. Galt. Ferromagnetic domain theory. *Solid State Physics*, 3:437–564, 1956.

[124] T. Kobayashi, A. Matsuda, M. Kamichika, and T. Sato. Studies of the dry surface layer in a sand dune field (1) Modeling of the dry surface layer of sand under isothermal steady conditions. *J. Agr. Met*, 42:113–118, 1986.

[125] T. Kobayashi, A. Matsuda, M. Kamichika, and Y. Yamamura. Why the thickness of the dry surface layer in sand dune fields exhibits a diurnal variation? *J. Agr. Met*, 47:3–9, 1991.

[126] K. Kroy, G. Sauermann, and H. J. Herrmann. Minimal model for sand dunes. *Phys. Rev. Lett*, 88:054301, 2002.

[127] J. D Kuzan, T. J. Hanratty, and R. J. Adrian. Turbulent flows with incipient separation over solid waves. *Exp. in Fluids*, 7:88–98, 1989.

[128] R. G. Larson, L. E. Scriven, and H. T. Davis. Percolation theory of residual phases in porous media. *Nature*, 268:409–413, 1977. doi: 10.1038/268409a0.

[129] R. G. Larson, L. E. Scriven, and H. T. Davis. Percolation theory of two phase flow in porous media. *Chemical Engineering Science*, 36(1):57–73, 1981.

[130] C. Lastoskie, K. E. Gubbins, and N. Quirke. Pore size distribution analysis of microporous carbons: a density functional theory approach. *J. Phys. Chem.*, 97(18):4786–4796, 1993.

[131] T. D. Lee and C. N. Yang. Statistical theory of equations of state and phase transitions. ii. Lattice gas and Ising model. *Phys. Rev.*, 87(3):410, 1952.

[132] S. Leonardi, P. Orlandi, and R. A. Antonia. Properties of d- and k-type roughness in a turbulent channel flow. *Phys. Fluids*, 19:125101, 2007. doi: 10.1063/1.2821908.

[133] N. Levin, G. J. Kidron, and E. Ben-Dor. Surface properties of stabilizing coastal dunes: combining spectral and field analyses. *Sedimentology*, 54: 771–788, 2007.

[134] I. Livingstone, G. F. Wiggs, and C. M. Weaver. Geomorphology of desert sand dunes: A review of recent progress. *Earth-Science Rev*, 80:239–257, 2007.

[135] P. N. Loezos, P. Costamagna, and S. Sundaresan. The role of contact stresses and wall friction on fluidization. *Chem. Eng. Sci*, 57:5123–5141, 2002.

[136] M. Y. Louge, A. Valance, H. Mint Babah, J. c. Moreau-Trouvé, A. Ould el Moctar, and D. Ould Ahmedou. Seepage-induced penetration of humidity and dust beneath ripples and dunes. *J. Geophys. Res*, 115:F02002:1–14, 2010.

[137] M. Y. Louge, A. Valance, A. Ould el Moctar, and P. Dupont. Packing variations on a ripple of nearly monodisperse dry sand. *J. Geophys. Res*, 115: F02001, 2010. doi: 10.1029/2009JF001384.

[138] M. Y. Louge, C. S. Carroll, and B. Turnbull. Role of pore pressure gradients in sustaining frontal particle entrainment in eruption currents: The case of powder snow avalanches. *J. Geophys. Res*, 116:F04030, 2011. doi: 10.1029/2011JF002065.

[139] M. Y. Louge, A. Valance, A O. el Moctar, J. Xu, A. G. Hay, and R. Richer. Temperature and humidity within a mobile barchan sand dune, implications for microbial survival. *Journal of Geophysical Research: Earth Surface*, 118(4):2392–2405, 2013.

[140] C. Manes, D. Pokrajac, I. McEwan, and V. Nikora. Turbulent structure of open channel flows over permeable and impermeable beds: a comparative study. *Phys. Fluids*, 21:125109, 2009. doi: 10.1063/1.3276292.

[141] C. Manes, D. Poggi, and L. Ridolphi. Turbulent boundary layers over permeable walls: Scaling and near-wall structure. *J. Fluid Mech*, 687:141–170, 2011. doi: 10.1017/jfm.2011.329.

[142] E. Manukyan and L. Prigozhin. Formation of aeolian ripples and sand sorting. *Phys. Rev. E*, 79:031303, 2009. doi: 10.1103/PhysRevE.79.031303.

[143] T. G. Mason, A. J. Levine, D. Ertaş, and T. C. Halsey. Critical angle of wet sandpiles. *Phys. Rev. E*, 60:R5044–R5047, 1999.

[144] E. D. McKee et al. A study of global sand seas. *US Geological Survey, Professional Paper*, (P-1052), 1980.

[145] F. J. R. Meysman, O. S. Galaktionov, P. L. M. Cook, F. Janssen, and M. Huettel. Quantifying biologically and physically induced flow and tracer dynamics in permeable sediments. *Biogeosciences*, 4:627–646, 2007.

[146] N. Mitarai and F. Nori. Wet granular materials. *Advances in Phys*, 55:1–45, 2006.

[147] F. Moebius and D. Or. Pore scale dynamics underlying the motion of drainage fronts in porous media. *Water Resources Research*, 50(11):8441–8457, 2014.

[148] M. Mooney. The viscosity of a concentrated suspension of spherical particles. *J. of Colloid Sci*, 6:162–170, 1951.

[149] Y. Mualem. A conceptual model of hysteresis. *Water Resources Research*, 10(3):514–520, 1974.

[150] Y. Mualem. Hysteretical models for prediction of the hydraulic conductivity of unsaturated porous media. *Water Resources Research*, 12(6):1248–1254, 1976.

[151] Y. Mualem. A new model for predicting the hydraulic conductivity of unsaturated porous media. *Water Resources Research*, 12(3):513–522, 1976.

[152] Y. Mualem. Extension of the similarity hypothesis used for modeling the soil water characteristics. *Water Resources Research*, 13(4):773–780, 1977.

[153] Y. Mualem and A. Beriozkin. General scaling rules of the hysteretic water retention function based on Mualem's domain theory. *European J. of Soil Science*, 60(4):652–661, 2009.

[154] Y. Mualem and G. Dagan. A dependent domain model of capillary hysteresis. *Water Resources Research*, 11(3):452–460, 1975.

[155] J. Mugnier and G. Jung. Survival of bacteria and fungi in relation to water activity and the solvent properties of water in biopolymer gels. *Applied & Env. Microbiol*, 50:108–114, 1985.

[156] D. A. Nield. The Beavers-Joseph boundary condition and related matters: A historical and critical note. *Transp. Porous Med*, 78:537–540, 2009. doi: 10.1007/s11242-009-9344-y.

[157] M. H. O'Leary. Carbon isotopes in photosynthesis. *BioScience*, 38:328–336, 1988.

[158] J. Olsthoorn, M. Stastna, and N. Soontiens. Fluid circulation and seepage in lake sediment due to propagating and trapped internal waves. *Water Resour. Res*, 48:W11520, 2012. doi: 10.1029/2012WR012552.

[159] F. M. Orr, L. E. Scriven, and A. P. Rivas. Pendular rings between solids: meniscus properties and capillary force. *Journal of Fluid Mechanics*, 67(04): 723–742, 1975.

[160] A. I. Packman, M. Salehin, and M. Zaramella. Hyporheic exchange with gravel beds: Basic hydrodynamic interactions and bedform-induced advective flows. *J. Hydraul. Eng*, 130:647–656, 2004. doi: 10.1061/(ASCE)0733-9429(2004)130:7(647).

[161] J.-Y. Parlange. Capillary hysteresis and the relationship between drying and wetting curves. *Water Resources Research*, 12:224–228, 1976.

[162] A. E. Perry, W. H. Schofield, and P. N. Joubert. Rough wall turbulent boundary layers. *J. Fluid Mech*, 37:383–413, 1969.

[163] A. Peters. Simple consistent models for water retention and hydraulic conductivity in the complete moisture range. *Water Resources Research*, 49: 6765–6780, 2013. doi: 10.1002/wrcr.20548.

[164] L. Pisani. Simple expression for the tortuosity of porous media. *Transport in Porous Media*, 88(2):193–203, 2011.

[165] V. B. Ponizovskaya, A. B. Antropova, V. L. Mokeeva, E. N. Bilanenko, and L. N. Chekunova. Effect of water activity and relative air humidity on the growth of *Penicillium chrysogenum* Thom, *Aspergillus repens* (Corda) Sacc., and *Trichoderma viride* Pers. isolated from living spaces. *Microbiology*, 80: 378–385, 2011.

[166] A. Poulovassilis. Hysteresis of pore water in granular porous bodies. *Soil Science*, 109(1):5–12, 1970.

[167] A. J. Prata. A new long-wave formula for estimating downward clear-sky radiation at the surface. *Q. J. R. Meteorol. Soc*, 122:1127–1151, 1996.

[168] F. Preisach. Über die magnetische Nachwirkung. *Zeitschrift für Physik*, 94 (5-6):277–302, 1935.

[169] P. Prinos, D. Sofialidis, and E. Keramaris. Turbulent flow over and within a porous bed. *J. Hydraul. Eng*, 129:720–733, 2003. doi: 10.1061/(ASCE)0733-9429(2003)129:9(720).

[170] K. Pye and H. Tsoar. The mechanics and geological implications of dust transport and deposition in deserts with particular reference to loess formation and dune sand diagenesis in the Northern Negev, Israel, in: Desert sediments: Ancient and modern. In L. Frostick and I. Reid, editors, *Geological Society Special Publication*, pages 139–156. 35, 1987.

[171] Z. Qin, P. Berliner, and A. Karnieli. Micrometeorological modeling to understand the thermal anomaly in the sand dunes across the Israel-Egypt border. *J. of Arid Environments*, 51:281–318, 2002.

[172] K. R. Rasmussen, J. D. Iversen, and P. Rautahemio. Saltation and wind-flow interaction in a variable slope wind tunnel. *Geomorphology*, 17:19–28, 1996.

[173] S. Ravi, T. M. Zobeck, T. M. Over, G. S. Okin, and P. D'Odorico. On the effect of moisture bonding forces in air-dry soils on threshold friction velocity of wind erosion. *Sedimentology*, pages 1–13, 2006. doi: 10.1111/j.1365-3091.2006.00775.x.

[174] N. Requena, E. Perez-Solis, C. Azcón-Aguilar, P. Jeffries, and J. m. Barea. Management of indigenous plant-microbe symbioses aids restoration of desertified ecosystems. *Appl. Environ. Microbiol*, 67:495–498, 2001.

[175] R. J. Ribando. The cornell environmental wind tunnel. Master's thesis, Cornell University, 1974.

[176] P. Richard. Personal communication. 2014.

[177] L. A. Richards. *Capillary conduction of liquids through porous mediums*. PhD thesis, Cornell University, 1931.

[178] L. A. Richards. Capillary conduction of liquids through porous mediums. *Journal of Applied Physics*, 1(5):318–333, 1931.

[179] O. Roche, S. Montserrat, Y. Ni no, and A. Tamburrino. Pore fluid pressure and internal kinematics of gravitational laboratory air-particle flows: Insights into the emplacement dynamics of pyroclastic flows. *J. Geophys. Res*, 115:B09206, 2010. doi: 10.1029/2009JB007133.

[180] D. H. Rothman and J. M. Keller. Immiscible cellular-automaton fluids. *Journal of Statistical Physics*, 52(3-4):1119–1127, 1988.

[181] J. Rotnicka. Aeolian vertical mass flux profiles above dry and moist sandy beach surfaces. *Geomorphology*, 187:27–37, 2013.

[182] P. G. Saffman. On the boundary condition at the interface of a porous medium. *Stud. Appl. Math*, 1:93–101, 1971.

[183] G. Sauermann, K. Kroy, and H. J. Herrmann. Continuum saltation model for sand dunes. *Phys. Rev. E*, 64:031305, 2001.

[184] M. G. Schaap, F. J. Leij, and M. T. van Genuchten. Neural network analysis for hierarchical prediction of soil hydraulic properties. *Soil Science Society of America Journal*, 62(4):847–855, 1998.

[185] M. Scheel, R. Seemann, M. Brinkmann, M Di M., A. Sheppard, and S. Herminghaus. Liquid distribution and cohesion in wet granular assemblies beyond the capillary bridge regime. *Journal of Physics: Condensed Matter*, 20(49):494236, 2008.

[186] J. M. H. M. Scheutjens and G. J. Fleer. Statistical theory of the adsorption of interacting chain molecules. 1. Partition function, segment density distribution, and adsorption isotherms. *Journal of Physical Chemistry*, 83(12): 1619–1635, 1979.

[187] S. Schlüter, A. Sheppard, K. Brown, and D. Wildenschild. Image processing of multiphase images obtained via X-ray microtomography: A review. *Water Resources Research*, 50(4):3615–3639, 2014.

[188] L. Scholtès, B. Chareyre, F. Nicot, and F. Darve. Micromechanics of granular materials with capillary effects. *International Journal of Engineering Science*, 47(1):64–75, 2009.

[189] V. Schwämmle and H. Herrmann. A model of barchan dunes including lateral shear stress. *Eur. Phys. J. E*, 16:57–65, 2005.

[190] J. P. Sethna, K. Dahmen, S. Kartha, J. A. Krumhansl, B. W. Roberts, and J. D. Shore. Hysteresis and hierarchies: Dynamics of disorder-driven first-order phase transformations. *Phys. Rev. Lett.*, 70(21):3347, 1993.

[191] E. Shahraeeni and D. Or. Pore-scale analysis of evaporation and condensation dynamics in porous media. *Langmuir*, 26:13924–13936, 2010.

[192] E. Shahraeeni and D. Or. Pore-scale analysis of evaporation and condensation dynamics in porous media. *Langmuir*, 26:13924–13936, 2010. doi: 10.1021/la101596y.

[193] S. Shang, R. N. Horne, and H. J. Ramey. Water vapor adsorption on geothermal reservoir rocks. *Geothermics*, 24:523–540, 1995.

[194] Y. Shao and H. Lu. A simple expression for wind erosion threshold friction velocity. *J. Geophys. Res*, 105:22437–22443, 2000.

[195] D. J. Sherman and E. J. Farrell. Aerodynamic roughness lengths over movable beds: comparison of wind tunnel and field data. *J. Geophys. Res*, 113: F02S08, 2008. doi: 10.1029/2007JF000784.

[196] A. Shields. Anwendung der aehnlichkeitsmechanik und der turbulenzforschung auf die geschiebebewegung (application of similarity principles and turbulence research to bedload motion). *Mitteilungen der Preußischen Versuchsanstalt für Wasserbau*, 26:1–26, 1936.

[197] J. F. A. Sleath. Conditions for plug formation in oscillatory flow. *Continental Shelf Res*, 19:1643–1664, 1999.

[198] M. Sophocleous. Interactions between groundwater and surface water: the state of the science. *Hydrogeology J*, 10:52–67, 2002.

[199] G. Sposito and S.-Y. Chu. The statistical mechanical theory of groundwater flow. *Water Resources Research*, 17(4):885–892, 1981. doi: 10.1029/WR017i004p00885.

[200] G. Sterk. Causes, consequences and control of wind erosion in Sahelian Africa: A review. *Land Degrad. Develop*, 14:95–108, 2003.

[201] J. C. Stutz, R. Copeman, C. A. Martin, and J. B. Morton. Patterns of species composition and distribution of arbuscular mycorrhizal fungi in arid regions of southwestern North America and Namibia, Africa. *Can. J. Bot*, 78:237–245, 2000.

[202] B. M. Sumer and M. Bakioglu. On the formation of ripples on an erodible bed. *Journal of Fluid Mechanics*, 144:177–190, 1984.

[203] L. Susskind. Personal communication. 2010.

[204] J. Taine, F. Bellet, V. Leroy, and E. Iacona. Generalized radiative transfer equation for porous medium upscaling: Application to the radiative fourier law. *Int. J. of Heat and Mass Transfer*, 53:4071–4081, 2010.

[205] W. F. Tanner. Ripple mark indices and their uses. *Sedimentology*, 9:89–104, 1967.

[206] P. Tegzes, T. Vicsek, and P. Schiffer. Development of correlations in the dynamics of wet granular avalanches. *Phys. Rev. E*, 67:51303–1–17, 2003.

[207] C. B. Thorsness, P. E. Morrisroe, and T. J. Hanratty. A comparison of linear theory with measurements of the variation of shear stress along a solid wave. *Chem. Eng. Sci*, 33:579–592, 1978.

[208] J. H. Titus, P. J. Titus, R. S. Novak, and S. D. Smith. Arbuscular mycorrhizae of Mojave desert plants. *Western North American Naturalist*, 62: 327–334, 2002.

[209] J. Tölke. Lattice Boltzmann simulations of binary fluid flow through porous media. *Phil. Trans. Roy. Soc. London A: Mathematical, Physical and Engineering Sciences*, 360(1792):535–545, 2002.

[210] G. C. Topp. Soil-water hysteresis measured in a sandy loam and compared with the hysteretic domain model. *Soil Science Society of America Journal*, 33(5):645–651, 1969.

[211] G. C. Topp. Soil water hysteresis in silt loam and clay loam soils. *Water Resources Research*, 7(4):914–920, 1971.

[212] S. C. Tsinontides and R. Jackson. The mechanics of gas fluidized beds with an interval of stable fluidization. *J. Fluid Mech*, 255:237–274, 1993.

[213] J. Van Brakel, S. Modrỳ, and M. Svata. Mercury porosimetry: State of the art. *Powder Technology*, 29(1):1–12, 1981.

[214] M. T. Van Genuchten. A closed-form equation for predicting the hydraulic conductivity of unsaturated soils. *Soil Science Soc. of America J.*, 44(5):892–898, 1980.

[215] O. Vizika, D. G. Avraam, and A. C. Payatakes. On the role of the viscosity ratio during low-capillary-number forced imbibition in porous media. *Journal of Colloid and Interface Science*, 165(2):386–401, 1994.

[216] H.-J. Vogel and K. Roth. Quantitative morphology and network representation of soil pore structure. *Advances in Water Resources*, 24(3):233–242, 2001.

[217] H. J. Vogel, J. Tölke, V. P. Schulz, M. Krafczyk, and K. Roth. Comparison of a Lattice-Boltzmann model, a full-morphology model, and a pore network model for determining capillary pressure – saturation relationships. *Vadose Zone Journal*, 4(2):380–388, 2005.

[218] N. M. Vriend, M. L. Hunt, R. W. Clayton, C. E. Brennen, K. S. Brantley, and A. Ruiz-Angulo. Solving the mystery of booming sand dunes. *Geophys. Res. Lett*, 34:L16306, 2007.

[219] N. M. Vriend, M. L. Hunt, and R. W. Clayton. Sedimentary structure of large sand dunes: examples from Dumont and Eureka dunes, California. *Geophys. J. Int*, 190:981–992, 2012.

[220] D. Wildenschild, C. M. P. Vaz, M. L. Rivers, D. Rikard, and B. S. B. Christensen. Using X-ray computed tomography in hydrology: systems, resolutions, and limitations. *Journal of Hydrology*, 267(3):285–297, 2002.

[221] D. Wilkinson and J. F. Willemsen. Invasion percolation: a new form of percolation theory. *Journal of Physics A: Mathematical and General*, 16(14): 3365, 1983.

[222] W. W. Willmarth. Pressure fluctuations beneath turbulent boundary layers. *Annu. Rev. Fluid Mech*, 7:13–36, 1975.

[223] J. C. Wyngaard. *Turbulence in the Atmosphere*. Cambridge University Press, N. Y., 2010. ISBN 978-0-521-88769-4.

[224] H. Yizhaq, Y.. Ashkenazy, and H. Tsoar. Why do active and stabilized dunes coexist under the same climatic conditions? *Phys. Rev. Lett*, 98: 188001, 2007.

[225] H. Yizhaq, I. Katra, J. F. Kok, and O. Isenberg. Transverse instability of megaripples. *Geology*, 40:459–462, 2012. doi: 10.1130/G32995.1.

[226] H. H. Yuan, B. F. Swanson, et al. Resolving pore-space characteristics by rate-controlled porosimetry. *SPE Formation Evaluation*, 4(01):17–24, 1989.

[227] E. A. Zedler and R. L. Street. Large-eddy simulations of sediment transport: currents over ripples. *J. Hydraulic Engrg*, 2001:444–452, June 2001.

[228] D. Zhang, C. Narteau, and O. Rozier. Morphodynamics of barchan and transverse dunes using a cellular automaton model. *J. Geophys. Res*, 115: F03041, 2010. doi: 10.1029/2009JF001620.

[229] D. Zhang, C. Narteau, O. Rozier, and S. Courrech du Pont. Morphology and dynamics of star dunes from numerical modelling. *Nature Geoscience*, 5:463–467, 2012. doi: 10.1038/ngeo1503.

[230] L. Zhao and K. S. Rezkallah. Gas-liquid flow patterns at microgravity conditions. *International Journal of Multiphase Flow*, 19(5):751–763, 1993.

[231] D. P. Zilker and T. J. Hanratty. Influence of the amplitude of a solid wavy wall on a turbulent flow. part 2. separated flows. *J. Fluid Mech.*, 90:257–271, 1979.